# DEVELOPMENT OF MgO-BASED SORBENTS PROMOTED BY ALKALI METAL SALTS FOR $CO_2$ CAPTURE

**ANA PATRÍCIA BENTO CORREIA**

THESIS TO OBTAIN THE MASTER'S DEGREE IN

**CHEMICAL ENGINEERING**

**SUPERVISORS:** Prof. Carla Pinheiro

Dra. Paula Teixeira

**EXAMINATION COMMITTEE**

**CHAIRPERSON:** Prof. Maria Teresa Duarte

**MEMBERS OF THE COMMITTEE:** Dra. Paula Teixeira

Prof. Moisés Pinto

**22 NOVEMBER 2021**

# ACKNOWLEDGMENTS

To the Portuguese Foundation for Science and Technology through research projects Carbon Emissions Reduction in the Cement Industry (PTDC/AAG-MAA/6195/2014), Solar-driven Ca-Looping Process for Thermochemical Energy Storage (PTDC/EAM-PEC/32342/2017) and UIDP/00100/2020 & UIDB/ 00100/2020, for the financial support.

To Dra Paula Teixeira, my supervisor, for the most extraordinary guidance, for the availability to help me almost daily, for all the shared knowledge, and for the constant concern I would deliver a complete and remarkable work. I could not have asked for a better supervisor.

To Prof. Carla Pinheiro, my supervisor, for the availability and academic advices.

To my grandparents, my biggest supporters, for praying so much for my success, for providing me the best education, and for allowing me to live my dreams and always wanting to be part of them.

To my parents, my unconditional supporters, for all the love and patience, for believing in me in a way I could never, for celebrating so much my highs and not so highs, and for always cheering me up in my lows.

To my sister Joana, my biggest pride, for being an excellence role model and an incredible perseverance example. I wish I could only conquer half of the things she already did and feel so fulfilled as she does.

To Inês, my best friend, for always showing so much interest in my academic life without often understanding a single word of what I was saying, and, together with Xana, João, Joana, Carlos e Tomás, for living my worries and my victories as if they were theirs.

And, finally, to the best friends that college could have given to me:

Tita, for always being there.

Ana Lou, for living together our best life.

Belga, for the endless late-night conversations in the car.

Paty Long, for speaking the hard truths.

Sofi, for making everything funnier.

Bia, for having the kindest words.

Ana Mercedes, for reminding me there will always be room for me in her heart.

Dobby, for being friends since day one.

This thesis is signed by me, but it is ours. I will forever be grateful to all of you!

# ABSTRACT

Carbon capture and storage (CCS) technologies are one of the most viable solutions to achieve carbon neutrality by 2050. MgO sorbents are promising materials, due to the high theoretical $CO_2$ sorption capacity (1.09 g of $CO_2$/ g of MgO) at intermediate temperatures (300 – 500 °C), small regeneration energy, wide availability and low cost. Their major drawbacks are exhibiting poor $CO_2$ sorption capacity, low kinetics and thermal stability.

In this work, nanosized MgO was produced using the sol-gel method. The sorbents' performance was further improved by the addition of supports, Ca and Ce-based, and by the doping with alkali metal salts (AMS), using molar percentages of 15 %, 25 % and 35 % of single salt $NaNO_3$ and of a mixture consisting of $NaNO_3$, $LiNO_3$ and $KNO_3$.

Cyclic stability was investigated by multiple sorption/ desorption tests using a thermogravimetric analyzer (TGA) and a continuous fixed-bed reactor. After 10 cycles in a fixed-bed under a sorption atmosphere of 100 % of $CO_2$, Ca and Ce-based supported MgO sorbents impregnated with 15 % of ternary mixture registered carrying capacities of 100 mg $CO_2$/ g sorbent and 152 mg $CO_2$/ g sorbent, respectively, considerably higher than the 44 mg $CO_2$/ g sorbent achieved by the unsupported sorbent. Such improvement was attributed to both the reduction of nitrates' sintering and segregation and the enhancement of sorbents' properties along cycles.

Textural, mineralogical and morphological characterization of the fresh and spent sorbents was made using X-ray diffraction (XRD), $N_2$ sorption and scanning electron microscope (SEM) techniques, respectively.

Key words: $CO_2$ sorption, nanosized MgO, supports, alkali metal salts, cyclic stability, fixed-bed reactor

# RESUMO

As tecnologias de captura e armazenamento de $CO_2$ são uma das soluções mais viáveis para atingir a neutralidade das emissões de carbono até 2050. Os adsorventes de MgO são materiais promissores, devido à elevada capacidade teórica de captura de $CO_2$ (1.09 g de $CO_2$ /g de MgO) na gama intermédia de temperaturas (300 – 500 °C), baixa energia de regeneração, vasta disponibilidade e baixo custo. Os maiores desafios são a baixa capacidade de captura de $CO_2$, cinética lenta e reduzida estabilidade térmica.

Este trabalho sintetizou adsorventes de MgO nanoporosos pelo método sol-gel, cujo desempenho melhorou acentuadamente através da adição de suportes, à base de Ca e Ce, e do doping com sais de metais alcalinos, usando percentagens molares de 15 %, 25 % e 35 % de $NaNO_3$ ou de mistura ternária de $NaNO_3$, $LiNO_3$ e $KNO_3$.

A estabilidade cíclica foi avaliada em ensaios de adsorção/ dessorção num analisador termogravimétrico e num reator de leito fixo. Após 10 ciclos no reator sob atmosfera de adsorção de 100 % $CO_2$, os adsorventes suportados com Ca e Ce impregnados com 15 % de mistura ternária registaram capacidades de 100 e 152 mg $CO_2$/ g adsorvente, respetivamente, superiores à do adsorvente não suportado (44 mg $CO_2$/ g adsorvente), devido à redução da sinterização e segregação dos nitratos e melhoria das propriedades dos adsorventes com os ciclos.

A caracterização textural, mineralógica e morfológica dos adsorventes frescos/ usados foi feita usando as técnicas de difração de raio-X, adsorção de $N_2$ e microscópio eletrónico de varrimento, respetivamente.

Palavras-chave: Adsorção de $CO_2$, MgO nanoporosos, suportes, sais de metais alcalinos, estabilidade cíclica, reator de leito fixo

## LIST OF CONTENTS

# LIST OF FIGURES

# LIST OF TABLES

# LIST OF ABBREVIATIONS AND ACRONYMS

IEA – International Energy Agency

GHG – Greenhouse Gases

GWP – Global Warming Power

ppb – Parts per billion

ppm – Parts per million

IPCC – Intergovernmental Panel on Climate Change

UNFCCC – United Nations Framework Convention on Climate Change Conference

COP – Conference of the Parties

CCUS – Carbon Capture Utilization and Storage

CCS – Carbon Capture and Storage

CCU – Carbon Capture and Utilization

Bt – Billion tonnes

Gt – Gigatonnes

Mt – Million tonnes

ASU – Air Separation Unit

IGCC - integrated Gasification Combined Cycles

BECCS – Biomass Energy with Carbon Capture and Storage

DACCS – Direct Air Carbon Capture and Storage

EOR – Enhanced Oil Recovery

AMS - Alkali Metal Salt

TGA – Thermogravimetric analyzer

MOFs – Metal-organic Frameworks

SERP – Sorption Enhanced Rection Process

SMR – Steam-methane Reforming

SEWGS – Sorption Enhanced Water-gas Shift

LDH – Layered Double Hydroxides

BET – Brunauer Emmett Teller

PTC – Phase Transfer Catalyst

TPB – Triple Phase Boundary

WGSR – Water Gas Shift Reaction

HTWGS – High-temperature Water Gas Shift Reaction

LTWGS – Low-temperature Water Gas Shift Reaction

SER – Sorption Enhanced Reaction

SESMR – Sorption Enhanced Steam Methane Reaction

CSP – Concentrating Solar Power

HTF – Heat Transfer Fluids

TG – Thermogravimetric

DTG – Differential Thermogravimetric

XRD – X-ray Powder Diffraction

IUPAC – International Union of Pure and Applied Chemistry

SEM - Scanning Electron Microscopy

CC – Carrying Capacity

EDS – Energy Dispersive X-ray Spectrometer

CS – Crystallite Size

LCA – Life Cycle Assessment

# 1 INTRODUCTION

According to the International Energy Agency (IEA), the global energy demand is expected to rise 12 % between 2019 and 2030 [1], with the increasing population growth and the improving quality of life being its two major driver forces [2]. Although such increasing demand may seem a sign of both development and evolution, it also means higher global resource use, where fossil-fuel based consumption is leading the way [2].

Currently, fossil fuels account for almost 80 % of total energy supply, with oil being the most used, followed by natural gas and, finally, coal [3]. These fuels are non-renewable, and their reservoirs are expected to last for a limited time of 50 or 150 years, considering both oil and coal or natural gas, respectively, at the current rate of exploration [4]. Fossil fuels' combustion releases greenhouse gases (GHG), such as carbon dioxide ($CO_2$), methane ($CH_4$) and nitrous oxide ($N_2O$). In addition, $CO_2$ is also a by-product of burning biomass, land-use changes and industrial products, such as cement and steel, which makes it the primary anthropogenic GHG [2]. Along with these related to human activities' sources, $CO_2$ also occurs naturally in the atmosphere and, thus, it is the most common GHG and the main responsible for climate change [2]. In this way, all GHG are measured with relation to $CO_2$, whose global warming potential (GWP) assumes the reference value of one [2].

The GWP is defined as the climatic warming potential of a greenhouse gas relative to carbon dioxide and it is calculated in terms of the 100-year warming potential of one kilogram of a greenhouse gas relative to one kilogram of $CO_2$ [5]. $CH_4$ and $N_2O$ have a GWP of 21 and 310 [6], respectively, meaning that emissions of these two GHG warm harder the atmosphere when comparing to those of $CO_2$. However, both $CH_4$ and $N_2O$ can only stay in the atmosphere for 12 and 120 years [6], respectively, presenting an extremely smaller lifetime than that of $CO_2$.

Since around 1750, when industrial revolution took place, the increasing concentrations of GHG are an unequivocal consequence of human activities [7]. From 2011 to 2019, GHG concentrations in the atmosphere have been continually increasing [7]. With respect to 2019, annual averages concentrations were 1866 parts per billion (ppb) for $CH_4$, 332 ppb for $N_2O$ and 410 parts per million (ppm) for $CO_2$ [7]. In 2020, average annual concentration of $CO_2$ in the atmosphere was 412.5 ppm [8]. This value was the highest ever being registered and it corresponded to the double to that of the beginning of industrial revolution [8]. It must be noted that thanks to the global covid-19 pandemic, global $CO_2$ emissions were reduced by 5.8 % in 2020, because both oil and coal demand also fell, while renewable's increased [8]. This reduction of global $CO_2$ emissions represented the biggest decrease ever and it accounted for almost five times than the decline relative to 2009, which in turn was due to the global financial crisis [8]. Besides there's an evident relation between global crisis and the almost immediate reduction of $CO_2$ global emissions, low economic grow does not mean low emissions strategy [1]. In this sense, global energy-related $CO_2$ emissions are expected to rise 4.8 % in 2021, since the demand for coal, oil and gas will rebound with the economy [8].

The Intergovernmental Panel on Climate Change (IPCC) 2021 report declared "code red for humanity" in what regards to climate change negative global impacts. The recently released report described the past five years as the hottest since 1850, with the global surface temperature being 1.09 °C higher from 2011 to 2020, when compared to that of the period that went from 1850 to 1900. In fact, society has been experiencing more often and hotter heatwaves than cold events since 1950s. Also, the primary driver for the glaciers' global retreat since the 1990s is appointed to be human activity. A direct consequence of the latter is the rise of sea level, whose increasing rate is nowadays the triple of that of the time interval from 1901 to 1971 [7]. As regards, consciousness on the hazardous nature of the GHG emissions, with special focus in the case of $CO_2$, and on its subsequent climate change negative impact was raised between scientists, researchers and policy makers in developed countries.

In December 2015, a historical agreement was adopted in Paris under the United Nations Framework Convention on Climate Change Conference (UNFCCC) at the 21st session of the Conference of the Parties (COP) [2]. Less than a year later, in November 2016, it became international law, when fifty-five countries representing at least 55 % of GHG emissions joined the agreement [9]. It defined three main climate goals, namely, the short-term goal aiming to peak carbon emissions to the atmosphere as early as possible; and two long-term goals that dictate to limit the rise in global average temperature to well below 2 °C, but preferably under 1.5°C, above pre-industrial levels, and to reach a neutral balance carbon in the atmosphere [2,9]. This carbon neutrality will be achieved when and if the anthropogenic emissions of GHG to the atmosphere and the anthropogenic removals are quantitatively the same, leading to net zero emissions [2]. And this is where carbon capture utilization and storage (CCUS) technologies can play a major role providing a net zero carbon future. In fact, the IPCC first recommendation's on Carbon capture and storage (CCS) technologies dates 2005 [10]. However, IPCC 2021 report states that both 2 °C and 1.5 °C targets won't be respected regardless the GHG emissions scenario that occurs [7].

IPCC defines CCS as "a process in which a relatively pure stream of $CO_2$ from industrial and energy-related sources is separated, conditioned, compressed and transported to a storage location for long-term isolation from the atmosphere" [2]. When the $CO_2$ is captured and subsequently used for the generation of a new product, it is correct to refer to it as a carbon capture and utilization (CCU) process [2].

The global evolution of the commercial CCS facility pipeline over the past decade is illustrated in Figure 1-1. Between the years 2011 and 2017, total capacity gradually decreased, a tendency believed to be a consequence of both the public and private sectors main goal being their recovery from global financial crisis. Fortunately, the following three years registered a promising growth, with the 2015 Paris Agreement as a big contributor to the acknowledgment that achieving negative to zero GHG emissions by mid-century is urgent. From 2019 to 2020, 17 new facilities joined the project pipeline, with the United States of America accounting for 12 of them. In 2020, there were 65 commercial CCS facilities. Among them, only 26 were operating, but the majority of the rest, 13 and 21 respectively, were in advanced development reaching front end engineering design or in early development [11].

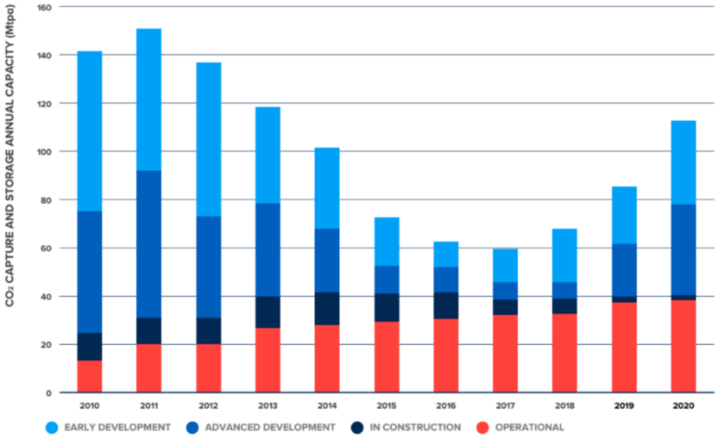

**Figure 1-1 – Pipeline of commercial CCS facilities from 2010 to 2020. [11]**

Figure 1-2 and Figure 1-3 intend to show how much CCUS can actually reduce $CO_2$ emissions in the most pollutant industry sectors. Industry is responsible for 8 billion tonnes (Bt) of direct $CO_2$ annual emissions, with cement, iron and steel, and chemical sectors accounting for 70 % of the total. The natural gas processing; the production of cement, iron, steel, ammonia and biofuel; and several petrochemical processes are examples of industrial processes with significant $CO_2$ emissions. Forecast predicts direct $CO_2$ emissions will grow up to 10 Bt per annum by 2060. In order to meet the Paris agreement's goals, these emissions must decline to 4.7 Bt by the same year. By implementing CCS technologies, it will be possible to capture 5.6 gigatonnes (Gt) in 2050 against the 40 million tonnes (Mt) per annum of nowadays. The power sector, for instance, is the main source of $CO_2$ emissions. As electricity demand is expected to significantly rise and is already responsible for a third of global $CO_2$ emissions, the sector must be decarbonized as soon as possible [11].

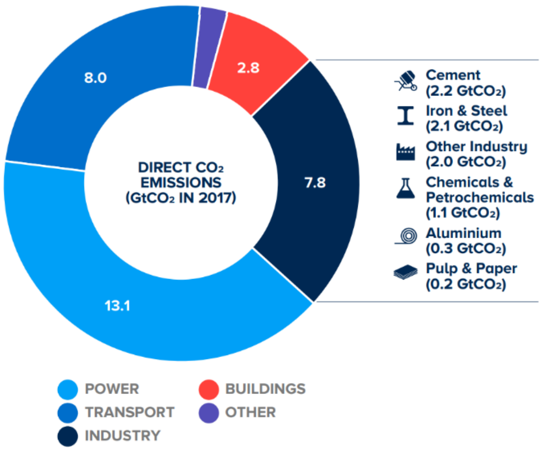

**Figure 1-2 – Global direct $CO_2$ emissions by sector. [11]**

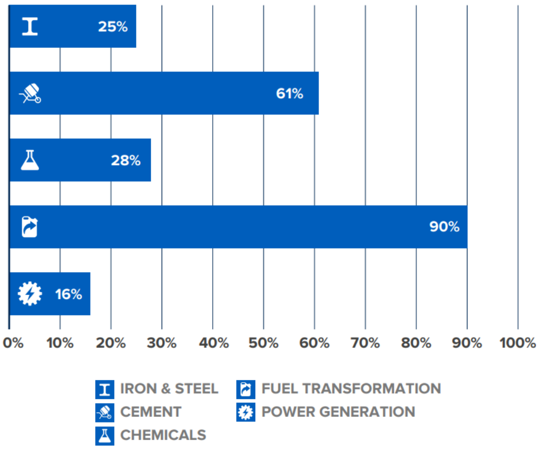

**Figure 1-3 – Contribution of CCUS to sector $CO_2$ emissions reductions up to 2070 in the IEA sustainable development scenario. [11]**

In the majority of industrial processes, the single feasible option to mitigate $CO_2$ emissions is to remove the $CO_2$ with CCS but only after production is finished. Currently, there are three general $CO_2$ capture approaches from point sources, namely, oxyfuel combustion, post-combustion capture and pre-combustion capture [12].

In the post-combustion capture (Figure 1-4), the $CO_2$ capture occurs after the combustion of the fuel. Hence, its implementation in an existing facility does not require changes in the base design. Instead, a new plant that captures and removes the $CO_2$ from the flue gas emerging from the boiler is added [13]. This possibility of retrofitting CCS represents its biggest advantage and makes it cost-effective and the simplest approach for controlling $CO_2$ emissions, especially for economies highly dependent on coal, such as China or India [11]. Considering a process using conventional combustion, the fuel is burned with air inside a boiler and steam at high temperature and pressure and exhaust gases are produced. The use of an excess of air guarantees an excess of oxygen ($O_2$), making the combustion complete, but also diluting the $CO_2$ until low concentrations of 4 % to 20 % within the other combustion gases, namely, the excess $O_2$, nitrogen ($N_2$) and water ($H_2O$). The exhaust gases go through a unit capture, where the $O_2$, the $N_2$ and the $H_2O$ are vented and the $CO_2$ is separated, compressed and storaged. The most widely commercialized post-combustion technology was first patented in 1930 and uses 30 – 40 wt.% amine molecules diluted in water that selectively absorb the $CO_2$ at atmospheric pressure among the other exhaust gases [14]. Typical $CO_2$ capture levels situate around 80 – 90 %, but values of 98 – 99 % are believed to be achieved easily. These low volatility amine solvents are sprayed at the top and flow down by gravity through an absorption tower with structured packing, while the flue gas passes through upwards in the opposite direction. The chemical reaction occurs at the interface between the gas and the liquid film spread on the packing, allowing the $CO_2$ to be removed by bonding strongly with the amines. Overall, this process consists of an amine solvent loop, in which there is the chemical absorption of the $CO_2$ from the exhaust gases into the solvent on one side followed by the desorption of the gaseous $CO_2$ from the solvent on the other side. The clean flue gas is then liberated to the atmosphere at the top of the tower and the chemical solvent enriched in $CO_2$ is collected at the bottom of the tower to be regenerated. The solvent regeneration is done by stripping with water vapor at 100 – 120 °C [14]. But both the solvent regeneration and the recycling process back to the system are extremely high demanding in energy, leading to an overall fall in the global efficiency. For example, once a supercritical coal-fired plant installs a post-combustion capture technology using amine solvents, its initial efficiency of 45 % will drop to 33 % [13]. Yet, the efficiency of the $CO_2$ capture varies with the $CO_2$ concentration in the flue gas. Higher concentrations allow the utilization of a physical adsorbent into which the $CO_2$ dissolves. Further technologies of capture are possible to implement. Cryogenic separation at temperatures until – 120 °C, for instance, can remove up to 90 % of the $CO_2$ from the flue gas, but the cooling costs associated are high. Adsorption with solid sorbents and capture with membranes are both inefficient [13].

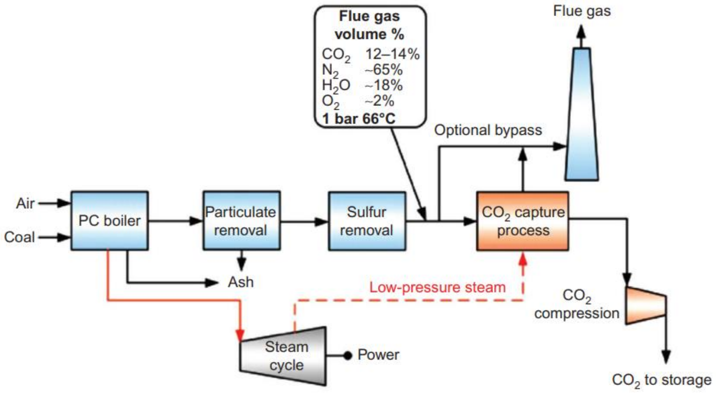

**Figure 1-4 – Schematic of a power plant with post-combustion technology for $CO_2$ capture. [13]**

In the oxyfuel combustion technology (Figure 1-5), the combustion of the fuel does not occur with air. Instead, it uses a mixture of $O_2$ and recycled flue gas [15]. After entering an air separation unit (ASU), air is separated into $N_2$ and $O_2$. A stream of very high purity $O_2$ is obtained and enters the boiler with the fuel. The fact that this type of technology burns the fuel with pure $O_2$ and in the absence of $N_2$ would make the combustion temperatures easily peak 2500 °C. To overcome extremely high temperatures, a fraction of the flue gas is recycled back to the combustion chamber, allowing the control of the flame temperature and the making up of the volume of the missing $N_2$. The heat produced in the combustion can be used to drive turbines and produce electricity while the combustion gases leave the boiler and enter into the capture unit. Once there is no $N_2$ inside the boiler, this capture unit has a significant smaller volume than that of post-combustion capture as well as nitrogen oxides, $NO_x$, emissions are substantially reduced. While the concentrations of $CO_2$ in the combustion gases usually represent 4 % to 20 % in a conventional combustion process, with this type of technology $CO_2$ concentrations can be higher than 90 %. The combustion gases of oxyfuel combustion are mainly $CO_2$ and $H_2O$. The $H_2O$ can be condensed using a simple process of drying of the gas. The result is a stream with 95 - 99 % of $CO_2$ that is then compressed, transported and storaged. Although oxyfuel combustion can be retrofitted to an existing facility, the ASU's cost is expensive [13].

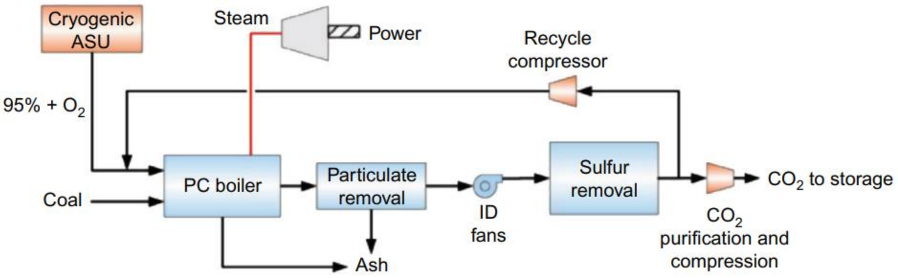

**Figure 1-5 – Schematic of a power plant using oxyfuel combustion technology for $CO_2$ capture. [13]**

In pre-combustion capture technologies, the $CO_2$ removal takes place before the fossil fuel combustion occurs, by converting it into a carbon-free fuel, that is, hydrogen ($H_2$). It is essentially a coal gasification reaction. As opposed to post-combustion and to oxyfuel combustion, pre-combustion capture technologies' implementation is limited to new-build power stations, because it requires the design of a process significantly different from conventional combustion. The overall process begins with air entering an ASU. While the $N_2$ stream is removed from the system, the very high purity $O_2$ stream enters in a gasifier, in which it reacts at high temperature and high pressure with the fossil fuel and steam, forming a synthesis gas. This synthesis gas, also called syngas, is a mixture of high-pressure $H_2$, carbon monoxide (CO), $CO_2$ and $H_2O$. By undergoing a water shift reaction, responsible for combining CO with $H_2O$, the syngas' both $CO_2$ and $H_2$ content increases. Here, $CO_2$ concentration can be more than 50 %, making its separation from the $H_2$ easier. Moreover, the $CO_2$ is already at high pressure and free of $N_2$. In this way, the volume of the gaseous mixture is expected to be smaller and, thus, it is possible to use physical absorption in the separation. This technique demands less energy when compared to using amines. In the capture unit, occurs the removal of 90 – 95 % of the $CO_2$ that is then dried, compressed and transported to be stored. The most common configuration for a coal gasification power plant is the integrated gasification combined cycles (IGCC) power plant (Figure 1-6), in which the produced $H_2$ is burnt in a gas turbine to produce electricity, impacting positively the global energetic efficiency of the system. The gasification and shift reaction steps, for instance, require very high energy inputs. The turbine waste heat produces steam in a heat recovery steam generator that, in turn, drives a steam turbine. Also, the waste heat from gasification is used in steam generation. Hence, theoretical energy conversion of an IGCC plant before $CO_2$ capture is 55 %. However, operational IGCC plants can only achieve conversions around 40 %. After $CO_2$ capture, efficiency falls to 32 % [13]

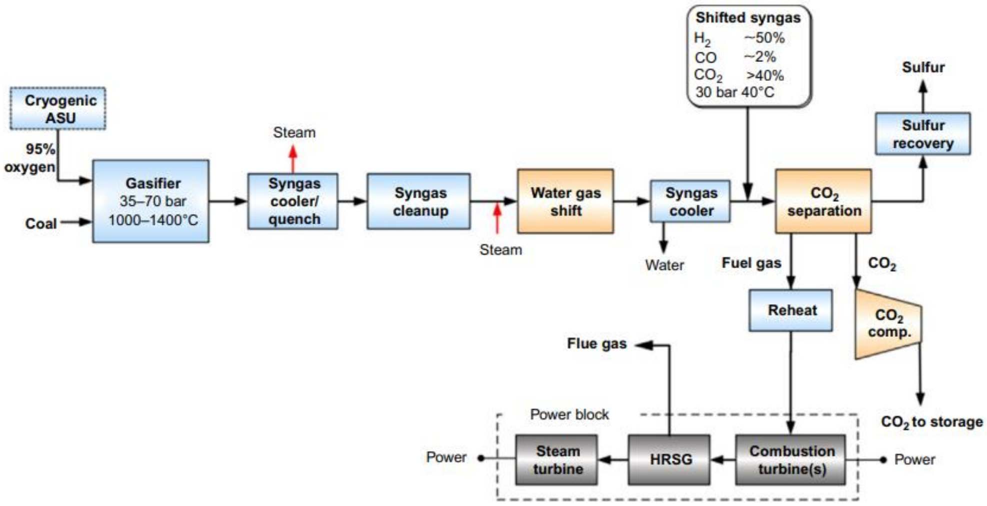

**Figure 1-6 – Schematic of a power plant with pre-combustion technology for $CO_2$ capture. [13]**

Regardless the technology, different types of materials can be used to selectively react with the $CO_2$. To choose the appropriate sorbent, the following parameters must be analyzed: sorption/ desorption kinetics, $CO_2$ capture capacity, operating temperature window, regenerability and multicycle stability, impact of flue gas components or contaminants, and cost [14].

The most studied, well-stablished and commercialized materials are the liquid adsorbents. In spite of having a relatively good $CO_2$ capture capacity, liquid adsorbents suffer from high energy consumption and lack of thermal stability in multi-cyclic $CO_2$ adsorption stripping. Aiming to overcome these limitations, solid adsorbents have been investigated and appointed as very promising materials, since they offer a wide operating temperature window, reduced waste production during cycling, high $CO_2$ capture capacity and the means to be discarded without excessive environmental concerns [12].

$CO_2$ utilization can complement CCS technologies by contributing to the main goal of mitigating $CO_2$ emissions and it is defined as the use of $CO_2$ that creates products with economic value. Figure 1-7 shows the variety of the existent $CO_2$ applications, which are categorized in three different areas, namely, chemical, mineralization and biological [16].

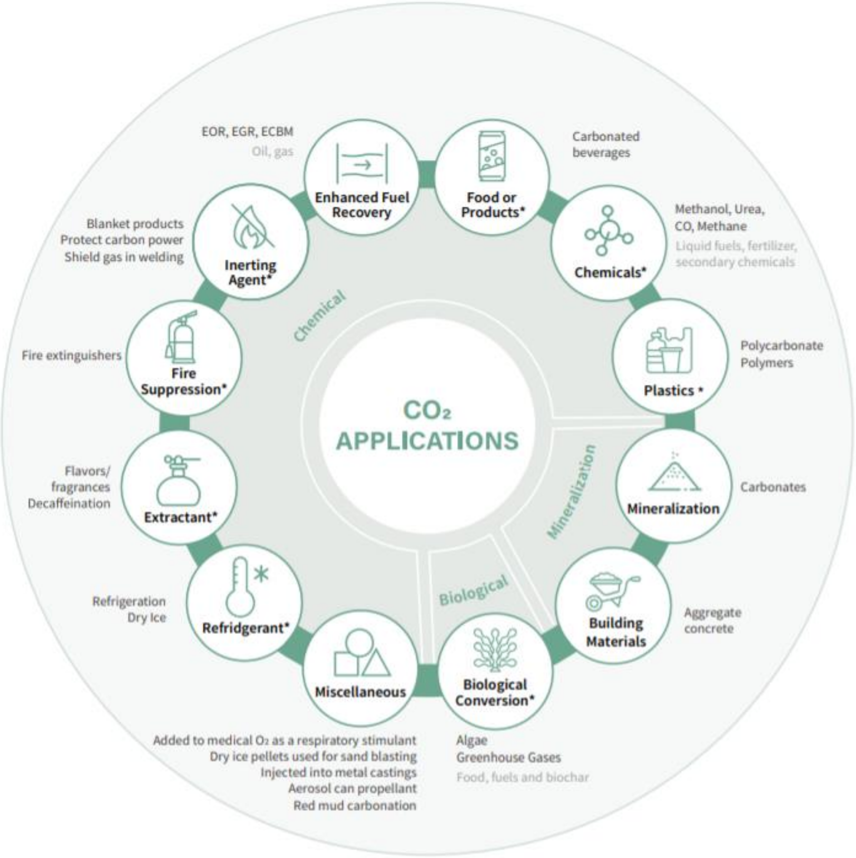

**Figure 1-7 – $CO_2$ applications. [16]**

The $CO_2$ utilization in the chemical sector deserves special attention. The majority of the chemical processes, such as the production of refrigerants, extractants, fire extinguishers, urea fertilizers, methanol and polymers for example, releases $CO_2$ emissions. Moreover, chemical products have very short lifetimes to be considered permanent storage solutions. In fact, $CO_2$ utilization can only be net-advantageous if it is replacing the use of petrochemicals. In this sector, greater environmental impact is achieved if using $CO_2$ coming from biomass energy with carbon capture and storage (BECCS), direct air carbon capture and storage (DACCS) or waste streams. In a hydrogen-based economy, the hydrogenation of $CO_2$ will produce synthetic fuels, syngas and methanol with near to zero GHG emissions. This subject is further explored in 2.3 section. Several chemicals and polymers, for example, are produced from methanol and syngas [16–17].

The greatest current exception of the chemical sector is the enhanced oil recovery (EOR) technique that represents the primary market for CCU, due to the high $CO_2$ exploration rate from oil and gas industries. It consists in the direct injection of $CO_2$ into oil wells to increase the recovery of both oil and gas. At depths higher than 700 m, $CO_2$ is in its supercritical form, acting as a good solvent and, thus, facilitating the release of the oil gas from the containing rocks. Furthermore, there is the possibility of sequestrating the injected $CO_2$ in the exhausted well, that is, EOR is actually a CCUS technology [16–17].

Regarding to the mineralization sector, the production of both concrete and aggregate from $CO_2$ is an energy efficient process and represents a long-term to permanent sequestration solution, as it is able to store $CO_2$ for long decades. In addition, concrete is made of cement that, in turn, accounts for 8 % of the total GHG. Thus, there's great potential for it to become a larger market. Yet, the current market is very competitive since the existing products are very low priced [16–17].

In the biological sector, the $CO_2$ is used to enhance either plant growth or soil quality by being captured with biochar. One important example of biological conversion is the $CO_2$ absorption and fixation through photosynthesis by microalgae that exhibit a very high growth rate in atmospheres rich in $CO_2$. Photosynthetic cyanobacteria also capture and use $CO_2$ in the production of organic content via the Calvin cycle. Moreover, the growing of microbial proteins uses $CO_2$, either from atmosphere or from industrial flue gases. Agricultural greenhouses improved crop yields after enriching their internal atmosphere with $CO_2$ [16–17].

Figure 1-8 summarizes the main $CO_2$ sources, CCS technologies, $CO_2$ capture methods and CCU categories.

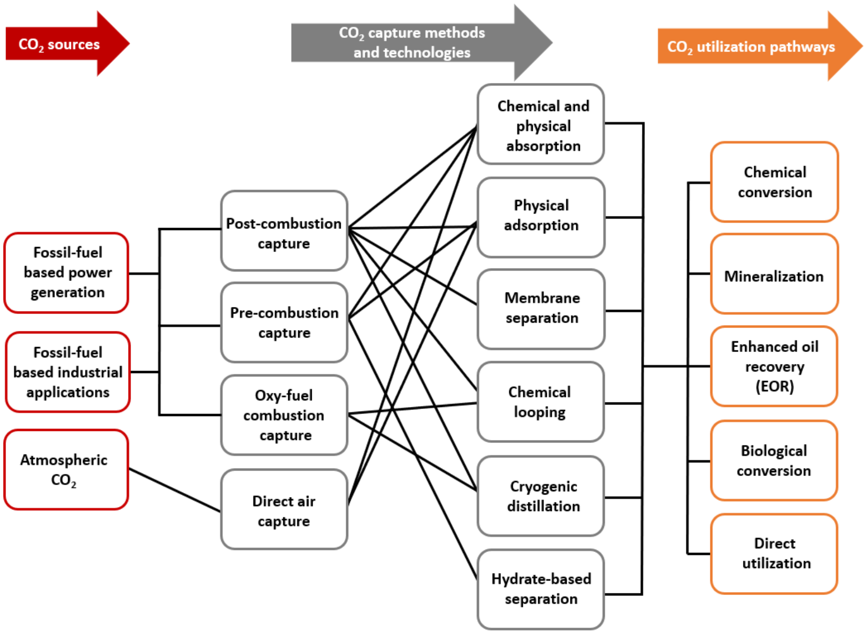

**Figure 1-8 – Schematic diagram of the existent $CO_2$ sources, CCS technologies, $CO_2$ capture methods and CCU categories. Adapted from [17]**

## 1.1 MOTIVATION AND RESEARCH GOALS

CCS technologies are appointed as one of the most viable solution for the mitigation of global $CO_2$ emissions and MgO-based sorbents are considered promising materials to be used in the integrated $CO_2$ capture step. They present high theoretical $CO_2$ capture capacity, small regeneration energy, wide availability and low price. Their major drawback is exhibiting experimental poor $CO_2$ capture capacity associated with both low kinetics and thermal stability. Research studies are focused in finding strategies to overcome it. This thesis aims to evaluate the potential of the alkali metal salts (AMS) doping on the enhancement of the $CO_2$ uptake of MgO-based sorbents. The research objectives targeted for this thesis are the following:

- Test the efficiency of the sol-gel method in the synthesis of homogeneous and mesoporous MgO sorbents;
- Test the effect of adding Ca and Ce-based supports to MgO sorbents;
- Test the efficiency of the impregnation method with different mixtures and molar percentages of AMS, namely, 15 %, 25 % and 35 % of $NaNO_3$ and 10 %, 15 %, 25 % and 35 % of ternary mixture consisting of 52 wt.% $KNO_3$, 18 wt.% $NaNO_3$ and 30 wt.% $LiNO_3$, in unsupported and supported MgO sorbents;
- Assess the thermal decomposition of $NaNO_3$ and ternary mixture consisting of 52 wt.% $KNO_3$, 18 wt.% $NaNO_3$ and 30 wt.% $LiNO_3$ in a thermogravimetric analyzer (TGA) over a temperature window from 20 °C to 1000 °C under two different atmospheres, namely, 100 % of $CO_2$ and 100 % of air;
- Find the most promising sorption/ desorption time and temperature operational conditions;
- Test the $CO_2$ uptake of unsupported and supported MgO sorbents, before and after doping, in a TGA over a temperature window from 20 °C to 500 °C under an atmosphere of 100 % of $CO_2$;
- Test the $CO_2$ uptake and cyclic stability of the most promising unsupported and supported doped MgO sorbents over 5 sorption/ desorption cycles in a TGA using the operational temperature conditions previously selected;
- Test the $CO_2$ uptake and cyclic stability of the most promising unsupported and supported doped MgO sorbents over 10 sorption/ desorption cycles in a fixed-bed reactor under two different sorption atmospheres, namely, 100 % of $CO_2$ and 25 % of $CO_2$ + 75 % of air.

# 2 LITERATURE REVIEW

## 2.1 TYPICAL $CO_2$ SORBENT MATERIALS / $CO_2$ CAPTURE BY SOLID SORBENTS

According to their sorption temperature, solid sorbents are classified in three different categories: low-temperature (< 200 °C) , intermediate-temperature (200 °C – 400 °C) and high-temperature (> 400 °C) [12].

**Low-temperature sorbents** include aqueous amine and amine-based solid sorbents, zeolites, active carbons, metal-organic frameworks (MOFs) and ionic liquids [14].

According to their structure, amines interact with $CO_2$ molecules by different mechanisms. Primary and secondary amines react directly with $CO_2$, forming a zwitterionic intermediate to produce carbamates. Tertiary amines act as catalysts in the bicarbonate formation according to the base-catalyzed hydration of $CO_2$. Regardless the mechanism, amines capture $CO_2$ at temperatures below 100 °C. This is the most common technology used in post-combustion processes since $CO_2$ capture occurs at room or low temperatures. Its application is also possible in pre-combustion processes. The outlet flue gas stream needs to be cooled before $CO_2$ scrubbing and subsequently re-heated, with an elevated energy penalty, though. Material degradation, vessel corrosion and evaporation are other drawbacks associated to aqueous amines. Amines dispersed in a solid support, like silica, can overcome them [14].

The $CO_2$ adsorption mechanism of zeolites consists of physisorption mostly, but with a small presence of chemisorption in the overall process. Zeolites are aluminosilicates with a crystalline and porous structure of repeated arrays of orthosilicate ($SiO_4^-$) and $AlO_4^-$. Zeolites 13X and 4A showed $CO_2$ capture capacities of 160 and 130 mg $CO_2$/ g sorbent, respectively, at 25 °C and 1 atm of $CO_2$ partial pressure. It was also described the abrupt decline in $CO_2$ capture capacity with the small increasing of room temperature. This evidence represents a serious disadvantage in what concerns to use zeolites as $CO_2$ sorbents of power plants' flue gases that are usually at temperatures of 50 to 120 °C [14].

Active carbons capture $CO_2$ by physical adsorption. An isotherm test registered a $CO_2$ absorption capacity of 90 mg $CO_2$/ g sorbent at 1 bar and 25 °C. It was verified that its $CO_2$ capture capacity decreased quickly with the rising of temperature. Activated carbon show worse $CO_2$ capture performance than zeolites. Its biggest advantage is the very low cost of the raw-materials, such as, coal, petroleum, wood or biomass [14].

The great developing of MOFs is due to their wide application in gas separation and heterogeneous catalysis. MOFs consist of organic ligands coordinated to metal-based nodes forming a three-dimensional network with uniformly dispersed pores ranging diameters of 3 to 20 Å. These materials are associated with extraordinary high surface areas of 1500 to 4500 $m^2$/ g, which results in better $CO_2$ capture performance when compared to zeolites. For example, the MOF $[Zn_4O(btb)_2]$ (MOF-177) exhibited a surface are of 4500 $m^2$/ g and a $CO_2$ capture capacity of 1470 mg $CO_2$/ g sorbent at room temperature and 42 bar of $CO_2$ pressure. Zeolite 13X registered a $CO_2$ capture capacity three times smaller under identical operation conditions. Even if under pressurized conditions, MOFs can work at low temperatures [14].

The interest in using ionic liquids for $CO_2$ capture is based in the non-measurable vapor pressure and excellent thermal stability that characterized them. Ionic liquids consist of large organic cations combined with smaller inorganic anions in a liquid form at room temperature. Its $CO_2$ capture mechanism occurs by physisorption, but with slow sorption kinetics [14].

**Intermediate-temperature sorbents** consist of hydrotalcites, magnesium oxide (MgO) and magnesium oxide-based salts. The arising area of sorption enhanced reaction process (SERP) for hydrogen production by steam-methane reforming (SMR) has triggered the development of materials that can either reversibly and selectively absorb $CO_2$ between 200 – 400 °C with an uptake capacity higher than 22 mg $CO_2$/ g sorbent [14]. In fact, this is also a very promising pre-combustion $CO_2$ capture technology for IGCC-related processes requiring it, e.g., sorption enhanced water-gas shift (SEWGS) and SERP, that prefer to use solid sorbents operating in this temperature range [12]. Air Products and Chemicals, Inc. have been leading the study and already have made novel progress in developing Intermediate-temperature sorbents, namely, potassium carbonate-promoted hydrotalcite and MgO-contained double salt [14].

Hydrotalcites compounds, also designated as layered double hydroxides (LDH)-derived metal oxides, are associated with distinctive properties like adsorption capacity, anions mobility, large surface areas and structural capacity [14]. Potassium carbonate ($K_2CO_3$)-promoted hydrotalcite is an example. Its optimal adsorption temperature was found to be 400 °C with a sorption working capacity of 37 mg $CO_2$/ g sorbent. A surprisingly capacity exceeding 660 mg $CO_2$/ g sorbent was achieved with a similar hydrotalcite compound. The presence of magnesium carbonate ($MgCO_3$) was mentioned to contribute for this significant uptake. Nevertheless, its operational conditions of using partial pressures of steam and $CO_2$ over 20 bar did not have a practical utilization. Attending to the equilibrium of magnesium hydroxide ($Mg(OH)_2$) formation from MgO in steam, $Mg(OH)_2$ is more likely to form than hydrotalcite under the pressurized and high steam environment, which justifies the obtained $CO_2$ uptake [14].

With respect to MgO, the interest among scientific researchers in using it to create new $CO_2$ sorbents has been growing significantly in recent years [12]. The benefits associated to MgO-based compounds are several. MgO is nontoxic, noncorrosive and is largely available in nature, where it is abundant at a relatively low cost. It also offers a wide temperature range to work with, one that goes from room to intermediate temperatures. Even its regeneration can occur around 500 °C, which is a moderately low temperature, when compared to the one used with high-temperature $CO_2$ basic metal oxide sorbents, like calcium oxide (CaO), lithium orthosilicate ($Li_4SiO_4$) and lithium zirconate ($Li_2ZrO_3$) sorbents. Economic benefits unfold from using lower temperatures, since energy consumption is reduced, which in turn impacts positively the system efficiency. In addition, MgO owns a moderate basicity and it is associated with a high theoretical $CO_2$ capture capacity of 1.09 g $CO_2$/ g MgO [18], since one mole of MgO can absorb one mole of $CO_2$, according to the direct reaction described in equation (1) [12].

$$MgO\ (s) + CO_2(g) \rightleftharpoons MgCO_3(s) \qquad (1)$$

$$\Delta H^0_{298\ K} = -116{,}9\ kJ/mol$$

The $CO_2$ capture process with MgO-based sorbents follows the reversible reaction described by equation (1). The circulation of the MgO-based sorbent between both the carbonation and the regeneration reactors is illustrated in Figure 2-1. The $CO_2$ from the inlet gas stream is captured in the carbonator, releasing an outlet gas stream without $CO_2$. A carbonated sorbent is also obtained. The latter enters into a regenerator where it is decomposed in both MgO and $CO_2$. The outlet concentrated in $CO_2$ gas stream goes to compression and storage, while MgO is recycled to the carbonator.

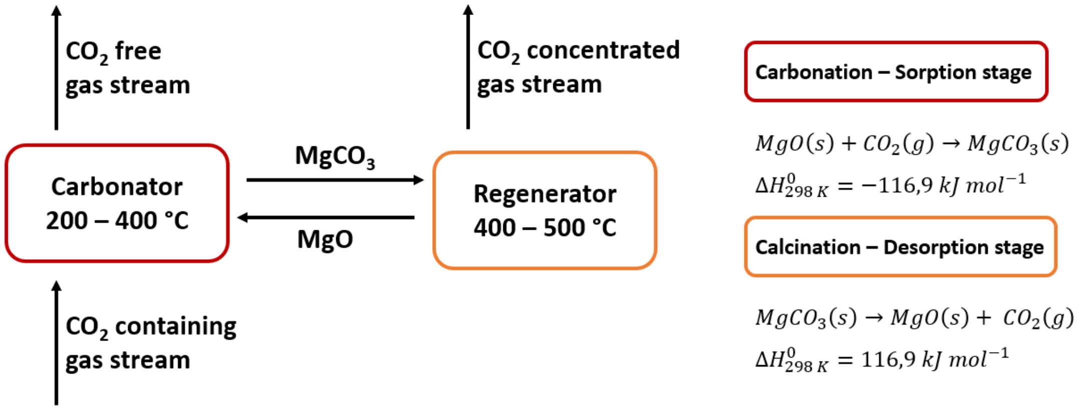

**Figure 2-1 – Schematic of the cyclic $CO_2$ removal process based on MgO sorbents. Adapted from [12]**

In practice, most of MgO-based sorbents do not exhibit the expected theoretical capture capacity. In fact these materials are characterized with low $CO_2$ capture capacity due to having slow kinetic reactivity [10,12]. For instance, commercial MgO powder presents a $CO_2$ capture capacity of only 20 mg $CO_2$/ g MgO at 200 °C [18]. There are two main factors that are believed to justify MgO-based sorbents' both poor capture capacity and slow kinetics. First one is related to the fact that MgO has a low surface area and, hence, does not expose its basic sites sufficient well for $CO_2$ sorption. Taking the same example of the commercially available MgO as above, its surface area situates between 8 to 35 $m^2$/ g [18]. Moreover, MgO has a volume expansion of 2.49 times [18] caused by the formation of $MgCO_3$.. This termination product layer ends up covering with dense layers the adjacent basic active sites of the MgO sorbent, inhibiting the $CO_2$ sorption to proceed. This evidence supports the fact that the poor adsorption capacity is a surface phenomenon [12]. The other reason lies in MgO's intrinsically high lattice enthalpy [6]. Low porosity is also often related to low kinetics, since MgO's strait pores obstruct the $CO_2$ diffusion through them and, thus, delay the adsorption equilibrium [12]. Poor thermal and mechanical stability, low coordination, and the edges and corners of the crystalline structure of MgO sorbents are other disadvantages.

**High-temperature sorbents** include CaO, $Li_2ZrO_3$ and $Li_4SiO_4$ [14].

CaO-based materials have been recognized as the ideal high-temperature sorbents [19]. These materials are associated with several benefits that include good absorption capacity and fast kinetics [20]. The large availability of natural CaO precursors also makes these materials cost-effective [19]. Their ultimate drawback is the great loss of $CO_2$ capture performance over multiple cycles due to particle sintering. Besides presenting a very high theoretical maximum $CO_2$ capture capacity of 786 mg $CO_2$ / g sorbent, their actual capacity is lower. CaO reacts with $CO_2$ to obtain calcium carbonate ($CaCO_3$) in a temperature window of 600 – 800 °C (equation (2)), according to its carbonation reaction that is exothermic. Regeneration temperature requires to be higher than 800 °C.

$$CaO\ (s) + CO_2(g) \rightleftharpoons CaCO_3(s) \tag{2}$$

The adsorption mechanisms of $Li_2ZrO_3$ and $Li_4SiO_4$ are described in equations (3) and (4), respectively. Both sorbents work at an operation temperature higher than 500 °C [10].

$$Li_2ZrO_3\ (s) + CO_2(g) \rightleftharpoons Li_2CO_3\ (s) + ZrO_2\ (s) \tag{3}$$

$$Li_4SiO_4\ (s) + CO_2(g) \rightleftharpoons Li_2CO_3\ (s) + Li_2SiO_3\ (s) \tag{4}$$

$Li_4SiO_4$ is characterized as a cost-effective sorbent, as silica ($SiO_2$) is a reagent in its preparation, with promising sorption performance. $Li_2ZrO_3$ is a more expensive sorbent showing smaller $CO_2$ capture capacity.

## 2.2 APPROACHES TO ENHANCE THE $CO_2$ CAPTURE PERFORMANCE OF MAGNESIUM OXIDE BASED SORBENTS

As mentioned in section 2.1, besides the interesting advantages of MgO as $CO_2$ sorbent, MgO revealed a very low experimental $CO_2$ uptake capacity of 11 – 20 mg $CO_2$/ g sorbent and a very poor experimental sorption kinetics at a very favorable temperature of 200 °C from the thermodynamic point of view [10,14,16].

In order to understand the thermodynamic limitations constraining the operational conditions associated to the equilibrium described in equation (1), it was plotted the $CO_2$ partial pressure, $P_{CO2}$, as function of the dissociation or equilibrium temperature, $T_{eq}$ (Figure 2-2). For instance, the temperature corresponding to the dissociation of $MgCO_3$ into MgO and $CO_2$, that is, the indirect reaction in equation (1), represents the thermodynamic limit for carbonation. The equilibrium temperature was calculated with equation (5) by arbitrating different values of $CO_2$ partial pressure [21].

$$T_{eq} = \frac{13636}{ln\left(\frac{[bar]}{P_{CO_2}}\right) + 20.01} - 273.15 \tag{5}$$

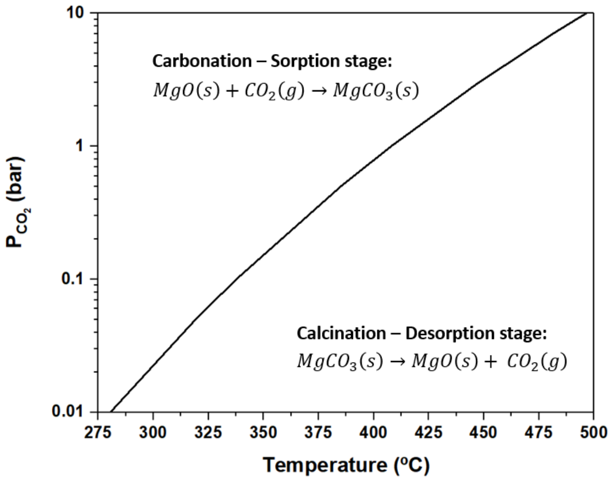

**Figure 2-2 – $MgCO_3$ equilibrium curve relating the temperature to the $CO_2$ partial pressure. Adapted from [21]**

The thermodynamic equilibrium of $MgCO_3$ represents a limitation in what concerns to increasing the working temperature. Only if working at high pressures, then higher operating temperatures would be possible to consider, but both kinetic and uptake could still be a concern, as well as it could be dangerous for practical applications [14,18]. The possibility of working at relatively low temperatures makes MgO compounds attractive to explore, but it is mandatory to overcome uncompetitive capacities and low sorption kinetics rates first. In this sense, researchers started to study different paths to enhance their performance, based on the sorbents' dependence on intrinsic and extrinsic factors.

### 2.2.1 INTRINSIC FACTORS

Most promising approaches aiming to improve the $CO_2$ capture performance of MgO sorbents by upgrading their internal properties consist of the following [6]:

- Synthesizing mesoporous MgO;
- Producing MgO from effective magnesium precursors;
- Dispersing MgO on porous supports and;
- Doping MgO with AMS.

The hypothesis that to **synthesize mesoporous MgO** as an effective way to improve its $CO_2$ capture capacity bases itself in the $CO_2$ adsorption mechanism on MgO surface [10].

In general, the $CO_2$ adsorption process in porous materials consists of the following five consecutive steps that are illustrated in Figure 2-3 [22]:

- Bulk diffusion: diffusion of $CO_2$ molecules from the bulk gas phase to the exterior of the gas film;
- Film diffusion: diffusion of $CO_2$ molecules through the gas film;
- Interparticle diffusion: diffusion of $CO_2$ molecules in the pore among the agglomerate particles;
- Intraparticle diffusion: diffusion of $CO_2$ molecules in the crystalline grains;

- Surface adsorption: interaction of $CO_2$ molecules with the sorbent.

The surface adsorption last step occurs rapidly with an associated resistance considered insignificant. The subsequent adsorption proceeds under the control of a single diffusion or of the combination of them [22].

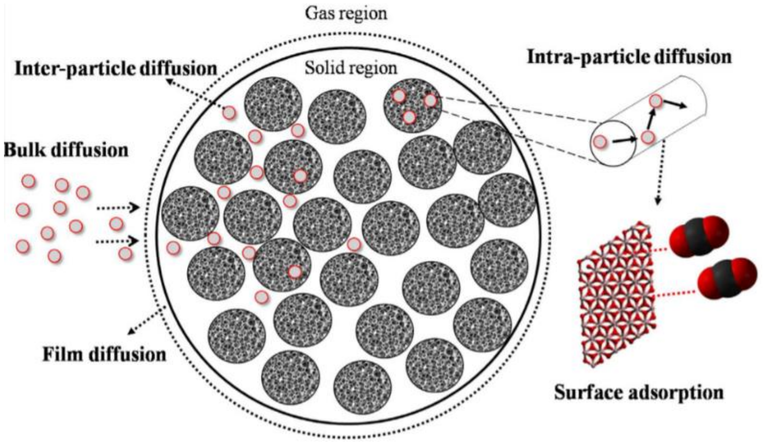

**Figure 2-3 – Schematic $CO_2$ adsorption mechanism on a porous sorbent. [22]**

Concerning to the $CO_2$ adsorption mechanism on MgO's surface, it occurs by rapid physical adsorption at low temperatures and by chemisorption at temperatures above 100 °C [12]. $CO_2$ adsorption mechanism on porous MgO's is actually a two-stage adsorption process comprising a quick initial $CO_2$ uptake headed by film diffusion from the bulk gas phase to the MgO exterior; followed by a slow adsorption controlled by strong intraparticle diffusion resistance, which, in turn, is due to the existence of numerous narrow pores that mitigate the process [12,22].

The $CO_2$ adsorption kinetics on porous MgO can be described by a pseudo-second order model [12]. This model assumes that the adsorption rate is proportional to the square of the number of empty adsorption sites according to equation (6) [22].

$$\frac{dq}{dt} = k_s(q_e - q_t)^2 \tag{6}$$

Where $q_e$ [mol/ Kg] and $q_t$ [mol/ Kg] are the adsorption capacities at equilibrium and at given time, respectively, and $k_S$ [$min^{-1}$] is the second order kinetic constant.

Considering the boundary conditions of $t = 0$, $q_t = 0$ and $t = \infty$, $q_t = q_e$, the adsorption capacity at given time is described by equation (7) [22].

$$q_t = \frac{{q_e}^2 k_s t}{1 + q_e k_s t} \tag{7}$$

The pseudo-second order model describes the adsorption process occurring by chemisorption, since it assumes the interaction established between the adsorbent and the adsorbate as a consequence of the powerful binding of the $CO_2$ on the sorbent's surface. Thus, to be described by this model signifies that $CO_2$ adsorption by MgO occurs mainly by chemisorption. There is only a small fraction of physisorption in the process [22].

Considering dry $CO_2$ conditions and moderately high temperatures, gaseous $CO_2$ reacts with MgO molecules to form a covering layer of the thermodynamically stable $MgCO_3$ on the unreacted sorbents' surface (equation (1)). Next, $CO_2$ molecules diffuse through the product layer, continuing the sorption process [10]. Sorbents with high surface area are associated with small pore diameter, meaning an elevated number of available basic sites on the sorbents surface [12]. The efficient adsorption sites for $CO_2$ on MgO surface are the low coordinated $Mg^{2+} – O^{2-}$ sites. The acidic $CO_2$ molecules react reversibly with the basic $O^{2-}$ sites [12]. Thus, it is important to produce an MgO sorbent with both high surface area and porosity to improve the $CO_2$ diffusion, enhancing the capture capacity of the former and the kinetics reactivity [10,12].

**Magnesium precursors** are proved to influence physical properties and surface morphologies of MgO sorbents [10]. Hence, the selection of the appropriate precursor is believed to enhance MgO-based sorbents' $CO_2$ capture capacity. There are three types of most common used precursors: inorganic salts, organometallic salts and natural minerals. In general, the organometallic salts of magnesium are better precursors than the other two types for the production of efficient MgO sorbents. This is mainly due to the fact that the former usually present larger molecular weight [10]. It has been experimentally demonstrated that precursors with high molecular weight per single magnesium (Mg) atom lead to the production of MgO compounds with high porosity, pore volume and pore size [12]. Other investigations showed that organometallic precursors also produce porous materials with higher Brunauer Emmett Teller (BET) surface areas, because they experience a higher mass loss during thermal decomposition [10]. The biggest disadvantaged related to organometallic precursors is the expensive cost. On the contrary, natural Mg-containing minerals are abundant in nature and, thus, are cost-effective [10].

Porous MgO produced by carbonization of magnesium acetate ($Mg(CH_3COO)_2$) showed a BET surface area of 300 $m^2$/ g and a $CO_2$ capture capacity of 28.9 mg $CO_2$ / g sorbent. In comparison, an MgO sorbent derived from magnesium nitrate ($Mg(NO_3)_2$) presents a $CO_2$ capture capacity 7 times smaller [10]. It is described in literature that magnesium oxalate ($MgC_2O_4$) is a better precursor than $MgCO_3$ because it generates MgO sorbents with better performance. Guo et al obtained a MgO sorbent derived from magnesium oxalate dihydrate ($MgC_2O_4.2H_2O$) with the highest $CO_2$ capture capacity of 194 mg $CO_2$ / g sorbent. This sorbent was characterized with excellent textural properties, uniform surface and plentiful of basic sites [23]. Hanif et- al synthesized mesoporous MgO with a BET surface area higher than 350 $m^2$/ g by ammonium-hydroxide-assisted precipitation of $Mg(OH)_2$ from a $Mg(NO_3)_2$ aqueous solution followed by thermal degradation of the precipitated $Mg(OH)_2$ in vacuum. The same sample presented a $CO_2$ capture capacity of 75 mg $CO_2$ / g sorbent at 300 °C [24].

The **dispersion of nanoparticles on a porous support** allows the sorbent to gain smaller particles, larger surface areas and abundant and well-exposed basic active sites, which in turn improves the sorbent's capture capacity [10]. It is described in literature that to combine highly porous supported materials with metal oxides, as it is MgO, upgrades the sorbent's active sites as well as their dispersion, facilitating the adsorption of a weak acidic gas, as it is $CO_2$ [12]. A good support must present a porous structure that is able to resist to variations in sorption/ reaction and desorption/ regeneration; and that allows the good dispersion and separation of the active component Mg, so it doesn't agglomerate, but withstand both the formation and decomposition of the carbonate [12]. Moreover, porous supports interfere with the sintering process in a way that the sorbent achieves a stable capacity after several cycles, with less reduction of $CO_2$ uptake capacity.

The **doping with alkali metal salts** is the most widely recognized promising approach [12]. The aim of the most recent experimental works is to improve the $CO_2$ uptake capacity of these materials up to 700 – 800 mg $CO_2$/ g sorbent [25]. The alkali carbonates and the alkali nitrates/nitrites are the most commonly used [10]. In general, it is considered three categories of alkali doping: alkali carbonate doping, alkali nitrate/nitrite doping and binary or ternary alkali doping.

A U.S patent on MgO-based double salts reports a favorable $CO_2$ uptake capacity range of 48 – 568 mg $CO_2$/ g sorbent of alkali promoted MgO-based sorbents with different synthesis conditions [14]. The highest regenerable capacity obtained was 484 mg $CO_2$/ g sorbent for pressure swing adsorption, PSA, at 375 °C [14]. The MgO-based double salts consist of compounds with MgO and more than one cation or anion that are obtained by crystallizing two different salts in the same regular ionic lattice [14].

Regarding to alkali carbonate doping, the $CO_2$ mechanism sorption is believed to happen in two steps illustrated in Figure 2-4. First step consists in the quick generation of basic sites on the MgO surface, due to established interactions between the sorbent and the alkali metal carbonate molecules. The nature of the AMS highly impacts the kinetics and the sorption capacity of the doped MgO sorbent at this stage because the basicity level of the produced active sites is influenced by the size of the ion salt. Second step is the slow formation of the double carbonate phase between the Mg and the AMS [10].

Reactions described in equations (8) and (9) refer to the generic example of doping an MgO sorbent with $A_2CO_3$, with A = Na, K, Rb or Cs.

$$A_2O + CO_2 \rightarrow A_2CO_3 \text{ (1}^{\text{st}}\text{ sorption step)} \quad (8)$$

$$A_2CO_3 + MgO + CO_2 \rightarrow A_2MgCO_3 \text{ (2}^{\text{nd}}\text{ sorption step)} \quad (9)$$

In the mixing of $A_2CO_3$ and MgO molecules, occurs the decomposition of some $A_2CO_3$ molecules in $A_2O$. $A_2O$ molecules act as dopant, generating basic sites in the MgO surface. Subsequently, the first sorption starts. The active basic sites react with $CO_2$ to form $A_2CO_3$ until a saturation point is reached. Then, the second sorption takes place, producing double carbonates through the interaction of A and Mg ions. In this mechanism, there are two different sources of $A_2CO_3$, namely, the $A_2CO_3$ formed in the first step and the unreacted $A_2CO_3$. As a result, the rate of the second sorption is lower than that of the first sorption since the former requires the $A_2CO_3$ diffusion through the sorbent's surface [10].

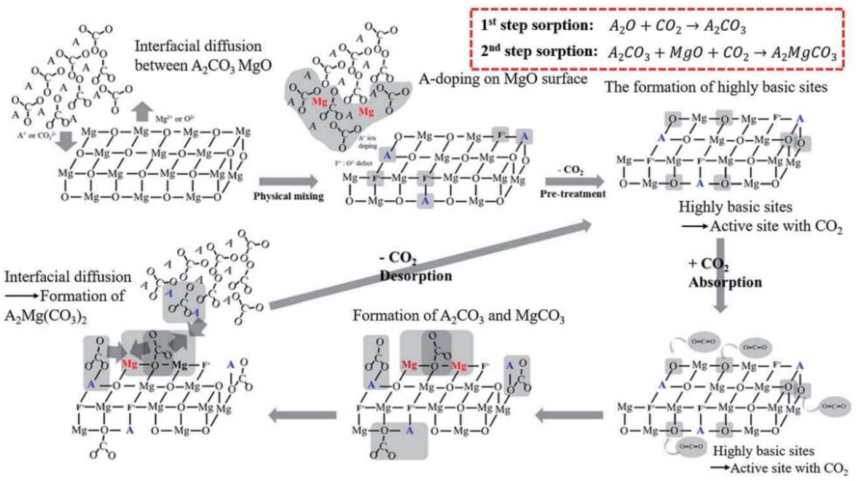

**Figure 2-4 – Mechanism of $CO_2$ sorption and desorption on alkali carbonate doped MgO sorbents. [10]**

It is described in literature that alkali metal carbonate doped MgO sorbents prepared by coprecipitation registered $CO_2$ capture capacities of 48 – 570 mg $CO_2$/ g sorbent at the temperature range of 350 °C to 400 °C and under 70 % dry $CO_2$ [10]. In addition, it was observed that the performance of the doped sorbent was influenced by the doping content. Sodium carbonate ($Na_2CO_3$) doped MgO sorbents showed better performance when compared with lithium carbonate ($Li_2CO_3$) and $K_2CO_3$ doped sorbents. The doping of MgO sorbents with $CaCO_3$ is also reported in literature as improving its sorption performance. Yang et al (2016) suggested that the introduction of $CaCO_3$ either increased the thermodynamic equilibrium temperature to higher ranges or decreased the equilibrium's $CO_2$ partial pressure at the same temperature [26]. Both evidence were attributed to the formation of the double salt dolomite ($CaMg(CO_3)_2$) [10].

An accidental $Na_2CO_3$-MgO sorbent's contamination with sodium nitrate ($NaNO_3$) revealed its enhanced $CO_2$ sorption performance and, thus, it aroused interest in the alkali nitrate/ nitrite doping [10]. Zhang et al. doped MgO sorbents with $NaNO_3$ exhibiting good $CO_2$ sorption performance and made novel progress by presenting a new reaction mechanism [27]. Experimental results showed a MgO sorbent doped with $NaNO_3$ exhibiting good $CO_2$ sorption kinetics and a MgO conversion of 75 % against of only 2 % for an undoped MgO, both at 330 °C and ambient pressure. It was stated that molten $NaNO_3$ provides an alternative reaction pathway to traditional gas-solid reactions, by acting as a phase transfer catalyst (PTC) between bulk MgO and $CO_2$ molecules which, in turn, facilitates the sorption reaction. It was described as the promoting effect of the molten nitrate. This evidence was then extended to other molten salts and metal oxides [27].

At sorption temperatures higher than the melting point of $NaNO_3$ (~308 °C [25]), it is in a molten state, so it acquired the ability to dissolve bulk MgO. This dissolution of some MgO in the molten nitrate forms dissociated ions pairs of $Mg^{2+}$ and $O^{2-}$. At this stage, the interactions are weaker when compared to those of bulk MgO. Simultaneously, $CO_2$ molecules weakly adsorb on the bare MgO surface as mono- or bi-dentate carbonate species and migrate to the formed triple phase boundaries (TPB), where the reaction between the adsorbed $CO_2$ molecules and the dissociated ions pairs of $Mg^{2+}$ and $O^{2-}$ takes place. New ionic pairs of $Mg^{2+}$ and $CO_3^{2-}$ form and subsequently precipitate as solid $MgCO_3$ as saturation level is reached. It was established a dynamic MgO dissociation/precipitation equilibrium that activates the MgO bulk solid lattice, by producing MgO species capable of absorb easier the $CO_2$ molecules at the most efficient reaction sites provided by the gas-solid-liquid TPB [27]. The explained mechanism is illustrated in Figure 2-5.

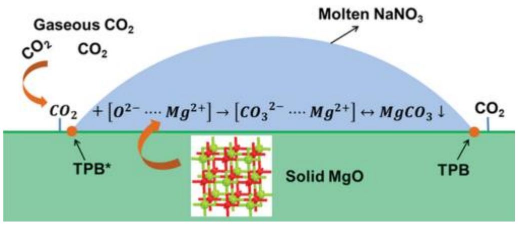

**Figure 2-5 – Schematic diagram of molten $NaNO_3$ as phase transfer catalyst of $CO_2$ sorption by alkali nitrate/ nitrite doped MgO-based sorbent. [27]**

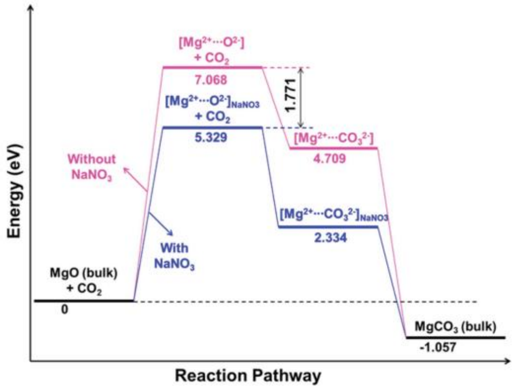

**Figure 2-6 – Born-Haber Cycles of $CO_2$ sorption by undoped MgO and by alkali nitrate/ nitrite doped MgO-based sorbent. [27]**

As shown in Figure 2-6, the activation of the MgO ionic bond is the rate-controlling step. It is actually the existence of a molten phase that decreases the dissociation energy of Mg-O ionic bonds in bulk MgO. In fact, to overcome the high lattice energy barrier associated to bulk MgO for carbonation to occur is the primary role of nitrates. In addition, molten alkali metal nitrates are shown to prevent the formation of a rigid, $CO_2$-impermeable, and monodentate carbonate layer on the surface of MgO as it occurs with bare MgO, but to promote the rapid generation of carbonate ions to allow a high rate of $CO_2$ uptake. Therefore, the doping with $NaNO_3$/ $NaNO_2$ improves the $CO_2$ sorption performance of MgO sorbents. The subsequently accumulation of $MgCO_3$ in the sorbent surface hinders the sorption process due to the increasing diffusion resistance of both $O^{2-}$ and $CO_3^{2-}$ from the $MgCO_3$ forming layer [10,12,25,27].

It is stated in literature that nitrite salts are associated with higher efficiency in the enhancement of both the sorption rate and the sorption capacity of MgO sorbents, when compared to nitrates, because of the higher concentration of $O^{2-}$ ions that the former can provide. It is also very well-stablished that the addition of alkali metal nitrates does improve the $CO_2$ uptake capacity of MgO-based sorbents. Yet, there's no great consensus on the sorption mechanism. In addition, it is not currently understood which properties of the nitrates influence the $CO_2$ uptake, besides the fact that is mandatory to have a molten phase [10,12,25].

Zhao et al. reported that a mesoporous MgO sorbent doped with $NaNO_3$ suffered a reduction of both surface area and pore size after carbonation and regeneration. Nevertheless, other recent works suggest that the loss of $CO_2$ sorption capacity can either be due to morphological changes or be related to partial dewetting on MgO surface [25].

Concerning the binary or ternary alkali doping, very promising evidence is found in literature. Lee et al. studied the $Na_2CO_3$/ $NaNO_3$-doped MgO sorbent that maintained a high $CO_2$ sorption capacity of 153 mg $CO_2$/ mg sorbent after multiple cycles [28]. Such good performance is believed to be related with the interaction established between MgO, $CO_2$ and the molten $NaNO_3$ that results in the formation of the double salt $Na_2Mg(CO_3)_2$. Identical results were registered for other cases of binary doping, such as, $K_2CO_3$/ $KNO_3$-doped MgO sorbents. Zhang et al. gave a detailed explanation for the enhancement of $CO_2$ sorption capacity of MgO sorbents doped with the binary $Na_2CO_3$/ $NaNO_3$ system [29]. The mechanism is stated to be similar to that of the single alkali nitrate. Bulk MgO dissolves in the molten salt because Mg-O ionic bonds are easy to break. $Na_2CO_3$ also dissolves in the same liquid medium because carbonate salts have good solubility in molten salts. Hence, ion pairs of $Mg^{2+}$, $O^{2-}$ and $CO_3^{2-}$ are formed and react with $CO_2$ molecules, generating the double salt ($Na_2Mg(CO_3)_2$). Same mechanism is appropriated to binary alkali nitrate/ carbonate doping that forms the $CaMg(CO_3)_2$ double salt [10,29].

The binary doping with alkali nitrate/ nitrite is also an interesting matter of study. Zhao et al. compared the $CO_2$ sorption capacities of the single $NaNO_3$ and of the binary $NaNO_3$/ $NaNO_2$ doped MgO sorbents [30]. The latter showed higher $CO_2$ sorption capacity than the former. This new evidence found explanation on the reduction of the melting temperature of the eutectic mixture. While single $NaNO_3$ and $NaNO_2$ present a theoretical melting point of 308 °C and 271 °C, respectively, the eutectic mixture of $NaNO_3$/ $NaNO_2$ exhibit a melting temperature of 185 °C. Thus, the eutectic mixture facilitates the sorption process by providing a molten phase that works like a liquid channel. Ternary doping with $NaNO_3$, lithium nitrate ($LiNO_3$) and potassium nitrate ($KNO_3$) registered an even more accentuated reduction of the eutectic mixture's melting point and an enhanced $CO_2$ sorption performance. In the case of the ternary doping with $LiNO_3$, $NaNO_3$ and $Na_2CO_3$, the former two form the molten phase in which $Na_2CO_3$ dissolves along with the bulk MgO to react with the $CO_2$ molecules [10,30]. Though it is well accepted that the melting temperature of the eutectic mixture impacts greatly the $CO_2$ sorption performance, it is reported in literature that MgO sorbents containing $NaNO_3$ maintained a quite stable $CO_2$ sorption capacity when deviating from the eutectic [25].

Summarizing, doping with AMS improves the cyclic $CO_2$ sorption capacity of MgO sorbents, when compared to that of commercial MgO, mesoporous MgO and MgO obtained from different precursors. Nevertheless, the majority of the AMS doped MgO sorbents exhibit a last-cycle $CO_2$ sorption capacity that is only 70 % of the theoretical maximum capacity [10].

Table 2-1 presents some selected studies found in literature using unsupported and supported MgO-based sorbents undoped and AMS doped and the corresponding $CO_2$ sorption capacity after multicyclic tests using a TGA or a reactor.

**Table 2-1 – Sorption performance and experimental conditions of unsupported and supported MgO-based sorbents impregnated with AMS reported in literature.**

| MgO-based sorbent | | Sorption test method | Temperature (°C)/ Atmosphere/ Time (min) | | Number of cycles | $CO_2$ sorption capacity (mg $CO_2$ / g sorbent) | | Ref. |
|---|---|---|---|---|---|---|---|---|
| | | | Sorption | Desorption | | Initial | Final | |
| **Unsupported: (% mol) AMS – MgO** | 10 $NaNO_3$ – MgO | TGA | 300/ 10 vol % $CO_2$/ 180 | 300/ He/ 180 | 5 | 390 | 210 | [31] |
| | 10 $NaNO_3$ – MgO | TGA | 450/ $N_2$/ 30 | 300/ $CO_2$/ 30 | 20 | 140 | 100 | [32] |
| | 10 (Li, Na, K)$NO_3$ – MgO | TGA | 300/ $CO_2$/ 60 | 450/ $N_2$/ 15 | 5 | 480 | 410 | [25] |
| | 15 (Li, Na, K)$NO_3$ – MgO | TGA | 300/ $CO_2$/ 60 | 350/ $N_2$/ 30 | 5 | 440 | 350 | [33] |
| | 15 (Li, Na, K)$NO_3$ – MgO | TGA | 300/ $CO_2$/ 60 | 350/ $N_2$/ 30 | 12 | 440 | 310 | [33] |
| | (Li, K)$NO_3$ + ($Na_2$,$K_2$)$CO_3$ – MgO | Packed bed reactor | 325/ 80 % $CO_2$ + 20 % $N_2$/ 30 | 400/ $N_2$/ 30 | 8 | 410 | 325 | [34] |
| **Supported: (% mol) AMS – MgO – (% mol) porous support** | 20 (Li, Na, K)$NO_3$ – MgO-5 Ca | TGA | 300/ $CO_2$/ 30 | 425/ $N_2$/ 10 | 5 | 396 | 330 | [35] |
| | 12 (Li, Na, K)$NO_3$ – MgO-10 Ce | TGA | 300/ $CO_2$/ 60 | 425/ $N_2$/ 15 | 5 | 340 | 180 | [36] |
| | 17 (Li, Na, K)$NO_3$ – MgO-10 Ce | TGA | 300/ $CO_2$/ 60 | 425/ $N_2$/ 15 | 5 | 420 | 330 | [36] |

### 2.2.2 EXTRINSIC FACTORS

Besides developing solutions for reducing the drawbacks related to sorbents' intrinsic properties, researchers also investigate the influence of extrinsic factors in the $CO_2$ sorption, in order to optimize the following operational conditions:

- $CO_2$ concentration;
- Pressure;
- Presence of water, and;
- Gas impurities.

The effect that the **$CO_2$ concentration** has on the performance of MgO-based sorbents is perceived both at the sorption and desorption steps. At the sorption step, $CO_2$ concentration acts as the driving force for an effective $CO_2$ diffusion and sorption, with a higher $CO_2$ concentration providing a higher contact between $CO_2$ and MgO molecules and, thus, smoothing the sorption process. Yang et al. reported a significant decrease in the sorption rate of sodium-doped MgO sorbents with the changing of the $CO_2$ concentration from pure to 80 % ($N_2$ balance). Zhang et al. also reported a serious decrease in the sorption capacity of bimodal mesoporous carbon-coated MgO when using a $CO_2$ partial pressure of 10 % [10].

In parallel with what happens to solid sorbents like CaO and $Li_4SiO_4$, the regeneration of MgO sorbents should occur under high concentrations of $CO_2$ to guarantee that the outlet stream of the desorption reactor is $CO_2$ concentrated and ready to be compressed and sent to storage. Currently, this procedure is still not followed in the works reported in literature. The carbonated MgO-based sorbents are usually regenerated in an atmosphere of pure $N_2$. Hwang et al. (2018) carried out one of the few preliminary tests on the effect that the desorption gas composition has on the regeneration of the sorbent. The results remained undefined though. In addition, it was described that the desorption temperature dramatically increased from 430 °C to 620 °C when the desorption atmosphere went from pure $N_2$ to pure $CO_2$. This evidence came out as a challenge. The increasing concentration of $CO_2$ at the desorption step increases the desorption temperature, as shown in Figure 2-2, which, in turn, causes the sintering of the MgO-based sorbent and, thus, affects its $CO_2$ uptake [10].

Currently, SEWGS processes undergo at high **pressures** [10]. Thus, a $CO_2$ separation unit of a SEWGS process demands MgO-based sorbents to remain stable its cyclic $CO_2$ uptake capacity at high pressures. Hwang et al. (2018) investigated the effect of the operation pressure in the $CO_2$ uptake capacity of a MgO-based sorbent impregnated with alkali metal nitrates under multiple cycles [37]. The obtained experimental results showed a general upward profile of the $CO_2$ uptake capacity with increasing operation pressure: the $CO_2$ uptake capacity increased dramatically from 1 to 20 atm, while a more discreet increase was registered from 20 to 30 atm. This fact was attributed to gaseous diffusion being mainly controlled by Knudsen diffusion at higher pressures. An MgO-based sorbent impregnated with 5 % of $NaNO_3$ plus 5 % of $KNO_3$ was able to maintain stable its $CO_2$ uptake capacity at 400 mg $CO_2$/ g sorbent after five cycles at 300 °C and 20 atm. It was concluded it was an adequate sorbent to be used in a SWEGS process at high pressures. In addition, it was reported that working at higher desorption pressure results in a higher desorption temperature needed for the regeneration of the sorbent [10].

Zarghami et al. (2015) investigated the effect of the **presence of $H_2O$** on the reactivity of MgO-based sorbents [38]. The experimental results demonstrated that the existence of steam in the sorption step had a positive influence in the rate of the carbonation reaction. Water is believed to work as a co-sorbent that boosts $CO_2$ chemical reactivity, by creating a new carbonation pathway consisting of two mechanisms [12]. The primary mechanism forms an alternative transient compound, $Mg(OH)_2$, with larger molar volume than that of MgO, (equation (10)). The secondary mechanism acts at the pore structural level, by expanding the inner pore volume and, thus, diminishing the resistance through diffusion in its inside (equation (11)) [10,12]. The overall result is the higher reactivity of the MgO-based sorbent toward $CO_2$, that is, higher $CO_2$ uptake capacity.

$$MgO\ (s) + H_2O\ (g) \rightleftharpoons Mg(OH)_2\ (s) \tag{10}$$

$$Mg(OH)_2\ (g) + CO_2(g) \rightleftharpoons MgCO_3(s) + H_2O \tag{11}$$

The kinetics of the reaction between $CO_2$ and $Mg(OH)_2$ described in equation (11) is faster than that of the reaction between $CO_2$ and MgO described in equation (1). The capture of $CO_2$ with $Mg(OH)_2$ is an exothermic reaction with an ΔH of – 19.657 kJ/ mol. The reaction of MgO with $CO_2$ is also an exothermic reaction, but its ΔH is – 100.895 kJ/ mol, a much higher absolute value. Moreover, to capture $CO_2$ with $Mg(OH)_2$ at high temperature is faster than with MgO. Researchers deduce that the presence of water provokes the rearrange of surface oxide to hydroxide over MgO molecules, producing $Mg(OH)_2$. This transient species has weaker lattice bonds when comparing to MgO, which smooths the transfer ability of $OH^-$ more than $O^{2-}$. $Mg(OH)_2$ registered an absorption capacity of 148 mg $CO_2$/ g sorbent, but its operation is limited to the temperature window of 200 – 315 °C and requires the rehydroxylation of MgO in the sorbent regeneration [14,18]. In addition, the existence of water decreases the operating temperature. Thus, the regeneration of $MgCO_3$ into $Mg(OH)_2$ represented in equation (12) can undergo at lower temperatures [10,12,38].

$$MgCO_3(s) + H_2 + CO_2(g) \rightleftharpoons Mg(OH)_2\,(g) + H_2O \tag{12}$$

It is described in literature that alkali-based sorbents that were pretreated with water showed a clear advantage for $CO_2$ capture (Figure 2-7) [12]. Yang et al. also found that the presence of $H_2O$ during the sorption step improved the kinetics of sorption rates [10]. In addition, it is also reported that the introduction of $H_2O$ at the desorption step could have benefits in the improvement of both regeneration rate and efficiency of MgO-based sorbents [10]. Other studies indicate that water vapor in both pretreatment and $CO_2$ adsorption stages help to reach the optimal $CO_2$ capture capacity [12]. These results support the introduction of a steam pretreatment of MgO sorbents preceding the sorption or of a steam regeneration of the carbonated MgO-based sorbents in industrial applications, for example, in IGCC typical processes or in coal-fired power plants [10]. Zarghami et al reported that an increasing of 20 bar in the pressure system plus adding 30 % (v/v) of water vapor enhances the rate of carbonation, resulting in a close complete conversion of the MgO sorbent [38].

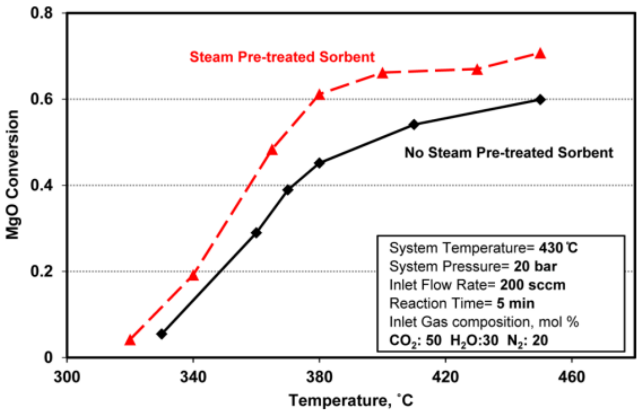

**Figure 2-7 – Influence of steam pretreatment on the reactivity of the MgO-based sorbent.** [38]

Concerning to typical **gas impurities**, Li et al. reported that $SO_2$ is a strong acid when compared to $CO_2$ and, consequently, the former will preferably occupy the strong basic sites of the MgO-based sorbent [39]. It is a case of sorbent's poisoning. In this sense, the presence of $SO_2$ at the sorption step will negatively impact the $CO_2$ uptake. This evidence supports that the desulfurization of flue gas prior to contact with MgO-based sorbents should be implied in industrial processes [10].

## 2.3 PROMISING APPLICATIONS FOR MAGNESIUM OXIDE BASED SORBENTS

In terms of CCS promising applications, MgO-based sorbents have been used in both post and pre-combustion $CO_2$ capture technologies [12]. Due to the fact that MgO is an intermediate-temperature sorbent, it can be used for capturing $CO_2$ from outlet gas streams of water gas shift reaction (WGSR) (equation (13)) and SMR (equation (14)), as well as for the SEWGS, where it captures $CO_2$ and maximizes $H_2$ generation in simultaneous [36].

$$CO(g) + H_2O \rightleftharpoons CO_2(g) + 4H_2(g) \tag{13}$$

$$\Delta H = -41 \ kJ/mol$$

$$CH_4 + H_2O \rightleftharpoons CO + 3H_2 \tag{14}$$

$H_2$ is the most promising alternative to fossil fuels as carbon-neutral clean energy vector, due to its higher energy density, that is, calorific value, and absence of pollutants production when converted to other types of energy. Currently, the $H_2$ production is 50 Mt/ year. Concerning to applications, $H_2$ is a raw-material largely used in the chemical industry and refineries, such as, the chemical synthesis of ammonia and urea, hydrocracking and hydrotreating in oil-upgrading, and in fuel for vehicles [40–41].

Traditionally, the production of $H_2$ is made via SMR from a methane source, such as natural gas, and using high-temperature steam (700 – 1000 °C). In addition, WGSR using syngas feedstock derived from a gasified carbonaceous from coal or biomass is also becoming a very common via to generate $H_2$. At low temperatures, the WGSR is thermodynamically favored, since its equilibrium constant decreases as temperatures increases, but not kinetically, as it is an exothermic reaction. In order to overcome this contradiction, the WGSR combines a two-step operation, that is, high-temperature (HT)WGS ranging from 350 °C to 450 °C that provides high reaction rates; and low temperature (LT)WGS running from 200 °C to 250 °C that improves CO conversion. In recent years, the sorption enhanced reaction (SER) has been applied, aiming to improve the performance of either the WGSR and the SMR, leading to SEWGS or to sorption enhanced steam methane reaction (SESMR), respectively [41–42].

The SEWGS consists of a WGSR with in-situ $CO_2$ capture by sorption occurring simultaneously in a single reactor. According with equation (13), the implementation of in-situ $CO_2$ removal shifts the WGSR to its right side by capturing the $CO_2$ and, thus, increasing the $H_2$ yield. That is to say that in-situ $CO_2$ capture overcomes the limitations related to the equilibrium, resulting in both higher $CO_2$ conversion and enhanced $H_2$ production. It is the Le Chatelier's principle. The result is the production of a very high-purity $H_2$ without the elevated costs associated to a separation process and a much more compact and simple process, that is, SEWGS is associated with higher energy system efficiency and lower capital costs than WGSR. Hence, SEWGS is considered a promising pre-combustion $CO_2$ capture technology. Moreover, the integration of SEWGS in an IGCC is appointed to be a favorable solution to reduce $CO_2$ emissions derived from coal-based power plants. There are also benefits associated to operating costs that unfold from the combination of IGCC [40–41].

The success of the SEWGS is highly dependent on the sorbent selected for the in-situ $CO_2$ capture from the reaction medium. The adequate materials for this technology are exclusively intermediate-temperature solid sorbents. For example, hydrotalcite and modified hydrotalcite-based sorbents exhibited low $CO_2$ sorption capacity of less than 100 mg $CO_2$/ g sorbent at intermediate to high temperatures in SEWGS, causing $CO_2$ saturation and reducing $H_2$ production. MgO-based sorbents have also been applied in the enhanced $CO_2$ removal from WGSR, due to being associated with low cost, wide availability and high theoretical sorption capacity. Moreover, the integration of MgO-based sorption/ desorption process allows to remove the $CO_2$ at lower temperatures, that is, ranging from sorption to regeneration temperatures of 300 to 450 °C, respectively, without the need of LTWGS. AMS-promoted MgO-based sorbents exhibit much higher $CO_2$ capture than hydrotalcite-based sorbents. Yet, MgO-based sorbents performed worse in practical applications, showing an abrupt decrease of the sorption capacity under long-term cyclical operation, because of the already mentioned product layer formation, sintering, attrition and potential competing sulphation reactions (when there is a high in sulfur feedstock). In fact, there is no record of pilot-scale projects in this arising area. All the presented evidence and challenges derive from experimental tests at laboratories [10,40–42].

It is reported in literature the utilization of a $Na_2CO_3$/ $NaNO_3$-doped MgO sorbent in the $CO_2$ capture of a WGSR aiming to obtain $H_2$. It was successfully obtained high-purity $H_2$ directly from the SEWGS reaction. Because it was performed one cycle of SEWGS, it was not possible to conclude about the cyclic stability. Further investigations employed a $LiNO_3$/$KNO_3$/$Na_2CO_3$/$K_2CO_3$/$CaCO_3$-doped MgO sorbent in a WGSR for in-situ $CO_2$ capture. The sorbent showed high sorption capacity, good sorption kinetics and stability after 30 cycles. It was also obtained very high-purity $H_2$ (99.4 % dry basis) at 300 °C and 12 atm. After 10 cycles, it was proved good cycling stability by obtaining very high-purity $H_2$ with a purity of 98.2 % [10]. Another work reported a Na-Mg double salt MgO-based sorbent with good sorption kinetics, excellent cyclic stability and high sorption capacity of 132 mol/ kg in the temperature range required for WGSR, that is, 200 – 400 °C [41].

Recent work describes the preparation of $K_2CO_3$-promoted Cu/MgO-$Al_2O_3$ by sol-gel method to be used in a SEWGS reaction. Very much promising results were obtained for a sorbent with a K/(Mg + Al) ratio of 0.2 and Mg/Al ratio of 9. It was registered and $H_2$ yield of 99.9 % after 10 SEWGS/ regeneration cycles at 300 °C and 380 °C for SEWGS and for regeneration, respectively [43].

It is also described in literature a study on the influence of the catalyst packing method in the $CO_2$ removal of a WGSR, using a Na-Mg double salt as sorbent and a commercial catalyst. In a first attempt, it was successfully synthesized a one-body hybrid solid, consisting of both catalyst and sorbent. However, it exhibited low sorption capacity when compared to that of single materials. Subsequently, it was adopted a divided section concept that minimized the contact between the catalyst and the sorbent by alternatively filling the sections of the reactor with each. This attempt generated high-purity $H_2$ by SEWGS. Moreover, higher production of high-purity $H_2$ was registered when using higher ratio of sorbent-to-catalyst, as higher concentrations of $CO_2$ were being capture, that is, SER. It was also observed that the SEWGS performance improved with the increasing number of the reactor sections. Further investigations using a reactor packing method that consists of former sections with higher catalyst-to-sorbent ratio and later sections with higher sorbent-to-catalyst ratio were proposed [41]. SEWGS experiment performed in a fixed-bed reactor using AMS-promoted MgO-$CaCO_3$ as sorbent is also reported in literature. It successfully produced high-purity $H_2$ (99.4 % in dry basis) at 573 K, 12 atm and for an initial $H_2O$/ CO molar ratio of 1.5 in a three layer of catalyst/sorbent configuration. It exhibited good cyclic stability after 10 consecutive cycles [42].

## 2.4 THERMAL DECOMPOSITION OF ALKALI NITRATE SALTS

Several studies on the thermal decomposition of molten salts are found in literature, since they are often implemented in Concentrating Solar Power (CSP) plants as heat transfer fluids (HTF) [44]. Solar Salt, a binary mixture consisting of 40 wt.% $KNO_3$ and 60 wt.% $NaNO_3$, and Hitec, a ternary mixture of 53 wt.% $KNO_3$, 7 wt.% $NaNO_3$ and 40 wt.% $NaNO_2$, are the nitrate salt mixtures most used as HTF [45]. $LiNO_3$ is also often added to these mixtures, so their melting point decreases and, thus, their working temperature range increases [45]. Yet, there is still lack of consensus concerning to both thermal decomposition temperature and mechanisms [44].

The alkali nitrate/ nitrite thermal decomposition mechanism is investigated since the 1960s. They are both associated with benefits such as low cost, low viscosity and high heat capacity. However, this binary molten salt mixture cannot be used at temperatures above 550 °C, due to thermal decomposition and insignificant vapor pressure [44].

The thermal decomposition of molten nitrate salts is described in literature considering three different temperature ranges. First, at temperatures higher than the melting point, the nitrate formation occurs in the melt with oxygen release as described in equation (15), considering its equilibrium constant $K_1$ given by equation (16). In this range, a minor quantity of nitrite is found. General consensus exists only for this first mechanism. [45–46].

$$NO_3^- \rightleftharpoons NO_2^- + 1/2O_2 \tag{15}$$

$$K_1 = [NO_2^-]\left(P_{O_2}\right)^{1/2}/[NO_3^-] \tag{16}$$

Next, between 450 °C and 600 °C, a secondary nitrate thermal decomposition takes place as described in equations (17) and/ or (18). The formed nitrites react to produce oxides with the release of nitrogen or nitrogen oxides. Here, the partial pressure of the atmospheric oxygen in contact with the molten salt limits the dissociation of the nitrate in nitrite [45–46].

$$2NO_2^- \rightleftharpoons O^{2-} + NO_2 + NO \tag{17}$$

$$2NO_2^- \rightleftharpoons O^{2-} + N_2 + NO_3 \tag{18}$$

Eventually, the formed $O^{2-}$ ions react with $CO_2$ molecules to form carbonates, according to equation (19).

$$CO_2 + O^{2-} \rightarrow CO_3^{2-} \tag{19}$$

Finally, at high temperatures ranging from 650 °C to 700 °C, the decomposition continues with the vaporization of nitrate salts to form $NO_x$ species [45–46].

Previous works in literature suggest preserving the molten nitrate salt mixtures from atmospheres containing oxygen [45]. In fact, in the absence of $O_2$ atmosphere (left), the equilibrium is favored towards the formation of $NO_3^-$, according to equation (15). In line with the latter, Bradshaw reported a gradual diminution of the concentration of $NO_2^-$ with an increasing of the melting temperature under atmospheres containing 10, 20 and 40 % of $O_2$ [47].

The presence of $N_2$ is also a matter of study. Considering an atmosphere containing $N_2$ (left side of the reaction described in equation (20)), the equilibrium can be shifted towards $NO_2$ formation with limited concentration of $O_2$ and with the kinetics favoring the nitrite formation. On the contrary, an atmosphere saturated in $O_2$ favors the nitrate formation (right), with ΔG = - 221.4 kJ [45].

$$1/2N_2 + 3NO_3 \rightleftharpoons 4NO_2 + 1/2O_2 \tag{20}$$

$$\Delta G_{550\,°C} = -493.5\ kJ$$

Stern describes in literature the effect of single nitrate salts in thermal stability [48]. $KNO_3$ exhibits the highest stability followed by $NaNO_3$, decomposing at 530 °C and at 500 °C in air, respectively. $LiNO_3$ appeared as the least stable of the three, because it decomposes itself in lithium nitrite ($LiNO_2$) right after its melting temperature. In addition, nitrates are more stable than nitrites at higher temperatures. Note that the decomposition of sodium nitrite ($NaNO_2$) occurs at temperatures above 330 °C. This defined increasing stability order follows the increasing cation radius of the periodic table (K > Na > Li), because of the increasing polarization effect that interferes with the distribution of the electron in the anion [45].

The decomposition of both nitrate and nitrites will originate different oxide ions according with the salts consisting of the mixture, the temperature and other experimental conditions. It is described in literature that oxides, peroxides and superoxides are decomposition products. The decomposition of $NaNO_3$, $LiNO_3$ and $KNO_3$, forms sodium oxide ($Na_2O$), lithium oxide ($Li_2O$) and potassium oxide ($K_2O$), respectively [45]. Stern adds other gaseous decomposition products, namely, $O_2$, $N_2$, nitrogen monoxide (NO), nitrogen dioxide ($NO_2$), dinitrogen trioxide ($N_2O_3$), dinitrogen tetroxide ($N_2O_4$) and dinitrogen pentoxide ($N_2O_5$) [48].

In addition, atmospheric carbon dioxide also represents a concern, since it can react with the produced oxygen ions to form carbonates, as described in equation (19). For being insoluble, carbonates are often associated with obstruction problems in pipes or valves. On the other hand, the soluble oxide species are related to the aggravation of corrosion phenomena at high temperatures by interacting with the containers' materials [45,49]. Bradshaw verified that ternary salts mixtures with $LiNO_3$ generate higher concentrations of oxide ions at high temperatures, namely, lithium peroxide ($Li_2O_2$) and $Li_2O$, when comparing to that of binary salts mixtures [50].

# 3 MATERIALS AND METHODS

## 3.1 MATERIALS

### 3.1.1 SYNTHESIS OF UNSUPPORTED AND SUPPORTED MAGNESIUM OXIDE BASED SORBENTS

Two different types of sorbents were used in the research carried out in this master thesis: unsupported and supported MgO sorbents. Both types were prepared via the sol-gel method. Two different temperatures were tested in the synthesis of the unsupported sorbents: 60 °C and 80 °C. Supported sorbents were synthesized at 80 °C.

With respect to unsupported MgO sorbents' preparation, magnesium nitrate hexahydrate ($Mg(NO_3).6H_2O$) from Sigma-Aldrich (assay of 98 – 102 %) and citric acid monohydrate ($C_6H_8O_7.H_2O$) from Panreac (assay of 99.5 – 102 %) were dissolved in distillate water, with a molar ratio of citric acid and distillate water to magnesium of 1:1 and 120:1, respectively.

Relatively to supported MgO sorbents, two different types of supports were used: calcium nitrate tetrahydrate ($Ca(NO_3)_2.4H_2O$) or cerium nitrate hexahydrate ($Ce(NO_3)_3.6H_2O$), both from Sigma-Aldrich (assay ≥ 99%). The followed procedure was similar to the one descripted above, with the addition of each support and considering a molar ratio of citric acid and distilled water to magnesium and calcium or cerium support of 1:1 and 120:1, respectively.

Each solution was continuously stirred in a silicone oil bath at 60 °C or 80 °C for 12 h or 6 h, respectively. Subsequently, the wet gel was dried in the oven at 120 °C for 14 h. After drying, the resultant sample was calcined in the muffle by ramping the temperature to 500 °C at a rate of 2 °C/ min plus 2 h more at 500 °C.

Figure 3-1 schematizes the synthesis procedure of supported and unsupported MgO-based sorbents.

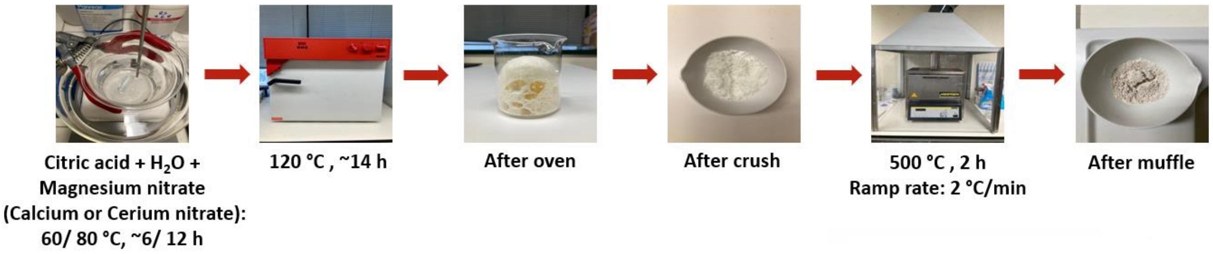

**Figure 3-1 – Synthesis of unsupported and supported MgO-based sorbents by sol-gel method.**

Table 3-1 summarizes the all-prepared samples of unsupported and supported MgO-based sorbents. For some MgO-SG samples it was needed to prepare more than one batch, namely, for the samples tested in the fixed-bed reactor (e.g., composite sorbent sample AMS-MgO-SG 5-9), where higher amounts of sorbent were used.

Table 3-1 – **Summary of the molar composition and synthesis temperature of unsupported and supported MgO sorbents.**

| Magnesium molar fraction (%) | Support molar fraction (%) | Synthesis Temperature ( °C) | Sample ID |
|---|---|---|---|
| 100 | 0 | 60 | MgO-SG 1<br>MgO-SG 4 |
| | | 80 | MgO-SG 5-9 (composed samples) |
| 90 | 10 Ce | 80 | MgO-Ca-SG |
| 90 | 10 Ca | 80 | MgO-Ce-SG |

### 3.1.2 DOPING WITH ALKALI METAL SALTS OF MAGNESIUM OXIDE BASED SORBENTS

Two different types of doping with alkali metal salts (AMS) were studied, namely, the mono AMS doping with sodium nitrate ($NaNO_3$); and the ternary AMS doping with a mixture of sodium nitrate, lithium nitrate ($LiNO_3$) and potassium nitrate ($KNO_3$). The used AMS reagents are from Sigma-Aldrich (assay ≥ 99%). The synthesized unsupported and supported samples of MgO sorbents were doped using the wet-impregnation method. Prior to the impregnation, the AMS were dried in the oven at 120 °C for 24 h.

The wet-impregnation procedure consisted of the suspension of both MgO-based sorbent and AMS in 20 mL of distillate water, using magnetic stir for 1 h at room temperature. The obtained aqueous slurry was dried in the oven at 120 °C for 14 h. Subsequently, the dried sample was placed in the muffle for calcination using a heating rate of 2 °C/ min until it reached 450 °C plus 4 h at 450 °C.

Figure 3-2 schematizes the AMS doping procedure of supported and unsupported MgO-SG based sorbents.

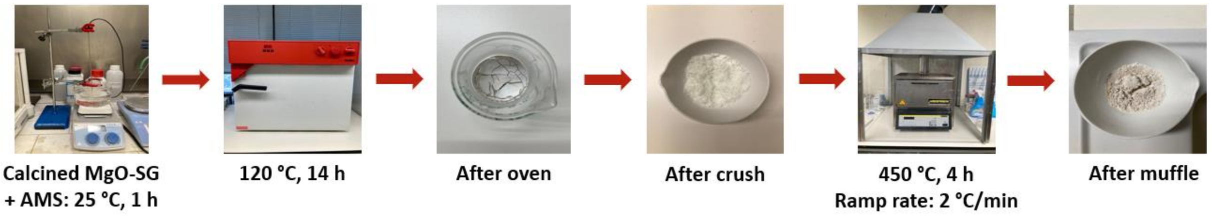

**Figure 3-2 – AMS doping of supported and unsupported MgO-based sorbents procedure.**

Different ratios of AMS-MgO-SG based sorbents were prepared. Table 3-2 summarizes all prepared AMS-MgO-based sorbents. The following nomenclature was used for the doped sorbent samples: x (Na or Na-Li-K)-MgO, where x corresponds to the molar fraction (%) of AMS, or x (Na-Li-K)-MgO-Y, where Y corresponds to the molar fraction (%) of Ca or Ce support.

**Table 3-2 – Summary of the molar composition of unsupported and supported AMS-MgO-based sorbents.**

| Sorbent precursor ID | AMS | | | |
|---|---|---|---|---|
| | $NaNO_3$ | | $(Na, Li, K)NO_3$ * | |
| | x | Sample ID | x | Sample ID |
| MgO-SG 1 | 30 | 30 Na-MgO | | |
| MgO-SG 4 | | | 10 | 10 (Na, K, Li)-MgO |
| | 15 | 15 Na-MgO | 15 | 15 (Na, K, Li)-MgO |
| | 25 | 25 Na-MgO | 25 | 25 (Na, K, Li)-MgO |
| | 35 | 35 Na-MgO | 35 | 35 (Na, K, Li)-MgO |
| MgO-SG-5-9 | | | 15 | 15 (Na, K, Li)-MgO |
| MgO-Ca-SG | | | 15 | 15 (Na, K, Li)-MgO-Ca |
| MgO-Ce-SG | | | 15 | 15 (Na, K, Li)-MgO-Ce |

* 18/30/52 of $NaNO_3/LiNO_3/KNO_3$ (wt.%)

## 3.2 CHARACTERIZATION METHODS

### 3.2.1 THERMOGRAVIMETRIC ANALYSIS

Thermogravimetric analysis (TGA) is a precise quantitative technique that measures the mass variations of a sample, either of a solid or low volatile liquid, as a function of time and temperature, following a defined temperature program and using a controlled gaseous atmosphere [51]. The device that does these measurements combines a sensitive analytical balance with an electronically programmed furnace and it is designated as thermobalance [52].

The TGA acquired data forms a thermogravimetric integral curve (TG curve) in which mass change is plotted against time or temperature. The differential TG curve (DTG curve) is its derivate with respect to time plotted against time or temperature. In the latter, down and upward peaks will be obtained, representing either loss or gain of mass, respectively [52], as it is shown in Figure 3-3.

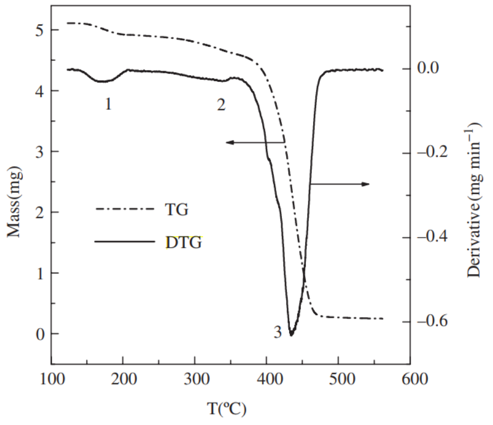

**Figure 3-3 – TG and DTG curves example.** [52]

The experimental unit used for the TGA studies conducted in this master thesis was the TG-DSC sestsys Evo 16 – SETARAM analyzer (Figure 8-1, section 8.1, appendix) and the software used for the data processing was Calisto.

### 3.2.2 X-RAY POWDER DIFFRACTION

X-ray powder diffraction (XRD) is an analytical technique that identifies the phase of a crystalline material, providing information about the unit cell dimensions and atomic spacing. The device that does this analysis contains an X-ray tube, a sample holder and a X-ray detector and it is called X-ray diffractometer [53–54].

The fundamental principle of XRD technique is the constructive (on phase) interference that occurs when a beam of monochromatic X-rays produced in the cathode ray tube hits the electrons in the crystalline sample, generating diffracted rays that verify the Bragg's Law (equation (21)). These contain data about the electron distribution in the sample nanoparticles, so are then collected, processed and counted [54–55].

$$n\,\lambda = 2\,d\,sin\,\theta \tag{21}$$

Where n is the order of reflection (an integer); λ is the wavelength of X-rays; d is the interplanar spacing of the crystal; and θ is the incidence angle at which constructive interference occurs [55].

The scan of the sample through a range of 2θ angles reaches every diffraction direction of the lattice, owing to the arbitrary orientation of the sample. By converting the diffraction peaks to d-spacings, one identifies the mineral specie [53].

The equipment used in the XRD experimental works of this master thesis was the Bruker D8 Advance Powder X-ray diffractometer (Figure 8-2, section 8.1, appendix) set up with a 1D detector (SSD 160), a Cu Kα (λ = 0.15406) and a Ni filter. It was operated at 40 kV and 30 mA, considering a scanning angle (2θ) window from 5° to 80° with a step size of 0.03° and a step time of 0.5 s. The Crystallography Open Database (COD) was subsequently used to identify the sample crystalline phases, by comparing the obtained d-spacings with the reference patterns.

The study of the sorbents' crystallite size is a subject of this research, and its determination was made using Scherrer's equation (equation (22)):

$$D = \frac{K\,\lambda}{\beta\,cos\,\theta} \tag{22}$$

Where D is the average dimension of crystallites (in nm); K is the Scherrer constant that ranges between 0.70-1.70, depending on crystal shape (0.9, assuming spherical particles); λ is the wavelength of X-rays (0.15406 nm); and β is the full width (in radians) at half maximum peak height (located at 2θ) [56].

### 3.2.3 NITROGEN ADSORPTION

Adsorption is defined as the “enrichment of molecules, atoms or ions in the vicinity of an interface” and it is designated as physisorption or chemisorption whether it is a case of physical or chemical adsorption, respectively [5].

Physisorption is defined as the general phenomenon where an adsorbable gas (the absorptive specie) contacts with the surface of a solid (the adsorbent specie) by establishing relatively weak forces named Van der Waals forces [54,57].

Concerning to physisorption, the International Union of Pure and Applied Chemistry (IUPAC) categorizes pores according to their width in micropores (< 2 nm), mesopores (between 2 – 50 nm) and macropores (> 50 nm). The nanopore term includes the latter three categories with an upper limit of 100 nm [57].

Gas adsorption is a well-established textural characterization technique of porous solids and fine powders.

IUPAC lists six types of physisorption isotherms (Figure 3-4) defined as follows [57]:

1. Reversible Type I isotherm: typical of microporous solids with relatively small external surfaces, specifically, with narrow micropores (with ≤ 1 nm) for type I (a) or with boarder pore size distribution (with < ~ 2.5 nm) for type I (b);
2. Reversible Type II isotherm: associated to nonporous or macroporous adsorbents, with unrestrained monolayer-multilayer adsorption; distinctive point B indicates complete monolayer coverage, while a more subtle curve corresponds to a situation of intense monolayer and start of multilayer adsorptions;
3. Type III isotherm: absence of monolayer formation; weak interactions between the adsorbent and the adsorbate; location of the absorbed molecules around the most favorable sites on the surface of a nonporous or macroporous solid;
4. Type IV isotherm: characteristic of mesoporous adsorbents with adsorption controlled both by adsorbent-adsorbate and in-between condensed molecules interactions; initial monolayer-multilayer adsorption similar to type II isotherm and followed by pore condensation; typical final saturation level; hysteresis in type (a) occurs when the width exceeds a critical width value depending on temperature and adsorption system, otherwise type IV (b) isotherm is observed;
5. Type V isotherm: similar to type III isotherm at low relative pressure, but with molecular agglomerating and pore filling at high relative pressure; common behavior of water adsorption on hydrophobic microporous and mesoporous adsorbents;
6. Type VI isotherm: typical of layer-by-layer adsorption on a uniform nonporous surface; each step-height refers to each adsorbed layer capacity; step’s sharp dependency on both the system and the temperature.

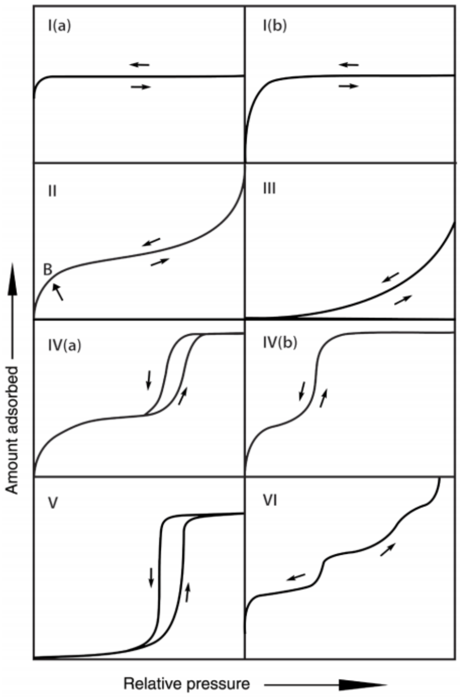

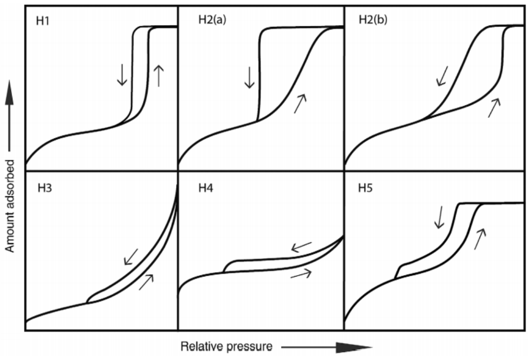

**Figure 3-5 – IUPAC classification of hysteresis loops. [57]**

**Figure 3-4 – IUPAC classification of physisorption isotherms. [57]**

When the adsorption and desorption curves do not coincide, adsorption hysteresis occurs. IUPAC categorizes hysteresis in five different types (Figure 3-5) explained as follows [57]:

1. Type H1 loop: abrupt and narrow loop associated with delayed condensation on the adsorption branch; typical of materials with a narrow range of uniform mesoporous and minimal network effects;
2. Type H2 loop: typical of more complex pore structures with important network effects; type H2 (a) steep desorption branch regards to pore-blocking in a narrow range pore necks or to cavitation-induced evaporation; type H2 (b) loop concerns to pore-blocking too, but in wider pore necks;
3. Type H3 loop: similar to type II isotherm adsorption branch; characteristic of non-rigid aggregates of plate-like particles and of macropores not completely filled with pore condensate;
4. Type H4 loop: composite adsorption branch of isotherms both types I and II; typical of mesoporous zeolites and micro-mesoporous carbons;
5. Type H5 loop: uncommon and characteristic of pore structures with open and partially blocked mesopores.

The device used in the experimental $N_2$ adsorption studies of this master thesis was the autosorb IQ of Quantachrome Instruments (Figure 8-3, section 8.1, appendix). It measured nitrogen adsorption under a temperature of – 196 °C ( ~ 77 K) and required a prior degasification process to prevent the sample to adsorb other gases or impurities. The followed procedure was performed under vacuum and consisted of two steps: the first one at 90 °C for 1 h and the second one at 350 °C for 5 h.

The ASiQwin software from Quantachrome was used to collect and analyze the data, that is, the sorbent's specific area ($S_{BET}$) using the BET method; the pore size distribution using BJH desorption model; and the total pore volume (Vp) at a relative pressure ($p/p_0$) of 0.95 using the nitrogen isotherm. The BET method calculates the $S_{BET}$ of a powder by physical adsorption of a gas on the solid's surface [54].

### 3.2.4 SCANNING ELECTRON MICROSCOPY

Scanning electron microscopy (SEM) is a technique that allows the visualization of "crystal shape, surface morphology, dispersed and agglomerated nanoparticles and surface functionalization's" [54]. A typical SEM apparatus is composed of a source of electrons, electromagnetic lenses, electron detectors, sample chambers, computers and displays to view the generated two-dimensional images. It requires vacuum to operate [54,58].

SEM analysis consists of a focused beam of accelerated electrons that hit the surface of the sample, losing kinetic energy and, thus, producing a variety of signals containing information on the sample [58]. Meanwhile, the sample is placed in a moving stage under vacuum, allowing its surface scan in all directions and angles [54].

The experimental device used for the required SEM measurements was the Phenom Pro G6 from Thermo Scientific (Figure 8-4, section 8.1, appendix). Samples were coated in a conductive adhesive containing Au-Pd in the form of a thin film to improve electron conductivity and, therefore, the quality of the obtained images.

## 3.3 NITRATE THERMAL DECOMPOSITION

The thermal decomposition of molten salts was assessed for the pure component $NaNO_3$ as well as the ternary mixture of 52 % (wt.) $KNO_3$, 18 % (wt.) $NaNO_3$ and 30 % (wt.) $LiNO_3$ by TGA under air and pure $CO_2$ atmospheres between 25 °C and 1000 °C at a heating rate of 10 °C/ min.

Molten salts are often associated with a set of features, such as, high hygroscopicity, high surface tension, high reactivity with crucible containers, and high melting points, originating the condensation of the melt on the measuring equipment. Hence, molten salts are described as being difficult to characterize in laboratory [46]. For this reason, the thermal decomposition of $KNO_3$ and $LiNO_3$ was not evaluated.

## 3.4 PRELIMINARY $CO_2$ UPTAKE TGA STUDIES CARRIED OUT WITH MAGNESIUM OXIDE BASED SORBENTS DOPED WITH ALKALI METAL SALTS

### 3.4.1 ASSESSMENT OF $CO_2$ SORPTION/ DESORPTION TEMPERATURE CONDITIONS

The first preliminary experiments performed in the TGA aimed to determine the optimal sorption and desorption conditions (Table 3-3). For these experiments it was used a constant flow of 80 ml/ min of $CO_2$, a ramp temperature of 10 °C/ min and ~10 mg of the 30 Na-MgO sample.

Concerning to sorption conditions, three different temperatures and two different time intervals were evaluated: 300 °C for 60 and 90 minutes, 325 °C and 350 °C, both for 60 min. With respect to desorption conditions, five different temperatures were tested for a time interval of 60 minutes: 420 °C, 430 °C, 435 °C, 440 °C and 445 °C.

**Table 3-3 – Experimental conditions used in the TGA during the sorption and desorption.**

| Sorption | | Desorption | |
|---|---|---|---|
| **Temperature (°C)** | **Time (min)** | **Temperature (°C)** | **Time (min)** |
| 300 | 90 | | |
| 300 | 60 | | |
| 325 | | | |
| 350 | | | |
| 300 | 60 | 420 | 60 |
| | | 430 | |
| | | 435 | |
| | | 440 | |
| | | 445 | |

### 3.4.2 ASSESSMENT OF MOLAR FRACTION EFFECT DURING MONO AND TERNARY ALKALI METAL SALTS DOPING

With both sorption and desorption temperature conditions defined, the next step aimed to find the most promising type of alkali metal salts doping, that is, mono or ternary AMS, as well as the best molar fraction of AMS salts/ MgO in each case.

Considering a window temperature from 20 °C to 500 °C, and a temperature ramp of 10 °C/ min, TGA studies were conducted on samples of MgO sorbent undoped and doped with mono or ternary AMS, that is, with $NaNO_3$ or with a ternary mixture of $NaNO_3$, $LiNO_3$ e $KNO_3$, respectively. Different proportions of both type of AMS were also considered. In the case of the mono AMS, MgO sorbent samples were doped with 15 %, 25 % or 35 %; while salts proportions of 10 %, 15 %, 25 % and 35 % were used in the ternary AMS doping case. During the experiments it was used a constant flow of 80 ml/ min of $CO_2$ and ~10 mg of sample.

The best two mono and ternary AMS samples, i.e., with higher $CO_2$ sorption capacity, were identified and selected to proceed the study by doing 5 sorption/ desorption cycles in the TGA as described in section 3.5.1. Based on TGA results, the sorbent with best $CO_2$ carrying capacity and stability was tested in the fixed-bed reactor as described in 3.5.2.

### 3.4.3 ASSESSMENT OF POROUS SUPPORT ADDITION

The effect of the addition of a porous support to the MgO sorbent doped with AMS was tested using Ca and Ce additions (10 %, mol). Samples of supported sorbent undoped and doped with ternary AMS (15 % mol) were tested in the TGA using the previous window temperature of 20 °C to 500 °C, and a temperature ramp of 10 °C/ min. It was used a constant flow of 80 ml/ min of $CO_2$ and ~10 mg of sample. The performance of supported sorbents was assessed along 5 sorption/ desorption cycles in the TGA and along 10 sorption/ desorption cycles in the fixed-bed reactor, as described in 3.5.1 and 3.5.2, respectively.

## 3.5 $CO_2$ SORPTION/ DESORPTION STUDIES

The results obtained for the assessment of the $CO_2$ sorption and desorption temperature conditions, of the mono and ternary AMS doping and of the porous support addition allowed to find the most promising sorption and desorption conditions, in what concerns to temperature, type and proportion of AMS.

### 3.5.1 TGA

A TGA (Figure 8-1, section 8.1, appendix) was used to conduct studies on the assessment of both stability and $CO_2$ uptake of the doped and undoped MgO sorbents. These tests consisted of 5 sorption/ desorption cycles with sorption and desorption temperatures of 300 °C and 445 °C, respectively, using a constant flow of 80 ml/ min of $CO_2$, a ramp temperature of 10 °C/ min and ~10 mg of sample.

The undoped sample showing best performance was identified and tested through 12 sorption/ desorption cycles under the same experimental conditions.

#### 3.5.1.1 EXPERIMENTAL PROCEDURE

The TGA unit consists of a chamber with a sample holder on its inside where a crucible containing the sample is placed.

The following experimental procedure was implemented:

1. Weight the empty crucible in an analytical scale and register the mass;
2. Tare the analytical scale and weight ~10 mg of sample;
3. Introduce the weighted mass of the sample in mg in the Calisto software, after subtracting the mass of the empty crucible from the mass of the crucible containing the sample;
4. Activate the cooling water and open the valve of the protective gas (Ar) (the pressure gauge is set to 2 bar);
5. Set the conditions of the experimental method as:
    a. Enter the number of sorption/ desorption cycles;
    b. Sorption conditions: 300 °C for 60 minutes with 80 ml/ min of $CO_2$ and a ramp temperature of 10 °C/ min;
    c. Desorption conditions: 445 °C for 60 minutes with 80 ml/ min of $CO_2$ and a ramp temperature of 10 °C/ min.

#### 3.5.1.2 ASSESSMENT OF $CO_2$ CAPTURE AND SORBENTS STABILITY DURING SORPTION/ DESORPTION CYCLES

The data file obtained at the end of each TGA cyclic test included the time in a step of 1.5 seconds, the temperature of the sample (°C) and the variation of the mass of the sample (mg). It was analyzed in a Microsoft Excel spreadsheet and plotted using the Origin software. Using the vertical cursor tool of the Origin, it was possible to extract both maximum mass gain and loss during sorption and desorption steps for each cycle, respectively. This mass variation resulted from the capture and release of $CO_2$ during sorption (direct) and desorption (indirect) reactions, respectively, as described in equation (1). These data allowed to determine the mass of $CO_2$ captured by the sorbent, i.e., the carrying capacity and the percentual MgO conversion using equations (23), (24) and (26), respectively.

$$m_{CO_2\ captured} = m_{sorption} - m_{desorption} \tag{23}$$

Where the $m_{CO2\ captured}$ is the mass of $CO_2$ captured in each cycle, $m_{sorption}$ is the mass of the sample after the sorption reaction and $m_{desorption}$ is the mass of the sample after the desorption reaction.

The carrying capacity (CC) of the sorbent is defined as the mass of $CO_2$ captured per unit mass of the dried sorbent (mg $CO_2$/ g sorbent).

$$CC = \frac{m_{CO_2\ captured}}{m_{sorbent}} \tag{24}$$

Where $m_{sorbent}$ is the mass of the sorbent sample.

The theoretical carrying capacity ($CC_{theoretical}$) is calculated with equation (25), according to the equimolarity of the sorption reaction described in equation (1), in which 1 mol of MgO can capture 1 mol of $CO_2$.

$$CC_{theoretical} = \frac{Mr_{CO_2}}{Mr_{MgO}} = \frac{44.01\ g/mol}{40.30\ g/mol} = 1.09 \tag{25}$$

Where $Mr_{CO2}$ and $Mr_{MgO}$ represents the molar mass of $CO_2$ and MgO (g/ mol), respectively.

The MgO conversion of the sorbent is defined as the percentage of the CC when compared to the $CC_{theoretical}$.

$$\mathrm{MgO_{conversion}} = \frac{CC}{CC_{theoretical} \times w_{MgO\_sorbent}} \times 100\ (\%) \tag{26}$$

Where $W_{MgO\_sorbent}$ represents the nominal mass fraction of the MgO (%, wt.) in the sorbent.

### 3.5.2 FIXED-BED UNIT

A lab-scale fixed-bed unit (Figure 8-5, section 8.1, appendix) was used to perform the cycling experiments for the assessment of both stability and $CO_2$ uptake of the most promising samples identified from the TGA experiments, that is, 15 (Na, Li, K)-MgO, 15 (Na, Li, K)-MgO-Ca and 15 (Na, Li, K)-MgO-Ce. These tests consisted of 10 sorption/ desorption cycles with sorption and desorption temperatures of 280 °C and 400 °C, respectively, and under two different atmospheres: first, to simulate the enhanced conditions, sorption under an atmosphere of 100 % of $CO_2$ followed by desorption under an atmosphere of 100 % of air; and second, to assess the applicability in the industry, sorption under an atmosphere of 25 % of $CO_2$ and 75 % of air followed by desorption under an atmosphere of 100 % of air.

### 3.5.2.1 FIXED-BED UNIT DESCRIPTION

The lab-scale fixed-bed unit consists of an oven with 10 cm diameter and 30 cm in height, whose interior is coated with ceramic to guarantee appropriate heat conduction to a high temperature resistant quartz reactor, measuring 5 cm of internal diameter and 14 cm of height. This reactor contains a porous plate on its interior, where the material to be tested was placed, and the sorption/ desorption temperatures are monitored by a thermocouple type K that is inside a thermowell nearby the sample, which is connected to a temperature controller designated Eurotherm® 2000 series.

The gases fed into the reactor were controlled by flowmeters from Alicat Scientific (MC Series), in the case of air flow, and from Brooks (5850E Series), in the case of $CO_2$. A total flow of 1000 ml/ min of $CO_2$ or 250 ml/ min of $CO_2$ balanced with 750 ml/ min of air was used during the sorption step, and the desorption was performed using a total flow of 1000 ml/ min of air in both cases. The Alicat Scientific mass flowmeter has a manufacturer calibration that was verified in the beginning of each experiment using a glass bubble flowmeter, and in case of the Brooks device it was necessary perform a calibration using the same glass bubble flowmeter.

The exhaust gas flow was connected to a $CO_2$ detector for measuring the concentration of $CO_2$ (%) in the outlet stream along the sorption and/ or desorption cycles. Since the $CO_2$ uptake quantification was performed during the desorption step, under an air atmosphere, it was used a Guardian NG $CO_2$ detector with a $CO_2$ concentration range of 0 – 30 % with +/- 2 % of full-scale accuracy. During the sorption step performed with 100% of $CO_2$, the $CO_2$ detector was disconnected to avoid the IR cell saturation, and the data were recorded only during desorption step.

The data acquisition of time elapsed, fixed-bed reactor temperature, oven temperature, $CO_2$ concentration in the outlet gas stream and air flow rate during the tests was made using LabVIEW software. This same software allowed the input of both oven temperature and air flow rate during the tests according to the defined experimental conditions.

### 3.5.2.2 EXPERIMENTAL PROCEDURE

To assess the $CO_2$ uptake in the fixed-bed, the following experimental procedure was implemented:

1. Weigh ~ 0.75 g, introduce and distribute uniformly the sorbent sample inside the silica plate of the reactor;
2. Introduce the reactor inside the oven and place the thermocouple inside the reactor thermowell;
3. Place the clamps on the top and at the bottom of the reactor to prevent gas leakage between it and the inlet and outlet flow gas tubes;
4. Open the air and the $CO_2$ valves (the pressure gauge is set to 2 bar);
5. Set the resulting calibration position into the Brooks and set the corresponding value of the air flow rate in the LABVIEW. The gas flow should be verified using the bubble flowmeter;
6. Open the exhaust gases valve and plug in the $CO_2$ detector;

7. Cover the top surface of the reactor with two ceramic plates and wrap it around with thermal insulation tape to avoid heat losses;
8. Turn on the oven and set the temperature to 280 °C in the LABVIEW;
9. Start to record the experiment in LABVIEW;
10. Carry out 10 sorption/ desorption cycles: sorption at 280 °C with 250 ml/min of $CO_2$ balanced with 750 ml/min of air or 1000 ml/ min of $CO_2$; and desorption performed with 1000 ml/ min of air at 400 °C. Each sorption step was carried out during 30 min, and the desorption time was monitored by the $CO_2$ detector, i.e., the desorption was concluded when the $CO_2$ detector display 0 % of $CO_2$, meaning that all the uptake $CO_2$ was released;
11. At the end of the experiment, stop and record the LabVIEW data acquisition software, turn off the oven, unplug the $CO_2$ detector, flowmeters, and valves;
12. Wait temperature falls and remove the oven reactor carefully using insulating gloves. Weigh and preserve the sorbent sample in a sealed recipient for XRD, $N_2$ sorption and SEM analysis.

### 3.5.2.3 ASSESSMENT OF $CO_2$ CAPTURE AND SORBENTS STABILITY DURING SORPTION/ DESORPTION CYCLES

The data file obtained at the end of the 10 sorption/ desorption cycles with the LabVIEW software was analyzed in a Microsoft Excel spreadsheet developed according to the calculation approach in a formerly published work [59].

After the sorption step, carried out with 25 % or 100 % of $CO_2$, the captured $CO_2$ was released and quantified in an atmosphere with 100 % of air. The molar amount of the $CO_2$ released during the desorption, $n_{CO2,\ desorption}$, was determined with the following equation (27):

$$\mathrm{n_{CO_2,desorption}} = \int_{t_1}^{t_2} \left(\mathrm{n_{CO_2,captured}}\right) \mathrm{dt} \tag{27}$$

Where $n_{CO2,\ captured}$ is the molar amount of $CO_2$ released by the sorbent between the start and end times of the desorption reaction $t_1$ and $t_2$, respectively.

Figure 3-6 illustrates an example of a $CO_2$ desorption profile during an experimental test in a fixed-bed reactor.

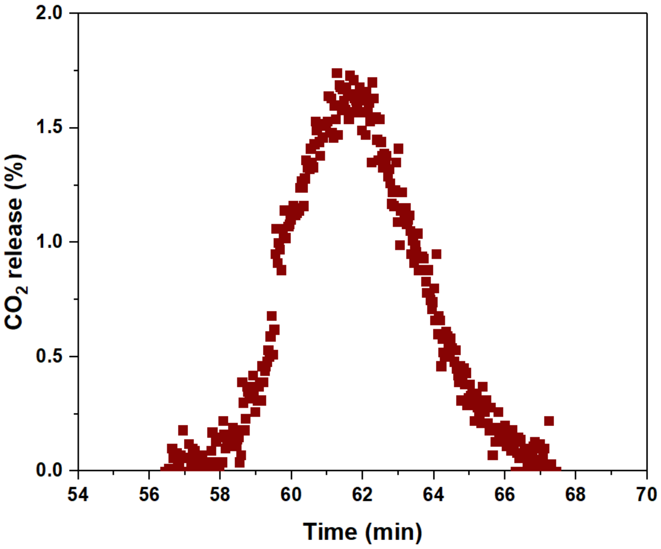

**Figure 3-6 – $CO_2$ desorption profile example during experimental tests carried out in the fixed-bed reactor.**

The MgO conversion (%) of the sorbent, i.e., conversion of MgO to $MgCO_3$ during the sorption step, was obtained using the following equation (28):

$$\mathrm{MgO}_{\mathrm{conversion}} = \frac{n_{CO_{2,desorption}} \times Mr_{MgO}}{m_{sorbent} \times w_{MgO\_sorbent}} \times 100\ (\%) \tag{28}$$

Where $n_{CO2,\ desorption}$ represents the molar amount of the $CO_2$ (mol) captured and released during the desorption step; $Mr_{MgO}$ represents the molar mass of MgO (g/ mol), $m_{sorbent}$ represents the mass of sorbent (g); and $w_{Mgo\text{-}sorbent}$ represents the nominal mass fraction of the MgO (%, wt.) in the sorbent.

# 4 RESULTS AND DISCUSSION

## 4.1 SORBENTS AND ALKALI SALTS CHARACTERIZATION

The textural, mineralogical, and morphological characterization of MgO-based sorbents was performed to assess the effect of support (Ca and Ce-based) and of alkali doping with $NaNO_3$ or (Na, Li, K)$NO_3$ salts in the sorbent's properties. In addition, the thermal decomposition of mono and ternary alkali salts was evaluated.

### 4.1.1 CHARACTERIZATION OF UNSUPPORTED AND SUPPORTED MAGNESIUM OXIDE BASED SORBENTS PROPERTIES

In order to assess the mineralogical, textural and morphological properties of the unsupported and supported MgO sorbents identified in Table 3-1 of section 3.1.1., these were characterized by XRD, $N_2$ sorption and SEM, respectively. For comparative reasons a commercial MgO was also analyzed.

Figure 4-1 shows the x-ray diffraction peaks and Figure 4-2 illustrates the MgO crystallite size assessed for all the unsupported and supported sorbents, as well as for the commercial MgO.

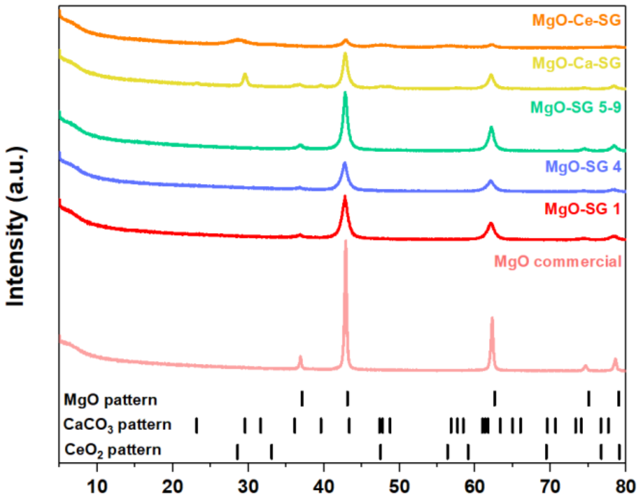

**Figure 4-1 – XRD patterns of the MgO commercial and of the synthesized MgO sorbents by sol-gel method: unsupported (MgO-SG 1, MgO-SG 4, MgO-SG 5-9) and supported (MgO-Ca-SG and MgO-Ce-SG).**

From the analysis of Figure 4-1 it is possible to observe that all the XRD patterns of the synthesized MgO sorbents exhibit the characteristic peaks of the MgO pattern (42.9 °, 62.2 °, 78.5 °), as expected. This evidence indicates that both the synthesis by sol-gel method and the calcination pre-treatment at 500 °C were well succeeded. In addition, XRD patterns of the supported MgO-Ca-SG and MgO-Ce-SG sorbents also present the characteristic peaks of the correspondent XRD pattern support at 29.5 ° and at 28.5 °, respectively, suggesting that the addition of porous support was successful. The difference between the XRD patterns of the synthesized sorbents and that of the MgO commercial resides in the intensity of the referred peaks and, thus, in the MgO crystallite size of each sorbent. The XRD pattern of the MgO commercial consists of very intense and sharper peaks, while XRD patterns of the MgO-SG 1, MgO-SG4, MgO-SG 5-9, MgO-Ca-SG and MgO-Ce-SG present less intense and broader peaks, meaning that the MgO commercial presents larger MgO crystallites than those of the synthesized MgO sorbents.

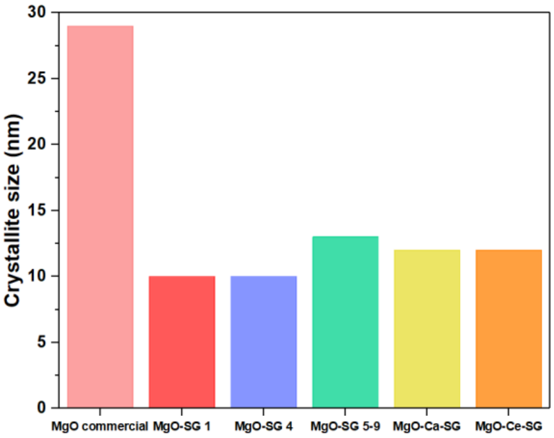

**Figure 4-2 – MgO crystallite size of the MgO commercial and of the synthesized sorbents: unsupported (MgO-SG 1, MgO-SG 4 and MgO-SG 5-9), supported (MgO-Ca-SG and MgO-Ce-SG).**

It is possible to observe in Figure 4-2 that the commercial MgO crystallites are larger than the crystallites of any of the synthesized sorbents, which is in line with the expected. Quantitatively, both MgO-SG 1 and MgO-SG 4 are the sorbents that present smaller MgO crystallites with a size of 10 nm, that is, three times smaller than that of the MgO crystallites of the commercial MgO. The MgO-SG 5-9, MgO-Ca-SG and MgO-Ce-SG samples also exhibit MgO crystallites smaller than those of the commercial MgO, with a size of 13, 12 and 12 nm, respectively. Thus, it is possible to conclude that the decision of using the sol-gel method to synthesize MgO sorbents was advantageous, since it allowed to obtain MgO sorbents with lower sized particles that, in turn, are directly correlated with higher surface areas, enhancing the $CO_2$ sorption [12]. The size of MgO crystallites described in literature can vary a lot, and it can be correlated with the synthetization method. Thus, average crystallites size of 7 – 8 nm of a MgO sorbent can be obtained through the calcination of pure hydromagnesite (HM) [25], but values around to 100 nm are also described, for example, when sol-gel method is applied using different gelling agents and calcination temperatures [60].

The $N_2$ sorption technique was used to assess the textural properties of the synthetized MgO sorbents (unsupported and supported with Ca and Ce) and of the commercial MgO. Figure 4-3 shows the $N_2$ sorption isotherms, Figure 4-4 the specific surface area ($S_{BET}$) and total pore volume ($V_p$), and Figure 4-5 the pore size distribution (PSD) estimated by the BJH desorption of all sorbents.

The $N_2$ sorption-desorption isotherms (Figure 4-3) of the MgO-SG 1, MgO-SG 4, MgO-SG 5-9 and MgO-Ce-SG sorbents resemble to type IV (Figure 3-4), accordingly to IUPAC's classification [57]. The hysteresis loop of the MgO-SG 1, MgO-SG 4 and MgO-Ce-SG sorbents is classified as type H4 (Figure 3-5), which is typical of mesoporous materials. The hysteresis loop of the MgO-SG 5-9 is classified as type H3 that is often associated with macroporous materials. The $N_2$ sorption-desorption isotherms of the commercial MgO and MgO-Ca-SG are classified as type II, that are features of macroporous materials.

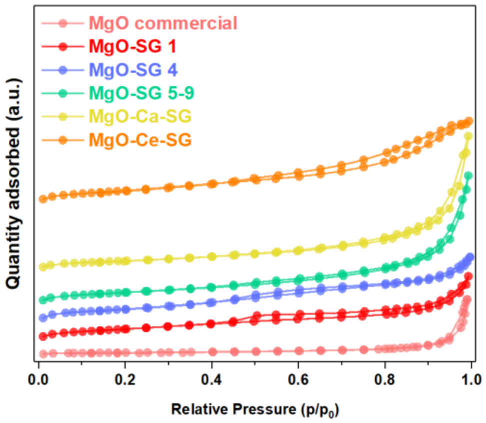

**Figure 4-3 – $N_2$ sorption isotherms of the MgO commercial and of the unsupported sorbents (MgO-SG 1, MgO-SG 4 and MgO-SG 5-9), supported sorbents (MgO-Ca-SG and MgO-Ce-SG).**

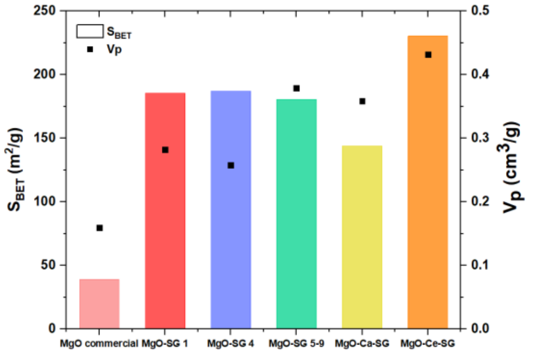

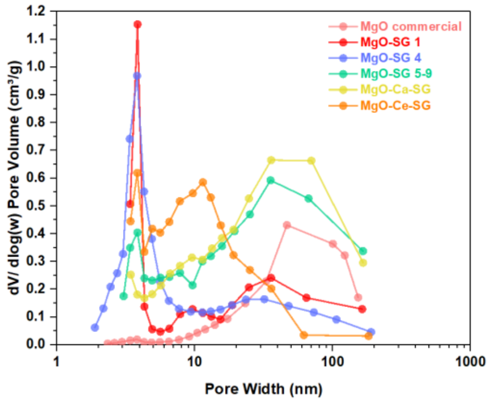

**Figure 4-4 – Specific Surface Area ($S_{BET}$) and total pore volume ($V_p$) of the MgO commercial and of the unsupported sorbents (MgO-SG 1, MgO-SG 4 and MgO-SG 5-9), supported sorbents (MgO-Ca-SG and MgO-Ce-SG).**

**Figure 4-5 – Pore size distribution (PSD) estimated by the BJH desorption of the MgO commercial and of the unsupported sorbents (MgO-SG 1, MgO-SG 4 and MgO-SG 5-9), supported sorbents (MgO-Ca-SG and MgO-Ce-SG).**

The commercial MgO exhibits the lowest $S_{BET}$ of 39 $m^2$/ g among the analyzed set (Figure 4-4), which is in line with its largest MgO crystallite size obtained by XRD. The MgO-SG-Ce is associated with the highest $S_{BET}$ (230 $m^2$/ g) that is ~6 times higher than that of the MgO commercial; followed by MgO-SG 4 (187 $m^2$/ g), MgO-SG 1 (185 $m^2$/ g) and MgO-SG 5-9 (180 $m^2$/ g), with those three sorbents presenting very identical values of $S_{BET}$, accordingly with the also very similar MgO crystallite sizes; and, finally, by MgO-Ca-SG (144 $m^2$/ g). Moreover, the synthesized sorbents exhibit higher total pore volume than the MgO commercial, which is expected to facilitate the $CO_2$ sorption process, as the resistance through diffusion diminishes inside of the pores as its volume expands [10].

The PSD (Figure 4-5) of the MgO-SG 1, MgO-SG 4 and MgO-Ce-SG sorbents indicates the presence of mainly mesoporous (2 – 50 nm), which is in line with the evidence provided by the correspondent $N_2$ isotherms' characterizations. There is also a small percentage of macroporous (> 50 nm). Both the commercial MgO and MgO-SG-Ca consist of macroporous predominantly, although the MgO-SG-Ca also exhibits a small share of mesoporous. The PSD of the MgO-SG 5-9 sorbent reveals the existence of both meso and macroporous.

The textural properties show that the range of temperatures used during the sol-gel synthesis, i.e., 60 °C or 80 °C, did not affect the $S_{BET}$ since the values are very similar (Figure 4-4), so for practical reasons the supported sorbents were prepared at 80 °C. As mentioned above, the properties of synthesized MgO can vary considerably, in literature, using sol-gel method $S_{BET}$ values of 66 $m^2$/ g [61] and 191 $m^2$/ g [62] can be found, which is in line with the present study. By aerogel method, the $S_{BET}$ can reach 569 $m^2$/g [63], but it will also increase the manufacturing costs, as it uses a high-pressure autoclave and organics during the synthesis, that, in turn, also impacts negatively the environment.

The synthesized MgO-Ca-SG presents higher $S_{BET}$ (144 $m^2$/ g) and lower crystallite size (12 nm) than the MgO-10Ca reported by Jin et al., namely, 35 $m^2$/ g and 21 nm [64]. The synthesized MgO-Ce-SG presents similar $S_{BET}$ (230 $m^2$/ g) than the MgO-10Ce described by Jin et al., namely, 252 $m^2$/g [36].

Regarding to supported sorbents, the particles size and the homogeneity distribution of the Mg, Ca and Ce compounds in the sorbent is a relevant parameter than can influence the sorbent reactivity and stability along the sorption/ desorption cycles. Figure 4-6 shows the SEM images of unsupported sorbent (MgO-SG 5-9) and supported sorbents (MgO-Ca-SG and MgO-Ce-SG), and Figure 4-7 shows the elements mapping of supported sorbents.

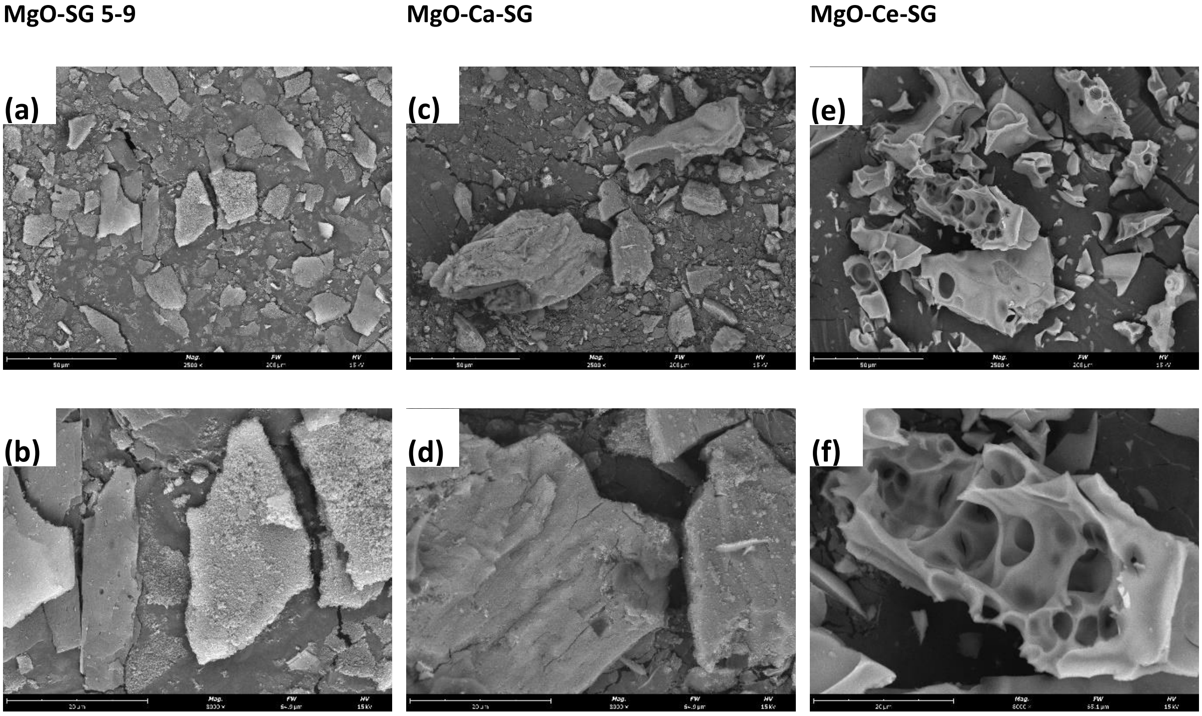

**Figure 4-6 – SEM images of (a and b) MgO-SG 5-9, (c and d) MgO-Ca-SG and (e and f) MgO-Ce-SG (a, c, e: scale: 50_µm and magnification: x 2 500; b, d, f: scale: 20_µm and magnification: x 8 000).**

The comparison of SEM images (a) and (b) with (c) and (d) from Figure 4-6 indicates that the addition of support did not change the overall sheet-like morphology of the MgO sorbent, that appeared to maintain a compact and smooth surface after the addition of the Ca support. Conversely, the differences are notable from

SEM images (a) and (b) to (e) and (f), respectively. The addition of a Ce support led to the formation of an internal structure consisting of numerous spherical empty holes of different diameters, in accordance with the mesoporous nature of the MgO-SG-Ce sorbent concluded from the $N_2$ sorption characterization.

**(a) MgO-Ca-SG** **(e) MgO-Ce-SG**

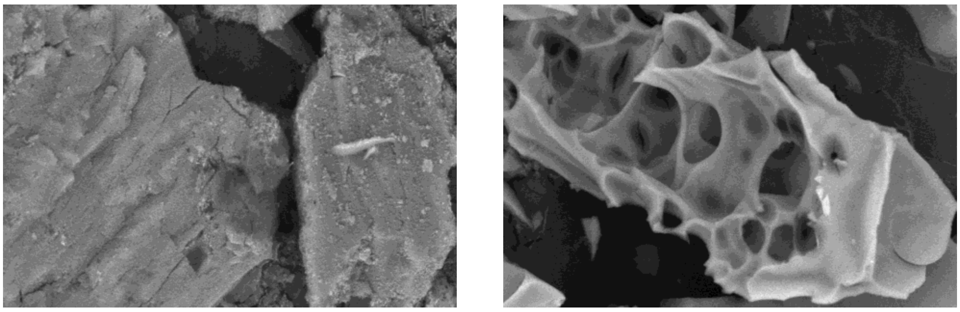

**(b) Magnesium** **(f) Magnesium**

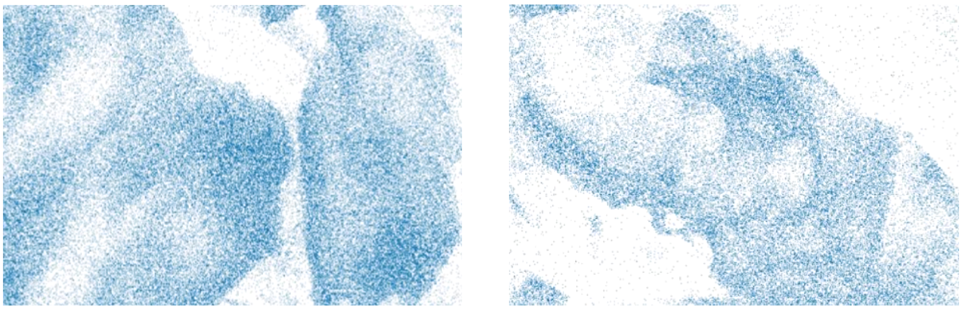

**(c) Calcium** **(g) Cerium**

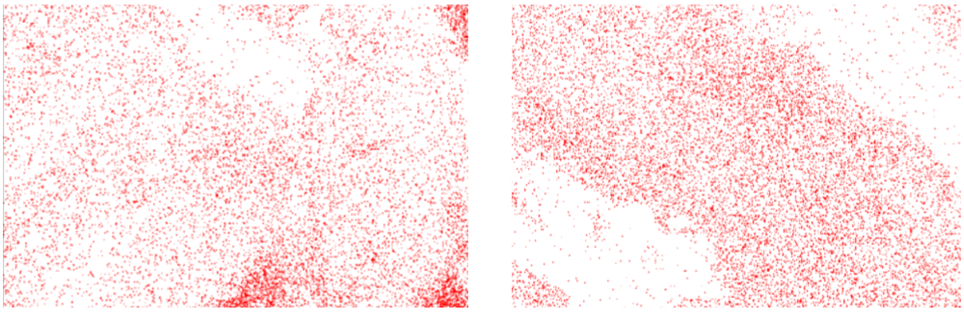

**(d) Oxigen** **(h) Oxigen**

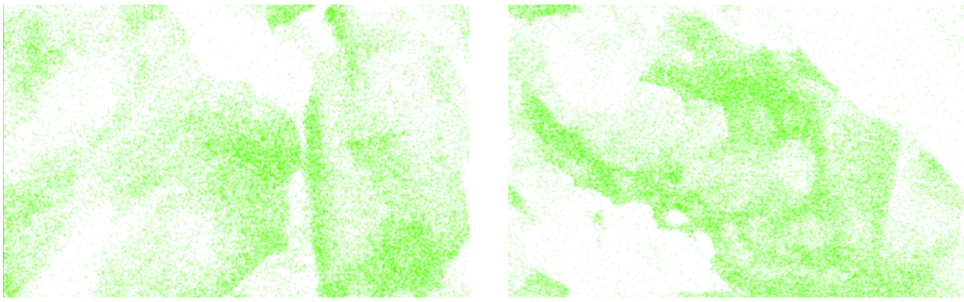

**Figure 4-7 – Mapping of SEM images of (a, b, c, and d) MgO-Ca-SG, and (e, f, g and h) MgO-Ce-SG (scale: 20_µm and magnification: x 8 000).**

The mapping of the elements Mg, O and correspondent support, Ca or Ce, indicates that both supports are well dispersed on the MgO surface, meaning that the sol-gel method allowed to generate an homogeneous supported sorbent, as expected [10,36]. The identified whiter areas, especially for the Mg and O elements, is related with the morphology (existence of holes) of the particles as can be observed in image (a) and (b).

### 4.1.2 ASSESSMENT OF MAGNESIUM OXIDE BASED SORBENTS PROPERTIES AFTER DOPING WITH ALKALI METAL SALTS

As mentioned in literature review, the MgO-based sorbents doping with alkali metal salts (AMS) is a promising approach to improve their $CO_2$ uptake and cyclic stability. The first part of this thesis is a preliminary study of different sorbent materials, which were tested in two different equipment, namely, a TGA and a fixed--bed reactor unit. For the sorbents tested in the TGA equipment, only the mineralogical and crystallite size was done by XRD; but for the sorbents tested in the fixed-bed unit reactor, where a higher amount of sample was available, $N_2$ sorption and SEM were also done.

Summarizing:

i. the 30 Na-MgO (prepared with MgO-SG 1) was characterized by XRD to confirm the impregnation of $NaNO_3$ in the sorbent sample and to assess the effect of the doping procedure in the crystallite size;

ii. the sorbents doped with mono alkali salts (15 Na-MgO, 25 Na-MgO, 35 Na-MgO) and ternary alkali salts (15 (Na, K, Li)-MgO, 25 (Na, K, Li)-MgO, 35 (Na, K, Li)-MgO), prepared with MgO-SG 4, were characterized by XRD to confirm the presence of AMS in sorbent and to assess the effect of the doping procedure in the crystallite size;

iii. the unsupported (MgO-SG 5-9) and supported sorbents (MgO-Ca-SG and MgO-Ce-SG) were tested in the fixed-bed reactor and were characterized by XRD, $N_2$ sorption and SEM.

Figure 4-8 illustrates the XRD patterns of the fresh MgO-SG 1, MgO-SG 1 after impregnation with 30 % of $NaNO_3$ and calcined at 450 °C (30 Na-MgO), and 30 Na-MgO after the 1st cycle and, finally, after the 2nd sorption.

The impregnated sample, i.e., 30 Na-MgO exhibits the characteristic peaks of the MgO pattern (42.9°, 62.2°, 78.5°), and the main peaks of the $NaNO_3$ pattern (29.4°, 31.9°, 38.9°, 47.9°), suggesting that the impregnation method was well-succeeded. After the 1st sorption-desorption cycle, carried out in the TGA at 300 °C and 430 °C, respectively, and under an atmosphere of 100 % of $CO_2$, both MgO and $NaNO_3$ remained present. As expectable, the $CO_2$ sorption by the 30 Na-MgO sorbent was confirmed by the presence of an $MgCO_3$ peak (32.6 °), after the 2nd sorption step. Nevertheless, the presence of MgO peaks show that not all the MgO was converted to $MgCO_3$.

The effect of the AMS doping in the crystallite size of MgO (Figure 4-9) was assessed using the Scherrer equation (22), as described in section 3.2.2. Considering the crystallite size of MgO-SG 1 as reference, it can be affirmed that the crystalite size of MgO increased about 78 % after $NaNO_3$ impregnation, and 197 % and 212 % after the 1st cycle and 2nd sorption, respectively. Therefore, the AMS doping contributed to the crystallite size's increase, meaning that the alkali metal nitrates accelerate the crystal growth of MgO. Yet, it suggests that a reduced surface area of MgO should be available to react with the $CO_2$. However, this limitation is overpassed by the molten properties of $NaNO_3$ that facilitate the $CO_2$ difusion until the MgO surface [27]. The crystalite size increase was potenciated by the sorption/ desorption cycles, probably due to the higher temperatures used during the regeneration step. Dal Pozzo reported MgO crystallites with the average size of 20 nm for a MgO sorbent promoted with 10 % of $NaNO_3$ after being calcined at 450 °C [25]. The 30 Na-MgO sorbent at the same conditions obtained smaller MgO crystallites (17 nm).

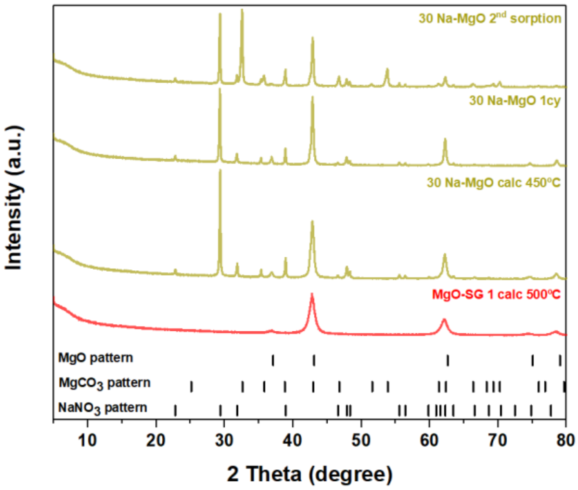

**Figure 4-8 – XRD patterns of the fresh sorbent MgO-SG 1 and of the impregnated samples 30 Na-SG after being calcined at 450 °C, after 1 cycle of sorption-desorption at 300 °C and 430°C, respectively, and after 2nd sorption at 300 °C.**

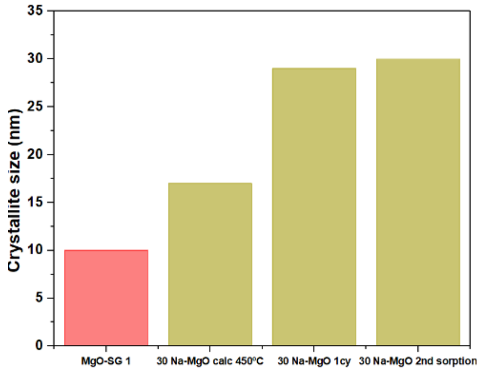

**Figure 4-9 – MgO crystallite size of the fresh sorbent MgO-SG 1 and of the impregnated sample 30 Na-MgO after being calcined at 450 °C, after 1 cycle of sorption-desorption at 300 °C and 430°C, respectively, and 30 Na-MgO sorbent after the 2nd sorption at 300 °C**

The crystalline structures of the MgO-SG 4 sorbent impregnated with 15, 25 and 35 % of either $NaNO_3$ or ternary mixture of $KNO_3$, $NaNO_3$ and $LiNO_3$ were analyzed by powder XRD. Figure 4-10 and Figure 4-11 show XRD patterns of fresh MgO-SG4 sorbent impregnated with 15, 25 and 35 % of either $NaNO_3$ or ternary mixture of $KNO_3$, $NaNO_3$ and $LiNO_3$, respectively.

Considering both Figure 4-10 and Figure 4-11, there are some first general evidences in common possible to describe. In what regards to the mono AMS impregnated samples, all the XRD obtained patterns show the characteristic peaks of the MgO pattern and a main peak located at ~ 29.4 ° that is referred to the $NaNO_3$ pattern. For the sorbents impregnated with the ternary alkali metals salts, the main peak of $KNO_3$ (~23.6°) was also observed, and the second main peak should be overlaid by the $NaNO_3$ peak (29.4°). The $LiNO_3$ was not identified, which can be justified by its high dispersion on the sorbent sample, which leads to the Li concentration below the instrumental detection limit [65], or its partial decomposition to $Li_2O_2$ or $LiO_2$ whose main peaks are around 32.9 ° and 33.5 °. Wang et al. study a similar ternary system, $LiNO_3$ (25.9 wt.%), $NaNO_3$ (20.06 wt.%) and $KNO_3$ (54.1 wt.%), and conclude that, unlike the sodium and potassium nitrate phases, lithium nitrate is an unstable phase in the ternary system that starts to decompose to $Li_2O_2$ and $LiO_2$ at temperatures higher than 440 °C [66].

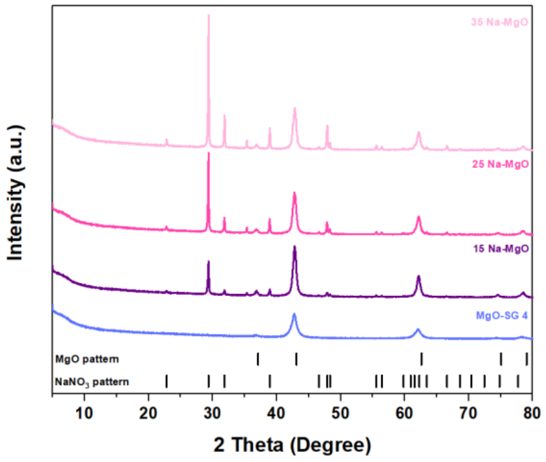

**Figure 4-10 – XRD patterns of the fresh sorbent MgO-SG 4 and of the fresh samples 15 Na-MgO, 25 Na-MgO and 35 Na-MgO.**

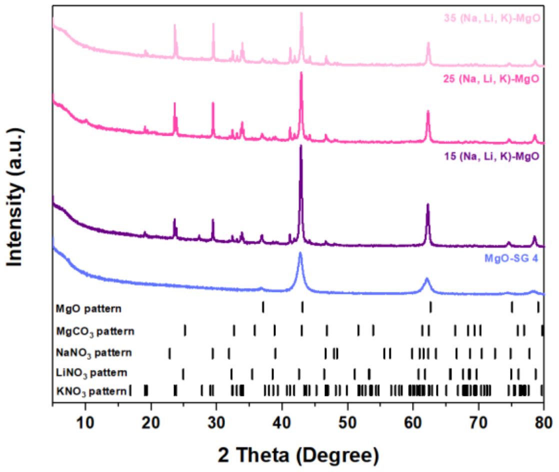

**Figure 4-11 – XRD patterns of the fresh sorbent MgO-SG 4 and of the fresh samples 15 (Na, Li, K)-MgO, 25 (Na, Li, K)-MgO and 35 (Na, Li, K)-MgO.**

Furthermore, the MgO peaks are significantly sharper in the impregnated samples, suggesting that the impregnation does influence the average size of MgO crystallite, as it occurred for the 30 Na-MgO sorbent. For example, the average crystallite size of the MgO-SG 4 sample is 10 nm, while the MgO-SG 4 impregnated with 15 % of $NaNO_3$ presents a crystallite with 15 nm, and the MgO-SG 4 impregnated with 15 % of (Na, Li, K)$NO_3$ achieves a crystallite size of 26 nm. Such results indicate that the impregnation with alkali metal nitrates increases the growth of the MgO crystals, that is accentuated in the case of the impregnation with the ternary mixture. Conversely, the AMS molar percentage of the impregnation doesn't appear to influence the increasing of the MgO crystallite. The MgO-SG4 samples doped with $NaNO_3$ present all an average crystallite size of ~ 15 nm and the MgO-SG4 samples doped with (Na, Li, K)$NO_3$ of ~ 27 nm, regardless the molar percentage of AMS impregnation (Table 4-1).

**Table 4-1 – Crystallite size of MgO-SG4 before and after doping with different molar percentages of AMS.**

| Crystallite size (nm) | 0 % (mol) | 15 % (mol) | 25 % (mol) | 35 % (mol) |
|---|---|---|---|---|
| **$NaNO_3$** | 10 | 15 | 15 | 16 |
| **(Na, Li, K) $NO_3$** | | 26 | 28 | 29 |

It is stated in literature the average crystallite size of a MgO sorbent obtained through the calcination of pure HM promoted with 10 % of $NaNO_3$ after calcination of 20 nm [25]. The same experience registers the same average crystallite size for a MgO sorbent obtained through the calcination of pure HM promoted with 10 % of the ternary mixture of 52 wt.% $KNO_3$, 18 wt.% $NaNO_3$ and 30 wt.% $LiNO_3$ after calcination [25]. The present work obtained average crystallite sizes of 15 and 26 nm for the fresh MgO-SG 4 sorbents doped with 15 % of $NaNO_3$ and with 15 % of the ternary mixture (Na, Li, K)$NO_3$, respectively.

The unsupported (MgO-SG 5-9) and supported sorbents (MgO-Ca-SG and MgO-Ce-SG) were doped with 15% of a ternary mixture of (Na, Li, K)$NO_3$. Figure 4-12 shows the x-ray diffraction peaks and Table 4-2 shows the

MgO crystallite size assessed for the unsupported and supported sorbents, i.e., 15 (Na, K, Li)-MgO, 15 (Na, K, Li)-MgO-Ca and 15 (Na, K, Li)-MgO-Ce, before and after the AMS doping.

The XRD patterns of the impregnated samples 15 (Na, Li, K)-MgO, 15 (Na, Li, K)-MgO-Ca and 15 (Na, Li, K)-MgO-Ce exhibit the characteristic peaks of the MgO pattern (42.9 °, 62.2 °, 78.5 °). The XRD patterns of the 15 (Na, Li, K)-MgO-Ca and 15 (Na, Li, K)-MgO-Ce also present the main peaks of the XRD pattern of $CaCO_3$ (29.4 °) and of the $CeO_2$ (28.5 °), respectively. Regarding to the nitrate salts used in the impregnation, $LiNO_3$ was not detected by XRD in any of the patterns of the analyzed sorbents, as expected. In fact, it is stated in literature that Li has a small crystallite size and, thus, a good dispersion in the sorbent [35]. The main peak of the $KNO_3$ pattern (23.5 °) was identified in the XRD patterns of the 15 (Na, Li, K)-MgO and of the 15 (Na, Li, K)-MgO-Ca, but its second main peak should be overlaid by the $NaNO_3$ peak (29.4 °). The remain peaks of the $NaNO_3$ pattern (31.9°, 38.9°, 47.9°) are also present. The characteristic peak of the $CeO_2$ is very wide, so it makes impossible to identify the peak at 29.4 ° of the $KNO_3$ and $NaNO_3$ patterns. Yet, a small peak at 27 ° of the $KNO_3$ pattern is exhibited, as well as the peaks at 31.9°, 38.9°, 47.9° related to the $NaNO_3$ pattern.

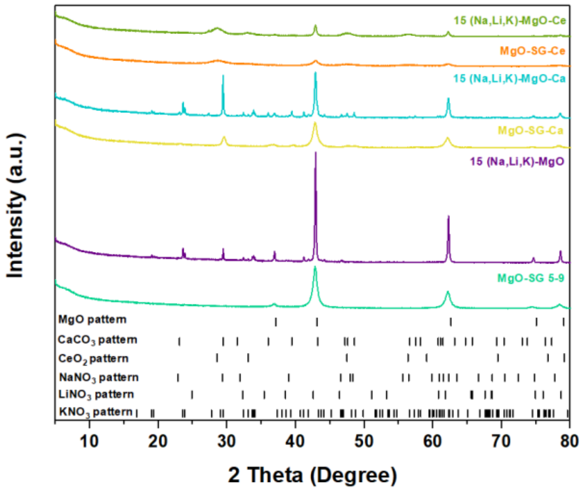

**Figure 4-12 – XRD patterns of the unsupported sample 15 (Na, Li, K)-MgO and of the supported samples 15 (Na, Li, K)-MgO-Ca and 15 (Na, Li, K)-MgO-Ce.**

From Table 4-2 it is possible to observe that the AMS doping affected the crystallite size of the unsupported and supported sorbents, provoking its increase. These results are in line with the AMS doping influence on the MgO crystallite size that was previously verified for the impregnated samples of both MgO-SG 1 and MgO-SG 4 sorbents.

**Table 4-2 – Crystallite size of unsupported (MgO-SG 5-9) and supported sorbents (MgO-Ca-SG and MgO-Ce-SG) before and after doping with 15% of ternary mixture of (Na, Li, K)$NO_3$.**

| Crystallite size (nm) | MgO-SG 5-9 | MgO-Ca-SG | MgO-Ce-SG |
|---|---|---|---|
| **0 % (wt.)** | 13 | 12 | 12 |
| **15 % (Na, Li, K)$NO_3$** | 26 * | 30 | 27 |

*From Table 4-1

The $N_2$ sorption technique was used to assess the textural properties of the unsupported MgO-SG 5-9 as well as of both the supported MgO-Ca-SG and MgO-Ce-SG sorbents after being impregnated with 15 % of (Na, Li, K)$NO_3$. Figure 4-13 shows the $N_2$ sorption isotherms, Figure 4-14 the specific surface area ($S_{BET}$) and total pore volume ($V_p$), and Figure 4-15 the pore size distribution (PSD) estimated by the BJH desorption of the 15 (Na, Li, K)-MgO, 15 (Na, Li, K)-MgO-Ca and 15 (Na, Li, K)-MgO-Ce, respectively.

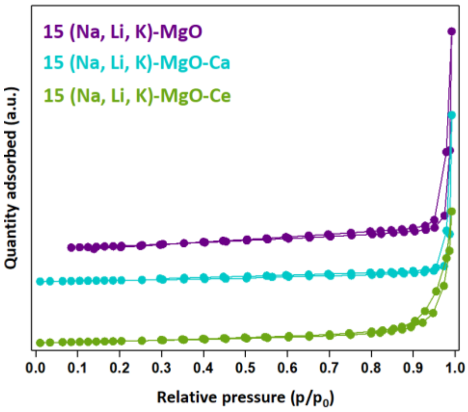

**Figure 4-13 – $N_2$ sorption isotherms of the MgO-SG 5-9, MgO-Ca-SG and MgO-Ce-SG after impregnation with 15 % of (Na, Li, K)$NO_3$.**

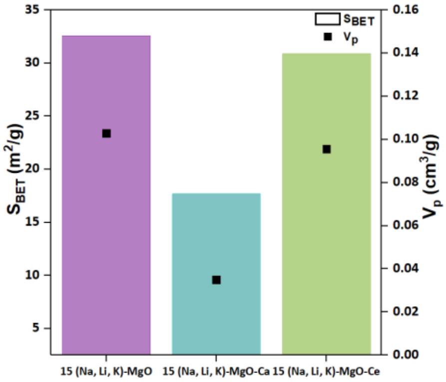

**Figure 4-14 – Specific Surface Area ($S_{BET}$) and total pore volume ($V_p$) of the MgO-SG 5-9, MgO-Ca-SG and MgO-Ce-SG after impregnation with 15 % of (Na, Li, K)$NO_3$.**

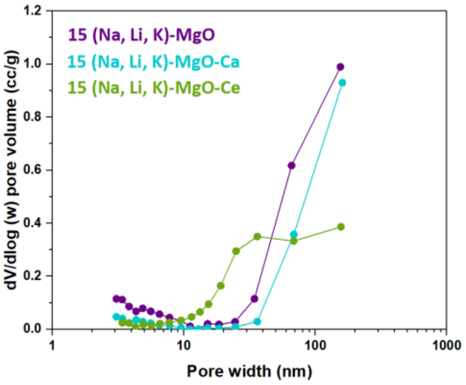

**Figure 4-15 – Pore size distribution (PSD) estimated by the BJH desorption of the MgO-SG 5-9, MgO-Ca-SG and MgO-Ce-SG after impregnation with 15 % of (Na, Li, K)$NO_3$.**

The $N_2$ sorption-desorption isotherms of 15 (Na, Li, K)-MgO, 15 (Na, Li, K)-MgO-Ca and 15 (Na, Li, K)-MgO-Ce sorbents conform to type II, accordingly to IUPAC's classification, characteristic of macroporous materials. As expected, the AMS doping seems to have affected MgO-SG 5-9 and the MgO-Ce-SG, both prior classified as type IV isotherms, for presenting a more pronounced hysteresis as fresh sorbents. Yet, the three analyzed sorbents present a very discreet hysteresis.

The 15 (Na, Li, K)-MgO sorbent presents the highest $S_{BET}$ (32 $m^2$/ g) that is very similar to that of the 15 (Na, Li, K)-MgO-Ce (31 $m^2$/ g). The 15 (Na, Li, K)-MgO-Ca exhibits the smallest $S_{BET}$ (18 $m^2$/ g). Moreover, all the sorbents analyzed in this set verified a reduction in their $S_{BET}$ with respect to before the impregnation (Figure 4-4). This evidence is in line with the previous conclusions from the XRD characterization, in which it was detected an increase of the MgO crystallite size, indicating a reduced surface area available for the MgO sorbent to uptake $CO_2$. Dal Pozzo et al. reported a $S_{BET}$ of 22 $m^2$/ g for a MgO sorbent promoted with 10 % of (Na, Li, K)$NO_3$ [25], which is smaller than that of 15 (Na, Li, K)-MgO and 15 (Na, Li, K)-MgO-Ce sorbents, but higher than that of 15 (Na, Li, K)-MgO-Ca. In addition, all the analyzed sorbents of the set also registered a decrease of the total pore volume after AMS doping, due to its partial occupation by the ternary mixture [31], which should affect the $CO_2$ sorption due to the higher occurrence of pores' blocking.

The PSD of the 15 (Na, Li, K)-MgO, 15 (Na, Li, K)-MgO-Ca and 15 (Na, Li, K)-MgO-Ce sorbents indicates a constitution of mainly macropores (> 50 nm), as expected according to the detected AMS impact on the type of isotherms. A small share of mesoporous is also present though, especially in the case of 15 (Na, Li, K)-MgO-Ce.

To evaluate the sorbents 3D morphology, the distribution of the porous support (Ca and Ce-based) and of the AMS along the particles it was carried the SEM analysis. Figure 4-16 shows the SEM image of 15 (Na, Li, K)-MgO, 15 (Na, Li, K)-MgO-Ca and 15 (Na, Li, K)-MgO-Ce sorbents and Figure 4-17 shows the identification of the main elements present in specific zones of 15 (Na, Li, K)-MgO, acquired by energy dispersive x-ray spectrometer (EDS).

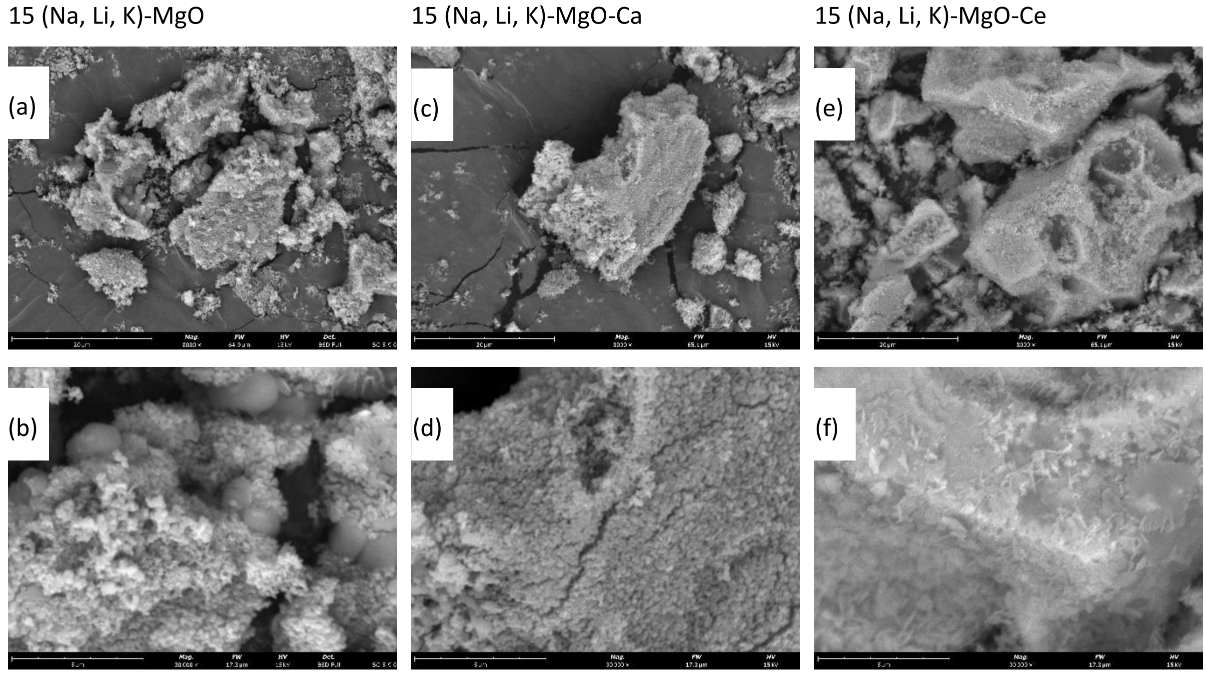

**Figure 4-16 – SEM images of (a and b) 15 (Na, Li, K)-MgO, (c and d) 15 (Na, Li, K)-MgO-Ca and (e and f) 15 (Na, Li, K)-MgO-Ce sorbents (a, c, e: scale: 20_µm and magnification: x 8 000; b, d, f: scale: 5_µm and magnification: x 30 000).**

The SEM images of the unsupported 15 (Na, Li, K)-MgO reveal the presence of several "spherical" structures with smooth surface that are not present in the SEM images of both the supported 15 (Na, Li, K)-MgO-Ca and 15 (Na, Li, K)-MgO-Ce sorbents. These structures are associated with the sintering phenomenon that results from the melting of some species (further identified by EDS). Thus, evidence suggests that the addition of supports to MgO-based sorbents prevents the sintering to occur and, in turn, the agglomeration of MgO particles by melting content [63]. Instead, it provides the well dispersion of it, which should improve the $CO_2$ sorption process. In addition, the surface of the 15 (Na, Li, K)-MgO-Ce sorbent exhibits some crystal structures, which seem haphazardly overlapping sheets.

Figure 4-17 shows the comparison of the EDS obtained for a sintered (blue rectangle) and for a non-sintered zone (red rectangle) of 15 (Na, Li, K) MgO sorbent. The sintered zone is mainly constituted by K instead of Mg, conversely to what is verified for the non-sintered zone's constitution. Hence, EDS indicates that the sintering of the unsupported MgO sorbent corresponds to the melting of $KNO_3$. In fact, the melting point of $KNO_3$ (334 °C [63]) was surpassed by the calcination pre-treatment temperature of 450 °C.

15 (Na, Li, K) MgO (a) Blue rectangule (b) Red rectangule

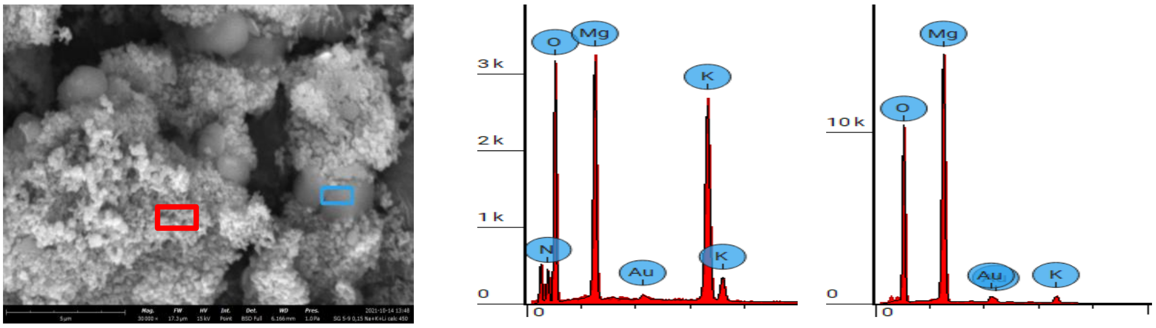

**Figure 4-17 – SEM image of 15 (Na, Li, K) MgO sorbent and identification of main elements acquired by energy dispersive x-ray spectrometer (qualitative analysis).**

Figure 4-18 shows the mapping of the following sorbents: 15 (Na, Li, K)-MgO, 15 (Na, Li, K)-MgO-Ca and 15 (Na, Li, K)-MgO-Ce, that allows to assess the elements distributions in the sorbents.

It was not possible to mapping the Li distribution on the sorbents because the X-ray signal generated for this element, as well as for H and He, is low and the probability of absorption is high. Therefore, its emitted intensity is small [67,68]. About potassium and calcium, the used equipment did not allow to select their identification lines and, since there is an overlap between the $C_{K\alpha}$ line, and $Ca_L$ and $K_L$ lines, it was observed an intensification of the signal due to the carbon strip where the sample of the sorbent is deposited. Therefore, the evaluation of the elements mapping should be focused only over the particles surface.

Calcium and cerium appear to be well-distributed along the MgO particles. No segregation was observed. In supported particles, the potassium and sodium distribution along the surface looks to be homogeneous. However, for the unsupported sorbent, an intense signal is observed over the particle (black circles) in case of sodium and potassium, that can be justified by the occurrence of some sintering associated to the $NaNO_3$ and $KNO_3$, as already mentioned. In fact, it was not detectable in the 15 (Na, Li, K)-MgO-Ca sample, and its signal is very smooth for the 15 (Na, Li, K)-MgO-Ce sorbent, which can be related with the higher dispersion of Na in supported samples that, in turn, reduces the emitted intensity. The achieved results are very interesting since they allow to confirm that the support had a relevant role in the AMS dispersion along the sorbent which certainly can be related with the sorbents performance along the sorption-desorption cycles.

(a)15 (Na, Li, K) MgO (e) 15 (Na, Li, K) MgO-Ca (i) 15 (Na, Li, K) MgO-Ce

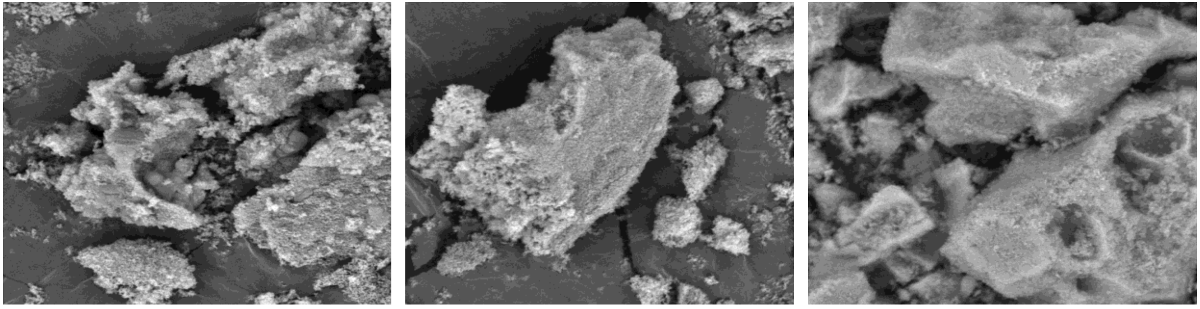

(a) Magnesium (f) Magnesium (j) Magnesium

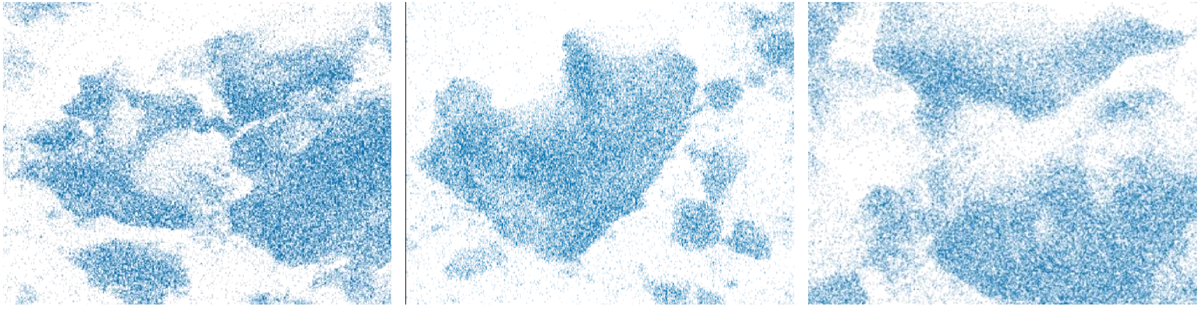

Unsupported sorbent

(g) Calcium (l) Cerium

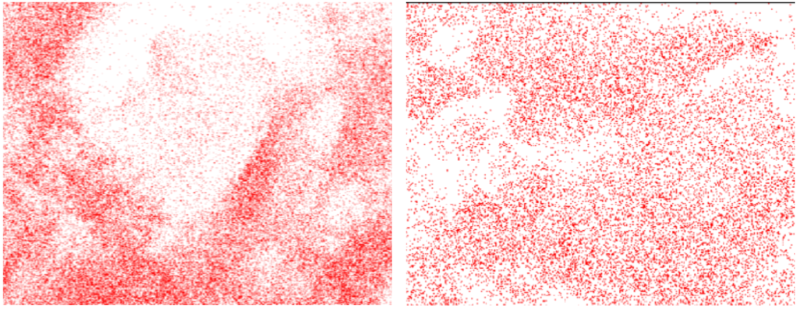

(b) Potassium (h) Potassium (m) Potassium

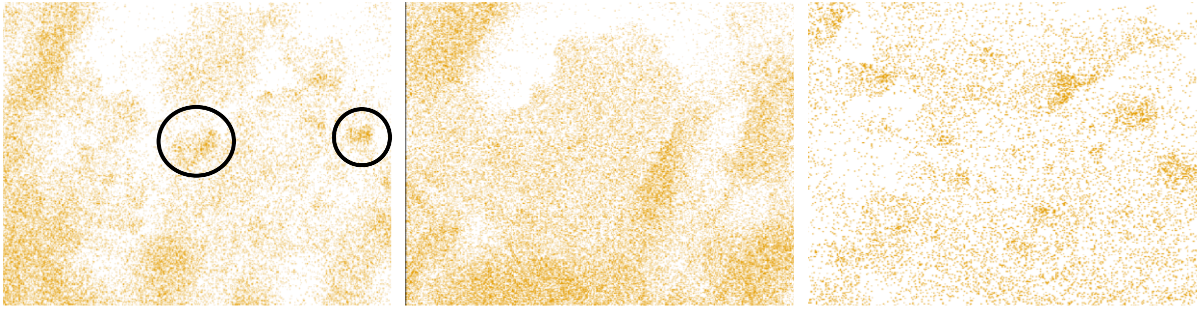

(c) Sodium

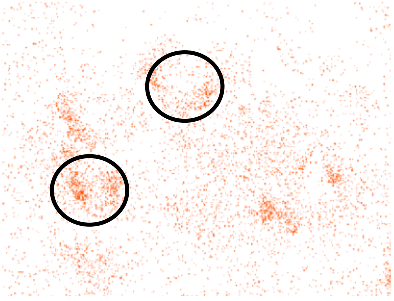

No detected

(n) Sodium

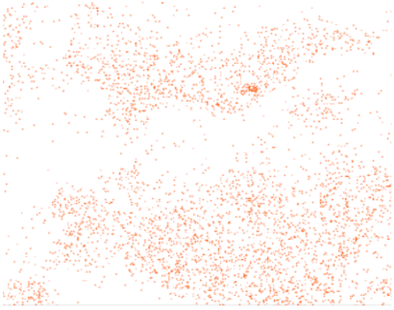

**Figure 4-18 – Mapping of SEM images: (a, b, c, d) 15(Na, Li, K)-MgO; (e, f, g , h) 15 (Na, Li, K) MgO-Ca, and (i, j, l, m, n) 15 (Na, Li, K)-MgO-Ce (scale: 20_µm and magnification: x 8 000).**

### 4.1.3 THERMAL DECOMPOSITION OF MONO AND TERNARY ALKALI NITRATE SALTS

The mass loss (%) and the first derivative of mass change (DTG) profiles with increasing temperature were obtained in the TGA , between 25 °C and 1000 °C (heating rate: 10 °C/ min) under 100 % of air or 100 % of $CO_2$ flow, for pure $NaNO_3$ and ternary mixture of 52 wt.% $KNO_3$, 18 wt. % $NaNO_3$ and 30 wt.% $LiNO_3$, (Figure 4-19 and Figure 4-20, respectively). The heat flow profile and respective 1st derivative of these alkali nitrate salts are represented in Figure 4-21 and Figure 4-22, respectively.

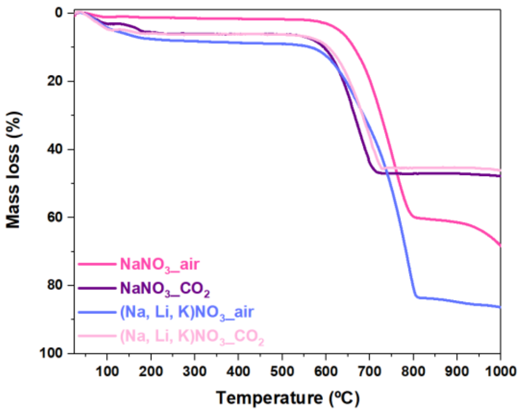

**Figure 4-19 – Thermal decomposition in massa loss (%) of $NaNO_3$ and (Na ,Li , K)$NO_3$ with temperature.**

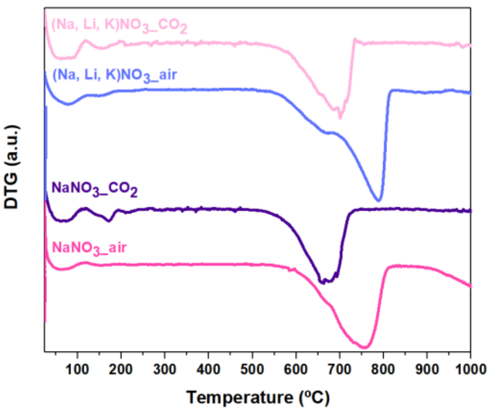

**Figure 4-20 – First derivative of mass change of $NaNO_3$ and (Na,Li, K)$NO_3$ with temperature.**

A preliminary analysis of Figure 4-19 shows a mass loss until 200 °C related with the water, since these salts are very hygroscopic [46]. Stands out that all the samples remain almost stable up to a temperature of around 600 °C, where an abrupt loss of mass is verified, regardless the atmosphere. On the contrary, the type of atmosphere does affect the extent of the decomposition: under pure air atmosphere, higher decomposition temperatures (~800 °C) are achieved when compared to those related to the 100 % $CO_2$ atmosphere (~715 °C). In addition, the samples tested in the presence of air experienced higher mass loss, with the $NaNO_3$ and the (Na, Li, K)$NO_3$ samples losing c.a. 60 and 83 % of mass (dry basis), respectively, against only 45 % (dry basis) for both under a pure $CO_2$ atmosphere.

As described in reaction (19), $CO_2$ molecules react with oxygen ions to form carbonate ions, that is, $O^{2-}$ concentration is being reduced while $CO_3^{2-}$ concentration is increasing. The system will try to compensate this perturbation by producing oxygen ions, hence, the nitrate decomposition will be favored (right side of equation (20)). In turn, the nitrte concentration will increase, which justify the lower decomposition temperature of alkalis under a $CO_2$ atmosphere. In addition, due the formation of alkali carbonates, with higher molar mass than the correspondent oxides, i.e., $Na_2O$, $K_2O$ and $Li_2O$/$Li_2O_2$, the observed mass loss is lower under a $CO_2$ atmosphere. The alkali carbonates are very stable at high temperature, especially under $CO_2$ atmosphere, i.e., $Na_2CO_3$ and $K_2CO_3$, start to decompose slowly above 900 °C [69,70], and, in case of $Li_2CO_3$, the decomposition starts at 737 °C, but only at temperatures near 900 °C the decomposition is significant [71].

The decomposition temperature of each sample was defined as the upper stability limit of a mixture (T3), that is, the maximum temperature at which it loses 3 % of the initial weight and it is usually calculated for a heating rate of 10 K/ min, but T3 can vary depending on the experimental methods and conditions such as heating rate, crucible type or atmosphere [46]. The definition of the decomposition temperature allowed to set the working temperature range, with the melting point and the T3 being the extremes of that interval [46]. In the present study, since it was identified the water presence in all samples, the initial weight was replaced by the weight at 200 °C. The decomposition temperature range was also determined. The obtained results are summarized in Table 4-3.

**Table 4-3 Thermal decomposition of mono and ternary alkali salts under air and $CO_2$ atmosphere: working range and decomposition range (°C).**

| Sample | Atmosphere | T3 (°C) | Melting point (°C) | Working range (°C) | Decomposition range (°C) |
|---|---|---|---|---|---|
| **$NaNO_3$** | Air | 620 | 308 [25] | 308 - 620 | 620 - 814 |
| | $CO_2$ | 581 | | 308 - 581 | 581 - 731 |
| **(Na, Li, K)$NO_3$** | Air | 575 | 120 [72] | 120 - 575 | 575 - 818 |
| | $CO_2$ | 595 | | 120 - 595 | 595 - 736 |

The performed measurements show lower T3 for $NaNO_3$ under $CO_2$ than under air atmosphere, which is in line with the above explanation about the molten nitrate salts decomposition in presence of $CO_2$. For the ternary mixture it does not happen, and the T3 under $CO_2$ or under air atmospheres are closer.

In what regards to the working temperature range, the ternary mixture does offer a larger temperature window to operate when compared to that of the single salt $NaNO_3$. This advantage relies mostly on the already described in literature addition of the $LiNO_3$, that significantly decreases the melting temperature of the mixture with relation to the sodium nitrate salt, that is, 120 °C [72] against 308 °C [25], and not in the T3, that don't vary as much between both cases. Nevertheless, in air atmosphere the eutectic mixture presents a T3 lower than the single salt, which is associated to the presence of Li that prematurely decompose [72], but it does not happen under the $CO_2$ flow evidencing that the atmosphere type is also a relevant parameter.

Concerning to the $NaNO_3$ sample tested in an air atmosphere, the present experience obtained T3 = 620 °C. Bauer registered a thermal decomposition temperature T3 for $NaNO_3$ of 612.5 °C [73] and another scientific article reported 612.8 °C [46]. Associated relative errors < 1 % were obtained and considered negligible. Hence, it is possible to conclude that these temperatures agree with each other. However, Stern reported a decomposition temperature of 500 °C in air [45], which is not in line with the experimental T3 with an associated relative error of 24 %. The effect of heating rate, which was much faster is the present study can contribute for the observed differences.

The experimental T3 obtained for the eutectic mixture of 52 wt.% $KNO_3$, 18 wt.% $NaNO_3$ and 30 wt.% $LiNO_3$ under air was 575 °C. According to Bradshaw, the same mixture can be used up to 550 °C [45]. With an experimental error associated of less than 5 %, the result of the present experiment is verified.

The heat flow TG curves presented in Figure 4-21 exhibit several up and downward peaks, whether an endothermic or exothermic heat event occurs, respectively. The heat flow DTG curves (Figure 4-22) allow to properly identify the temperature at each event occurs.

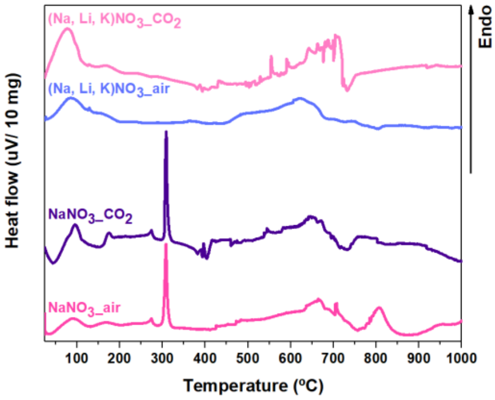

**Figure 4-21 – Heat flow profile of $NaNO_3$ and (Na,Li, K)$NO_3$ with temperature.**

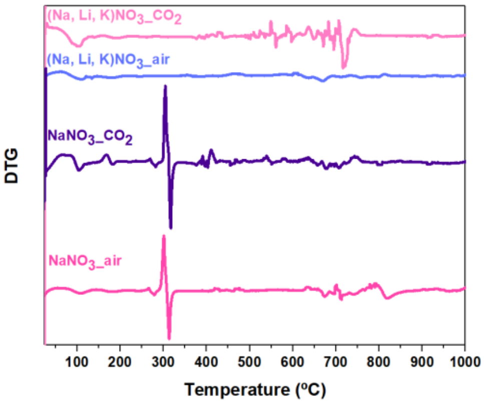

**Figure 4-22 – Heat flow first derivative profile of $NaNO_3$ and (Na,Li, K)$NO_3$ with temperature.**

The analysis of both the heat flow profiles and corresponding DTG curves reveals the existence of corresponding peaks in the same temperature intervals for all the samples (T3 ≥ 575 °C) regardless the atmosphere considerer. It is possible to establish a relation with the DTG curve represented (Figure 4-20), based on the fact that a wide endothermic heat flow corresponds to an abrupt fall of the mass at a high rate of decomposition of the salt [49].

The $NaNO_3$ melting (endothermic reaction) occurs around 310 °C, which agrees with literature [72]. In the case of ternary salt, it was difficult to identify the ternary salt melting. Due to the water vaporization, confirmed by the mass loss in both salts, only a small peak around 129 °C was visible for (Na, Li, K)$NO_3$ salt, meaning that probably the water vaporization is masking the endothermic reaction associated to the ternary salt melting.

## 4.2 PRELIMINARY $CO_2$ UPTAKE TGA STUDIES CARRIED OUT WITH MAGNESIUM OXIDE BASED SORBENTS DOPED WITH ALKALI METAL SALTS

The $CO_2$ sorption/ desorption sorbents' evaluation was preceded by a preliminary study focused on both the temperature conditions and the mono/ ternary alkali salts molar fraction used in the sorbent's doping. In this section all the experiments were carried out in the TGA apparatus.

### 4.2.1 ASSESSMENT OF SORPTION/ DESORPTION TEMPERATURE CONDITIONS

To assess the most promising sorption temperature, the mole fraction of $NaNO_3$ was fixed at 30 % and its $CO_2$ uptake was evaluated at 300 °C, 325 °C and 350 °C by TGA (80 ml/ min of $CO_2$ flow), according to the MgO's typical sorption reaction temperature range of 250 °C to 350 °C [25] and $NaNO_3$ melting temperature of 308 °C [25]. Figure 4-23 plots the carrying capacity (mg $CO_2$/ g sorbent) and the MgO conversion (%) of the 30 Na-MgO at 300 °C for 60 and 90 minutes and at 325 °C and 350 °C for 60 minutes, under an atmosphere of 100 % of $CO_2$.

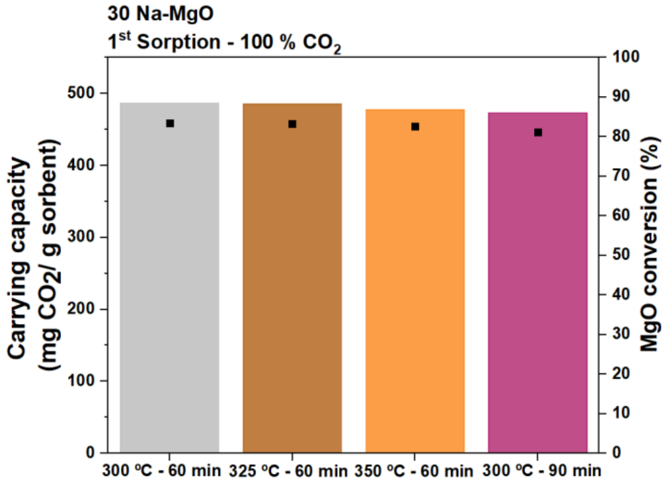

**Figure 4-23 – Carrying capacity (mg $CO_2$/ g sorbent) and MgO conversion (%) of 30 Na-MgO sorbent at 300 °C (60 and 90 min), at 325 °C and at 350 °C (60 min**

The analysis of Figure 4-23 allows to conclude that the $CO_2$ uptake of the tested sorbent is very similar either the sorption temperature was fixed at 300 °C, 325 °C or 350 °C, as well as the considered time interval was 60 or 90 minutes. Hence, it was decided to work at the lowest sorption temperature for the shortest sorption time interval, that is, 300 °C for 60 minutes.

Once the sorption temperature was selected, the desorption temperature profiles were studied. Figure 4-24 shows the TGA tests of the 30 Na-MgO sorbent at fixed sorption temperature of 300 °C but variable desorption temperatures of 420 °C, 430 °C, 435 °C, 440 °C and 445 °C. The desorption time interval was fixed in 60 minutes.

Conversely to the evidence found for the selected range of sorption temperature, it is possible to observe that these desorption temperature range significantly affects the amount of $CO_2$ released by the sorbent (Figure 4-24). The tendency is an increasing of the desorption efficiency as the desorption temperature increases. Figure 4-25 shows the quantification of the desorption efficiency (equation (29)) of the 30 Na-MgO sorbent for each tested desorption temperature and at the fixed sorption temperature of 300 °C.

$$Desorption\ efficiency\ (\%) = \frac{m_{1st\ sorption} - m_{1st\ desorption}}{m_{1st\ sorption}} \times 100 \qquad (29)$$

Where $m_{1st\ sorption}$ and $m_{1st\ desorption}$ correspond to the mass of the first sorption and of the first desorption, respectively.

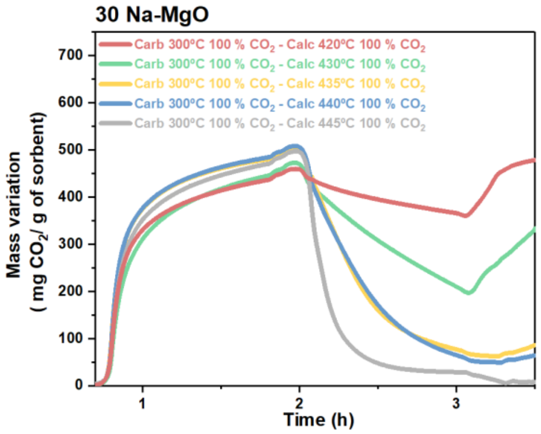

**Figure 4-24 – $CO_2$ desorption profile of 30 Na-MgO sorbent after sorption at 300 °C and at variable desorption temperatures of 420 °C, 430 °C, 435 °C, 440 °C and 445°C (80 ml/ min under CO2 flow, 60 min).**

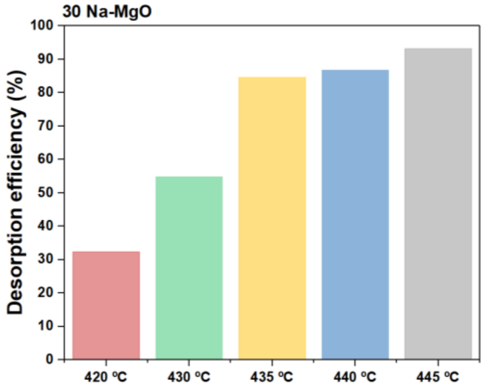

**Figure 4-25 – $CO_2$ desorption efficiency of the 30 Na-MgO sorbent after sorption at 300 °C and at variable desorption temperatures of 420 °C, 430 °C, 435 °C, 440 °C and 445 °C (80 ml/ min under CO2 flow, 60 min).**

The analysis of Figure 4-25 shows that desorption at 420 °C is not effective, since only around 31 % of the $CO_2$ captured in 1st sorption is actually released in the following desorption step. At 430 °C, the desorption efficiency arises to 56 %. Even more favorable results are obtained with higher temperatures. Sorption efficiencies of 86 %, 87 % and 94 % are achieved when using a temperature of 435 °C, 440 °C or 445 °C, respectively.

Summarizing, the conditions to be used in section 4.3.1 (sorption and desorption in a TGA apparatus) were defined as the following: sorption temperature of 300 °C for the time interval of 60 minutes and desorption temperature of 445 °C for 60 minutes.

### 4.2.2 ASSESSMENT OF MOLAR FRACTION EFFECT DURING MONO AND TERNARY ALKALI METAL SALTS DOPING

Considering a window temperature from 20 °C to 500 °C, and a heating ramp of 10 °C/ min, TGA studies (80 ml/ min, $CO_2$ flow) were conducted on samples of MgO sorbent undoped and doped with different molar fractions of mono or ternary AMS to assess the promotors ratio (AMS/ MgO) effect on $CO_2$ uptake. Figure 4-26 and Figure 4-27 plot the temperature-programmed sorption followed by TGA of a series of single $NaNO_3$ or ternary mixture of (Na, Li, K)$NO_3$ promoted MgO sorbents, respectively.

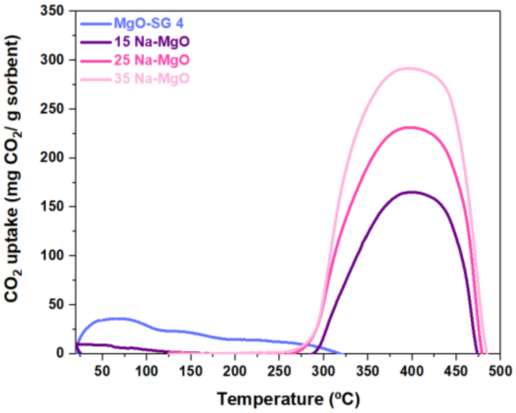

**Figure 4-26 – Profile of $CO_2$ uptake of undopped MgO-SG 4 sorbent and doped with 15 % of $NaNO_3$, 25 % of $NaNO_3$ and 35 % of $NaNO_3$.**

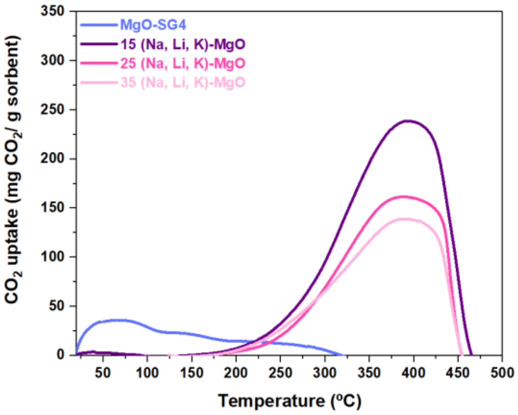

**Figure 4-27 – Profile of $CO_2$ uptake of undopped MgO-SG4 sorbent and doped with 15 % of (Na, Li, K)$NO_3$, 25 % of (Na, Li, K)$NO_3$ and 35 % of (Na, Li, K)$NO_3$**

Unpromoted MgO-SG 4 sorbent immediately captures $CO_2$ right at the beginning of the TGA test, achieving its maximum $CO_2$ uptake at 50 °C, and gradually releases it with the increasing of the temperature from 75 °C to 325 °C. The corresponding $CO_2$ desorption peak is significantly wider than those of the MgO promoted samples, which relates to the type of the surface of each sorbent and, in turn, with the type of species formed during sorption. In the case of the unpromoted MgO-SG 4 sorbent, $CO_2$ weakly physisorbs and chemisorbs as a monodentate gas [25]. In contrast, the extent of sorption was insignificant for all the promoted MgO-SG 4 samples at low temperatures, until it reaches a certain value of temperature, where it starts to uptake $CO_2$ more dramatically. In this way, the AMS impregnation is proved to increase considerably the $CO_2$ uptake by the MgO sorbents. The mentioned temperature was determined as the inflection point of each $CO_2$ uptake curve, that is, where the corresponding second derivate changes its signal. As a matter of example, the determination of the inflection temperature of the 25 Na-MgO and of the 25 (Na, Li, K)-MgO is illustrated in Figure 4-29 and in Figure 4-31, respectively, and the results are summarized in Table 4-4. The determinations for the remaining samples can be consulted in section 8.2 (appendix). The different threshold temperatures were obtained for each sample. This evidence is attributed to the physical state of the corresponding AMS, ranging from solid to melting. At low temperatures, the $CO_2$ uptake is obstructed due to the formation of a solid layer of nitrates that covers the surface of the sorbent. Only with the increasing temperature until close to the melting point of the AMS, this covering solid layer starts to melt. It is called the pre-melting phenomenon, where an interfacial liquidlike film of the partially disordered surface of the promoted sorbent is formed at temperatures below the corresponding melting point, enhancing the kinetic of the $CO_2$ uptake [74,75]. For example, the melting point of the single salt $NaNO_3$ is 308 °C, but it suffers a solid-state transition from an ordered to a disordered rhombohedral structure at a lower temperature of 275 °C that, in turn, is believed to potentiate its pre-melting [25]. The present experiments indicate that this transition occurs at even lower temperatures. In addition, the samples of MgO-SG 4 sorbent promoted with single $NaNO_3$ appear to have higher threshold temperatures than that of the corresponding MgO-SG 4 sorbent promoted with the ternary mixture. Hence, it is suggested that to promote the MgO sorbent with the eutectic mixture accentuates the reduction of the sorption temperature. It is described in literature a sorption temperature of 160 °C using the ternary eutectic mixture of (Na, Li, K)$NO_3$ [25]. Here it was possible to reduce the temperature to around 175 °C. The difference between the inflection temperature and the temperature correspondent to the maximum $CO_2$ uptake (mg $CO_2$/ g sorbent) achieved during the temperature-programmed experiment suggests that at low temperatures the accelerating effect of the addition of alkali metal nitrates on the $CO_2$ sorption by MgO is reduced, which is justified by the thermodynamic equilibrium of MgO/ $MgCO_3$ [25].

According to Figure 4-26, the $CO_2$ uptake increases with the increasing percentage of the single salt doping. Conversely, in Figure 4-27, the $CO_2$ uptake increases with the reduction of the impregnation percentage of the ternary mixture. These results suggest that both the type and the percentage of AMS influence the extent of the sorption. For the samples of MgO-SG 4 promoted with $NaNO_3$, it appears that increasing the percentage of the single salt enhances the $CO_2$ sorption by the sorbent, which can be attributed to the fact that the interfacial area between the MgO and the $NaNO_3$ was improved, making the surface of the sorbent more available to the $CO_2$ uptake. Nevertheless, it is reported in literature an optimal molar ratio of $NaNO_3$ of 10 % and a subsequent decreasing of the extent of sorption with increasing quantities of $NaNO_3$, suggesting that a certain thickness of the molten layer covering the surface of the sorbent limits the $CO_2$ uptake, by increasing the mass transfer resistance [25]. Considering the results obtained for the impregnated with the ternary mixture samples in the present work, this layer thickness seems to have been achieved.

It was also obtained the maximum instantaneous rate of change of temperature with respect to $CO_2$ uptake corresponding to the upward peak of the first derivative of each TG curve of the tested samples. As a matter of example, its determination is illustrated in Figure 4-28 and Figure 4-30 for the 25 Na-MgO and for the 25 (Na, Li, K)-MgO samples, respectively. The determinations for the remaining samples can be consulted in section 8.2 (appendix). The results are summarized in Table 4-4 and indicate that the maximum $CO_2$ uptake rate temperature does not significantly vary with the AMS impregnation percentage, for both sorbents. The samples of MgO sorbent impregnated with the ternary mixture registered higher maximum conversion temperatures than the ones impregnated with the single salt. As the former present lower inflection temperatures, it is also possible to associate them with larger sorption temperature range, that is, extents of sorption. Moreover, the obtained temperatures are in line with the defined sorption temperature of 300 °C in section 4.2.1.

In Table 4-4 there are also listed the maximum $CO_2$ uptakes (mg $CO_2$/ g sorbent) of each sample. It is described in literature a maximum conversion of 19 mg $CO_2$/ g sorbent for an unpromoted MgO [25], whilst the synthesized MgO sorbent in the present work yielded a higher value of 36 mg $CO_2$/ g sorbent. Yet, the same work managed to achieve maximum conversions of 432 and 474 mg $CO_2$/ g sorbent for MgO sorbents promoted with 10 % of $NaNO_3$ and 10 % of (Na, Li, K)$NO_3$ [25], both higher values than any maximum conversion obtained in the present experiments. In addition, the highest $CO_2$ uptake of 292 mg $CO_2$/ g sorbent was obtained for the MgO-SG 4 sorbent doped with 35 % of $NaNO_3$, which, in turn, corresponds to the highest percentage of $NaNO_3$. It suggests that sorbents with elevated percentages of $NaNO_3$ might benefit from the achieved lower inflection temperature comparatively to lower nitrates doping, since higher doping favors ion dynamics of the reactant species and higher concentrations of $Mg^{2+}$ ions in molten $NaNO_3$ [25]. For the ternary mixture, the highest $CO_2$ uptake was 239 mg $CO_2$/g sorbent for the MgO-SG 4 doped with 15% of AMS, and apparently its molar fraction does not affect the beginning of the $CO_2$ uptake, since inflection temperature is more or less constant.

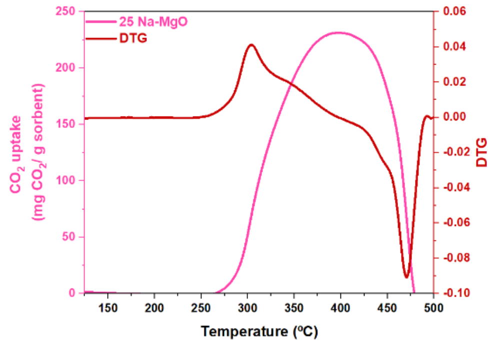

**Figure 4-28 – $CO_2$ uptake profile of MgO-SG 4 sorbent doped with 25 % of $NaNO_3$ and respective first derivative.**

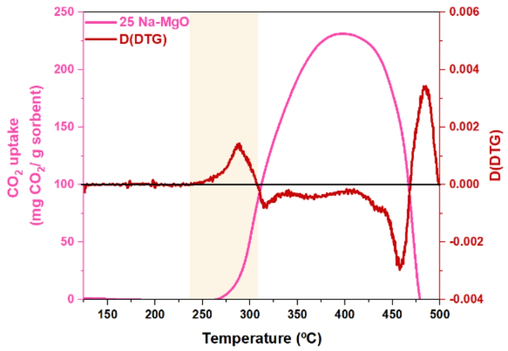

**Figure 4-29 – $CO_2$ uptake profile of MgO-SG 4 sorbent doped with 25 % of $NaNO_3$ and respective second derivative (acelerating sorption is highlight in yellow).**

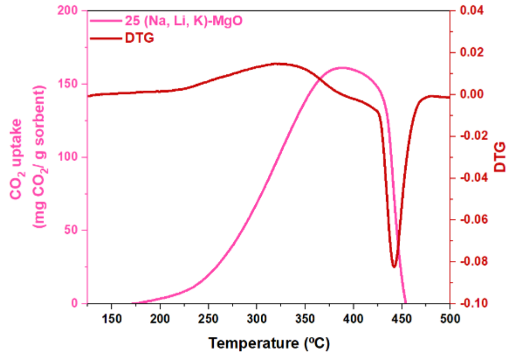

**Figure 4-30 – $CO_2$ uptake profile of MgO-SG 4 sorbent doped with 25 % of (Na, Li, K)$NO_3$ and respective first derivative.**

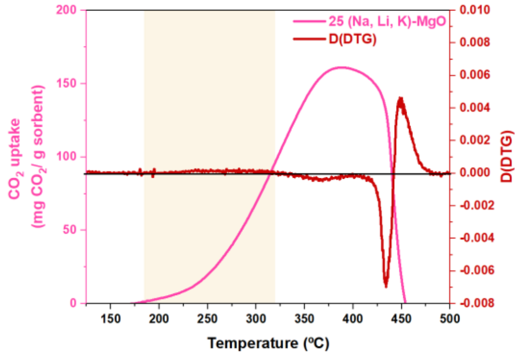

**Figure 4-31 – $CO_2$ uptake profile of MgO-SG 4 sorbent doped with 25 % of (Na, Li, K)$NO_3$ and respective second derivative (acelerating sorption is highlight in yellow).**

**Table 4-4 – Properties of MgO sorbent undoped and doped with different molar fractions of mono or ternary AMS: maximum instantaneous rate of change of temperature with respect to $CO_2$ uptake (°C), inflection temperature (°C), maximum $CO_2$ uptake temperature (°C) and maximum $CO_2$ uptake (mg $CO_2$/ g sorbent).**

| MgO-based sorbent | Unpromoted | Promoted | | | | | |
|---|---|---|---|---|---|---|---|
| | | $NaNO_3$ (%) | | | (Na, Li, K)$NO_3$ (%) | | |
| | | 15 | 25 | 35 | 15 | 25 | 35 |
| **Maximum instantaneous rate of change of temperature with respect to $CO_2$ uptake (°C)** | - | 310 | 304 | 310 | 322 | 319 | Peak not defined |
| **Inflection temperature (°C)** | - | 234 | 237 | 240 | 175 | 184 | Not detected |
| **Maximum $CO_2$ uptake temperature (°C)** | - | 399 | 396 | 395 | 391 | 388 | 388 |
| **Sorption temperature range (°C)** | 20 - 50 | 234 - 399 | 237 - 396 | 240 - 395 | 175 - 391 | 184 - 388 | - |
| **Maximum $CO_2$ uptake (mg $CO_2$/ g sorbent)** | 36 | 165 | 231 | 292 | 239 | 161 | 139 |

The crystalline structures of the MgO-SG 4 sorbent impregnated with 15, 25 and 35 % of either $NaNO_3$ or ternary mixture of $KNO_3$, $NaNO_3$ and $LiNO_3$ were studied by powder XRD after undergoing TGA tests. Due to the similarity of these XRD patterns comparatively with the one obtained before the TG experiments (section 4.1.2, Figure 4-10 and Figure 4-11), those are illustrated in Figure 8-18 and Figure 8-19 (section 8.3, appendix).

In Figure 4-32 and Figure 4-33 it is plotted the variation of the MgO crystallite size of the sorbents before and after TG tests using impregnation with single salt or with ternary mixture. Summarizing, the AMS impregnation contributes to the growth of the MgO crystallites, with the increasing of the MgO crystallite size being higher when the impregnation uses the ternary mixture of $KNO_3$, $NaNO_3$ and $LiNO_3$ than the single salt $NaNO_3$. The variation of MgO crystallite size (ΔCS) (equation (30)), of sorbent dopped with $NaNO_3$ varies between 50 and 60 % but increases for values between 160 to 200 % for the sorbent with higher (Na, Li, K)$NO_3$ content (according to Table 4.1). Conversely, the impregnated with $NaNO_3$ samples registered a more elevated rising of the crystallite size before and after TGA tests, i.e., between 50 and 60%, and 7 % to 15%, for $NaNO_3$ and (Na, Li, K)$NO_3$, respectively. The AMS molar percentage of the impregnation doesn't affect the crystallite size, regardless of it uses the single salt or the ternary mixture.

$$\Delta CS = \frac{\mathrm{CS}_{\text{dopped sorb}} - \mathrm{CS}_{\text{undopped sorb}}}{\mathrm{CS}_{\text{undopped sorb}}} \times 100 \tag{30}$$

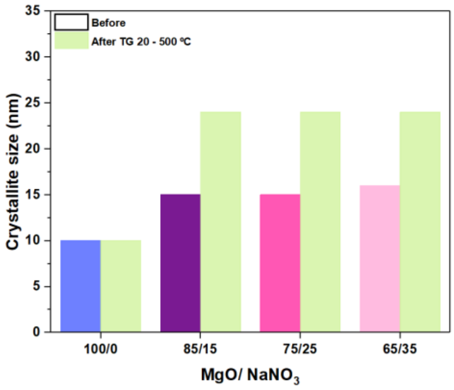

**Figure 4-32 – Crystallite size of undopped MgO-SG 4 sorbent and dopped with 15 % of $NaNO_3$, 25 % of $NaNO_3$ and 35 % of $NaNO_3$, before and after TG test between 20 and 500 °C.**

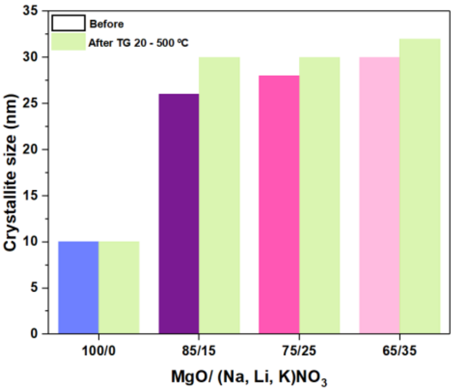

**Figure 4-33 – Crystallite size of undopped MgO-SG 4 sorbent and dopped with 15 % of (Na, Li, K)$NO_3$, 25 % of (Na, Li, K)$NO_3$ and 35 % of (Na, Li, K)$NO_3$, before and after TG test between 20 and 500 °C.**

### 4.2.3 POROUS SUPPORT ADDITION

Considering a window temperature from 25 °C to 500 °C, and a heating ramp of 10 °C/ min, TGA studies (80 ml/ min $CO_2$ flow) were conducted on samples of supported MgO sorbents (Ca or Ce-based) undoped and doped with 15 % of (Na, Li, K)$NO_3$. Figure 4-34 plots the temperature-programmed sorption followed by TGA of MgO-SG-Ca and 15 (Na, Li, K)-MgO-Ca sorbents. Figure 4-35 plots the temperature-programmed sorption followed by TGA of MgO-SG-Ce and 15 (Na, Li, K)-MgO-Ce sorbents.

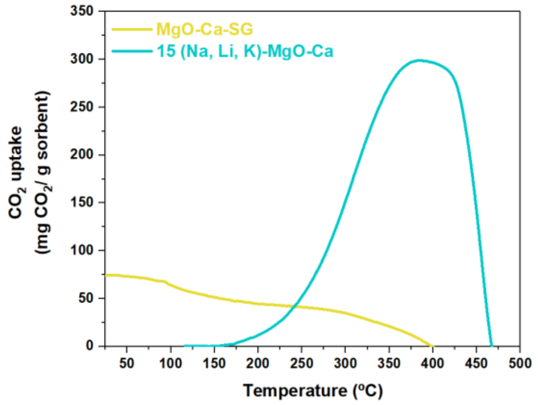

**Figure 4-34 – Profile of $CO_2$ uptake of the MgO-Ca-SG sorbent and of the impregnated sample 15 (Na, Li, K)-MgO-Ca.**

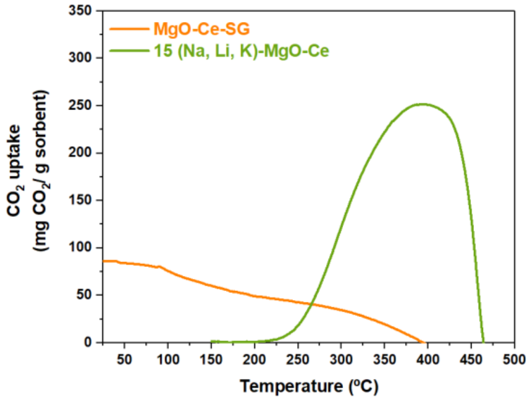

**Figure 4-35 – Profile of $CO_2$ uptake of the MgO-Ce-SG sorbent and of the impregnated sample 15 (Na, Li, K)-MgO-Ce.**

Unpromoted MgO-Ca-SG and MgO-Ce-SG sorbents register immediately its maximum $CO_2$ uptake of 73 mg $CO_2$/ g sorbent and 86 mg $CO_2$/ g sorbent, respectively, at the beginning of the TGA test at 25 °C and gradually release it with the increasing of the temperature until ~400 °C. Both sorbents exhibit $CO_2$ desorption peaks significantly wider than those of the corresponding AMS promoted samples. Conversely, the $CO_2$ uptake of the 15 (Na, Li, K)-MgO-Ca and of the 15 (Na, Li, K)-MgO-Ce sorbents was negligible at low temperatures, until it reaches the respective inflection temperature. This parameter was obtained as it was explained in section 4.2.2. The second derivative with respect to mass of the 15 (Na, Li, K)-MgO-Ca and of the 15 (Na, Li, K)-MgO-Ce sorbents is plotted in Figure 8-15 and Figure 8-17, respectively, in section 8.2 (appendix). In addition, the maximum instantaneous rate of change of temperature with respect to $CO_2$ uptake (°C) was also determined as it was explained in section 4.2.2. The first derivative with respect to mass of the 15 (Na, Li, K)-MgO-Ca and of the 15 (Na, Li, K)-MgO-Ce sorbents is plotted in Figure 8-14 and Figure 8-16, respectively, in section 8.2 (appendix). The promoted MgO-Ce-SG sorbent showed a higher inflection temperature than the promoted MgO-Ca-SG, meaning that the latter starts the $CO_2$ uptake sooner. As expected, the AMS doping enhanced considerable the $CO_2$ uptake of both MgO sorbents, with 15 (Na, Li, K)-MgO-Ca and of the 15 (Na, Li, K)-MgO-Ce sorbents achieving a maximum $CO_2$ uptake of 299 mg $CO_2$/ g sorbent and 252 mg $CO_2$/ g sorbent at 384 °C and 393 °C, respectively. Summarizing, unpromoted MgO-Ce-SG exhibited higher $CO_2$ uptake than MgO-Ca-SG, but AMS doping was more effective for the latter, with 15 (Na, Li, K)-MgO-Ca exhibiting higher $CO_2$ uptake than 15 (Na, Li, K)-MgO-Ce. Moreover, 15 (Na, Li, K)-MgO-Ca also provides a more extent sorption than 15 (Na, Li, K)-MgO-Ce, since the former presents a wider sorption temperature range than the latter.

Literature reports a $CO_2$ uptake of 317 mg $CO_2$/ g sorbent for an MgO sorbent promoted with 5 % (mol) of $CaCO_3$ and impregnated with 20 % of ternary mixture (Na, Li, K)$NO_3$ at 300 °C for 30 minutes under an atmosphere consisting of 30 % of $CO_2$ [35], which is in line with the $CO_2$ uptake obtained for the 15 (Na, Li, K)-MgO-Ca sorbent, despite the difference between the $CO_2$ atmospheres. Jin et al. synthesized a supported with $CeO_2$ (10 % mol) impregnated with a mixture of (Na, Li, K)$NO_3$ plus ($Na_2$, $K_2$)$CO_3$ (17 % mol) MgO sorbent that achieved a $CO_2$ uptake of 450 mg $CO_2$/ g sorbent at 325 °C for 120 minutes under 100 % $CO_2$ [36], that is almost the double of the $CO_2$ uptake obtained for the 15 (Na, Li, K)-MgO-Ce. Stands out that in the above examples a temperature plateau for 30 min (300 °C) and 120 min (325 °C), respectively, was applied, while the present study does not include a temperature plateau.

Table 4-5 summarizes the maximum instantaneous rate of change of temperature with respect to $CO_2$ uptake, the inflection temperature, the maximum $CO_2$ uptake temperature, the sorption temperature range and the maximum $CO_2$ uptake for the MgO-Ca-SG and MgO-Ce-SG unpromoted and promoted with 15 % of (Na, Li, K)$NO_3$ sorbents.

**Table 4-5 – Properties of MgO-Ca-SG and MgO-Ce-SG sorbents undoped and doped with 15 % of (Na, Li, K)$NO_3$: maximum instantaneous rate of change of temperature with respect to $CO_2$ uptake (°C), inflection temperature (°C), maximum $CO_2$ uptake temperature (°C) and maximum $CO_2$ uptake (mg $CO_2$/ g sorbent).**

| MgO-based sorbent | MgO-SG 4 * | MgO-Ca-SG | | MgO-Ce-SG | |
|---|---|---|---|---|---|
| | % (Na, Li, K)$NO_3$ | | | | |
| | 15 | 0 | 15 | 0 | 15 |
| **Maximum instantaneous rate of change of temperature with respect to $CO_2$ uptake (°C)** | 322 | - | 308 | - | 294 |
| **Inflection temperature (°C)** | 175 | - | 153 | - | 210 |
| **Maximum $CO_2$ uptake temperature (°C)** | 391 | 25 | 384 | 25 | 393 |
| **Sorption temperature range (°C)** | 175 - 391 | - | 153 - 384 | - | 210 - 393 |
| **Maximum $CO_2$ uptake (mg $CO_2$/ g sorbent)** | 239 | 73 | 299 | 86 | 252 |

*** Values from Table 4-4 for comparasion**

The 15 (Na, Li, K)-MgO-Ca sorbent starts to uptake $CO_2$ at lower temperature (153 °C) than the 15 (Na, Li, K)-MgO-Ce (210 °C), however the last one reaches the maximum instantaneous rate of change of temperature with respect to $CO_2$ uptake a little early (294 vs 308 °C). The higher inflection temperature of 15 (Na, Li, K)-MgO-Ce was unexpected since the same alkali ternary mixture was used. A possible explanation can be the high dispersion of both the $CeO_2$ and AMS on the sorbent. As it can be observed in XRD patterns of samples supported with Ce (Figure 4.12), broader peaks are observed meaning there is a high dispersion of these compounds in the sorbent, which probably delays the molten of the ternary alkali salts mixture. Yu et al. synthetized $CeO_2$-MgO and MgO sorbents and verified that, despite the similarity of their surface areas, the promoted sorbent had an increased $CO_2$ uptake, which was justified by changes in the pore structures and by the increase in the basicity of the MgO phase induced by the addition of $CeO_2$ [76]. In the present study, corresponding values of $S_{BET}$ are also similar (31 vs 32 g/ m$^2$), and, comparatively with the unsupported sorbent, the maximum $CO_2$ uptake of 15 (Na, Li, K)-MgO-Ce (239 vs 252 mg $CO_2$/ g sorbent) was slightly improved. It must be noted that any temperature plateau was considered during this experiment.

In addition, it was established a comparison between the DTG curves of the 15 (Na, Li, K)-MgO and of the 15 (Na, Li, K)-MgO-Ca sorbents.The result is illustrated in Figure 4-36 and shows that the 15 (Na, Li, K)-MgO-Ca sorbent starts to uptake $CO_2$ at lower temperatures, which is in accordance with it presenting a lower inflection temperature of 153 °C than the 15 (Na, Li, K)-MgO sorbent (175 °C). Moreover, the plotted DTG curves indicate that the impregnated Ca supported sorbent has a higher rate of $CO_2$ uptake. It is advanced that occurred the formation of the double salt $CaMg(CO_3)_2$, through the dissolution of carbonates, that have appreciable solubility in molten salts, subsequently reacting with the $CO_2$ molecules during $CO_2$ sorption by 15 (Na, Li, K)-MgO-Ca sorbent. In another hand, the comparison between the DTG curves of the 15 (Na, Li, K)-MgO and of the 15 (Na, Li, K)-MgO-Ce sorbents (Figure 4-37), indicates that the unsupported sorbent starts to uptake $CO_2$ first than the latter, which is in line with the corresponding inflection temperatures of 175 °C and 210 °C. Yet, the 15 (Na, Li, K)-MgO-Ce sorbent is associated with higher rate of $CO_2$ uptake. As expected, the addition of both Ca and Ce-based supports improved the MgO sorbents' performance [10,29].

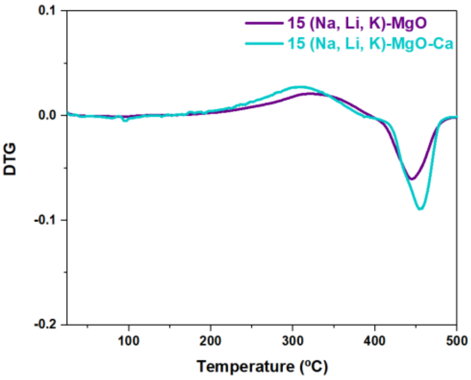

**Figure 4-36 – DTG curves of 15 (Na, Li, K)-MgO and 15 (Na, Li, K)-MgO-Ca sorbents with temperature increase from 20 to 500 °C.**

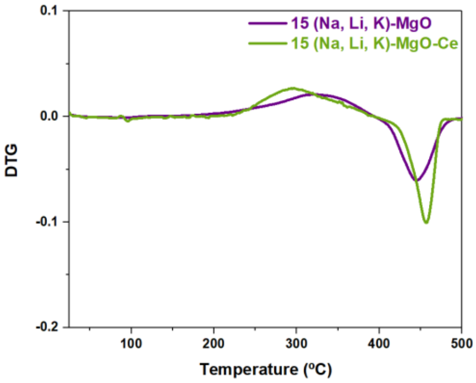

**Figure 4-37 – DTG curves of 15 (Na, Li, K)-MgO and 15 (Na, Li, K)-MgO-Ce sorbents with temperature increase from 20 to 500 °C.**

In Figure 4-38 and Figure 4-39 it is plotted the variation of the MgO crystallite size of the Ca or Ce-based supported MgO sorbents, respectively, before and after TGA tests using impregnation with 15 % of (Na, Li, K)$NO_3$. Both unpromoted MgO-Ca-SG and MgO-Ce-SG sorbents maintained the MgO crystallite size after undergoing the TGA test. The increase of MgO crystallites for both 15 (Na, Li, K)-MgO-Ca and 15 (Na, Li, K)-MgO-Ce is mainly due to the AMS impregnation procedure, associated to an increase of 150 % and 125 % (Table 4-2), while due to the TGA experiment the increase was 10 % and 22 %, respectively. Hence, the AMS impregnation with 15 % (Na, Li, K)$NO_3$ affected identically the supported MgO-Ca-SG and MgO-Ce-SG sorbents.

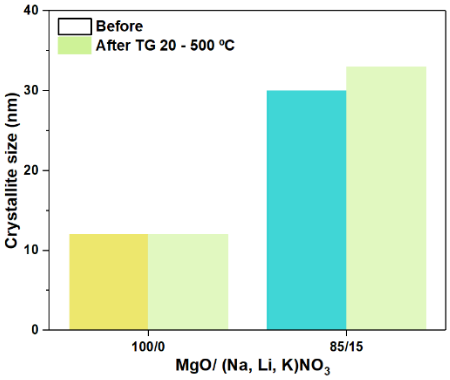

**Figure 4-38 – Crystallite size of undopped and dopped MgO-Ca-SG with 15 % of (Na, Li, K)$NO_3$ before and after TG experiment between 20 and 500 °C.**

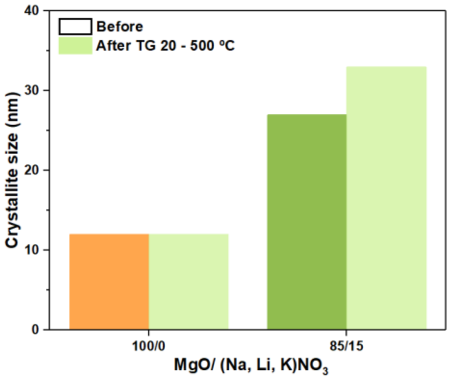

**Figure 4-39 – Crystallite size of undopped and dopped MgO-Ce-SG with 15 % of (Na, Li, K)$NO_3$ before and after TG experiment between 20 and 500 °C.**

## 4.3 $CO_2$ SORPTION/DESORPTION STUDIES

The previous section helped with the identification of sorption and desorption temperature conditions, influence of AMS type and fraction doping, and Ca or Ce support effect on $CO_2$ uptake. These experiments were carried out in a TG apparatus, but only 1 sorption/ desorption cycle was performed. In this section, it was performed a TG screening of cyclic sorption/ desorption carrying capacity along 5 cycles, and one test with 12 cycles (section 4.3.1.), considering the most promising conditions and sorbents identified in 4.2. This procedure was followed by 10 sorption/ desorption cycles in a fixed-bed reactor (section 4.3.2), using supported and unsupported sorbents: sorption with 25% or 100% of $CO_2$ and desorption in air atmosphere. Fixed type and fraction of AMS were considered.

### 4.3.1 TGA STUDIES

The $CO_2$ uptake and cyclic stability of five different samples consisting of MgO-SG 4 sorbent impregnated with 35 % of $NaNO_3$, 25 % of $NaNO_3$, 10 % of (Na, Li, K)$NO_3$, 15 % of (Na, Li, K)$NO_3$ and 25 % (Na, Li, K)$NO_3$ were tested in a TGA by performing 5 sorption/ desorption cycles. The sorbent 10 (Na, Li, K)-MgO was not tested in 4.2, but due to the improvement of $CO_2$ uptake for the sorbent with lower molar fraction of the ternary mixture, i.e., 15 % against 25 %, the 10 (Na, Li, K)-MgO sample was prepared and tested. Figure 4-40 and Figure 4-41 show the cyclic $CO_2$ sorption/ desorption tests of the MgO-SG 4 sorbent impregnated with the single salt $NaNO_3$ and with the ternary mixture of (Na, Li, K)$NO_3$, respectively. Figure 4-42 and Figure 4-43 plot the carrying capacity and the MgO conversion of the cyclic $CO_2$ sorption/ desorption tests of the MgO-SG 4 sorbent impregnated with the single salt $NaNO_3$ and with the ternary mixture of (Na, Li, K)$NO_3$, respectively.

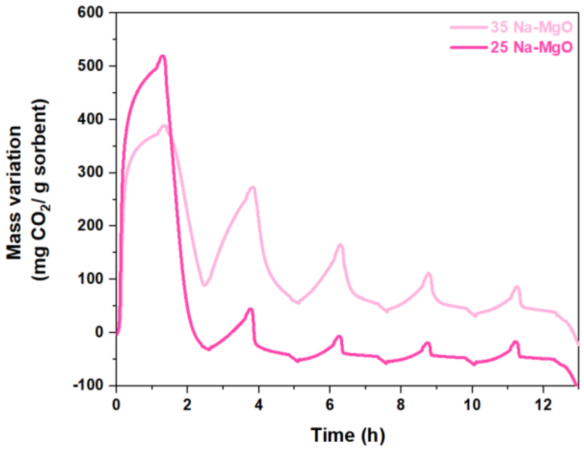

**Figure 4-40 – Profile of sorption (300 °C, 60 min) and desorption (445 °C, 60 min) tests carried out along 5 cycles in a TG (80 ml/ min of $CO_2$) for 35 Na-MgO and 25 Na-MgO sorbents.**

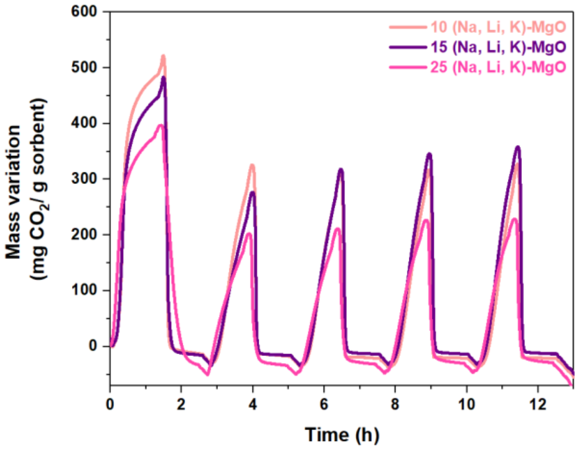

**Figure 4-41 – Profile of sorption (300 °C, 60 min) and desorption (445 °C, 60 min) tests carried out along 5 cycles in a TG (80 ml/ min of $CO_2$) for 10 (Na, Li, K)-MgO, 15 (Na, Li, K)-MgO and 25 (Na, Li, K)-MgO sorbents.**

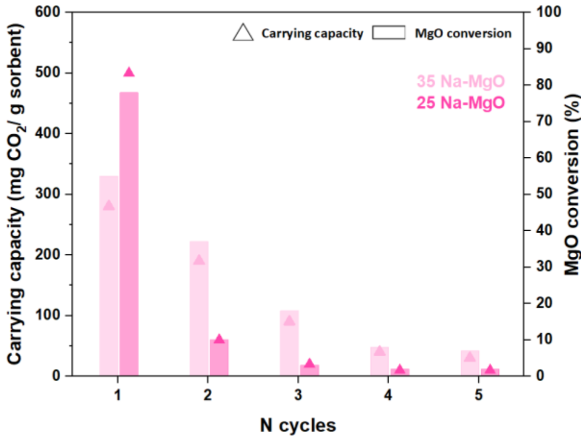

**Figure 4-42 – Carrying capacity (mg $CO_2$/g sorbent) and MgO conversion (%) of 35 Na-MgO and 25 Na-MgO sorbents achieved along 5 sorption/ desorption cycles in a TG apparatus.**

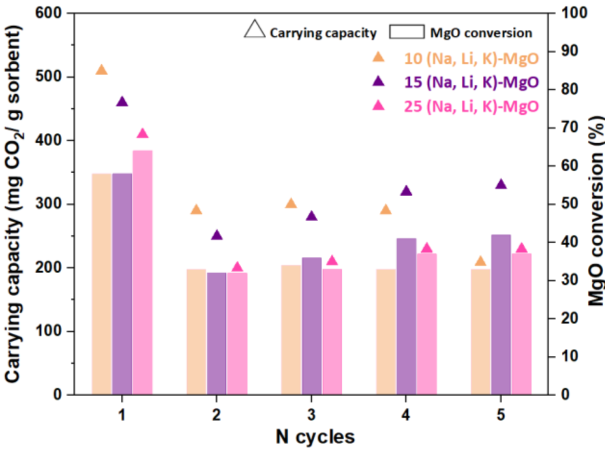

**Figure 4-43 – Carrying capacity (mg $CO_2$/g sorbent) and MgO conversion (%) of 10 (Na, Li, K)-MgO, 15 (Na, Li, K)-MgO and 25 (Na, Li, K)-MgO sorbents achieved along 5 sorption-desorption cycles in a TG apparatus.**

Both MgO-SG 4 samples impregnated with 35 % of $NaNO_3$ and with 25 % of $NaNO_3$ exhibited a general decreasing $CO_2$ uptake profile over the 5 cycles, with an accentuate decay in the 2nd cycle followed by a gradual reduction until the last cycle. The 35 Na-MgO registered an MgO conversion of 55 % at the first cycle, of 35 % at the second cycle and of only 7 % at the last cycle. The 25 Na-MgO achieved even higher reductions, with an MgO conversion of 78 % at the 1st cycle, 10 % at the 2nd cycle and of only 2 % at the 5th cycle. Although performing well at the 1st cycle, both sorbents did not manage to achieve high values of MgO conversion, as well as did not demonstrate to be stable over repeated cycles.

A qualitative comparison of Figure 4-40 and Figure 4-41 immediately reveals that the MgO-SG 4 samples impregnated with the ternary mixture of (Na, Li, K)$NO_3$ performed better than the ones impregnated with the single salt $NaNO_3$. Regardless the molar percentage of ternary impregnation used, the three tested samples exhibited a profile consisting of intense, well-defined and consistent peaks over the 5 adsorption/ desorption cycles, that is, good $CO_2$ uptakes and good cyclic stability. The 10 (Na, Li, K)-MgO achieved a MgO conversion of 58 % at the 1st cycle that was reduced to 33 % at the last cycle. The 15 (Na, Li, K)-MgO reached a MgO conversion of 58 % and of 42 % at the 1st and 5th cycles, respectively. Finally, the 25 (Na, Li, K)-MgO presented a MgO conversion of 64 % at the 1st cycle and of 37 % at the last cycle. Although the 25 (Na, Li, K)-MgO has the highest MgO conversion at the first cycle, it is also associated with the lowest MgO conversion at the last cycle. The 10 (Na, Li, K)-MgO and the 15 (Na, Li, K)-MgO sorbents registered the same MgO conversion at the 1st cycle, yet the former showed a lower MgO conversion at the 5th cycle. Hence, the 15 (Na, Li, K)-MgO sorbent was considered the one performing better among this tested set, due to presenting good MgO conversion values and remaining stable over 5 sorption/ desorption repeated cycles. Subsequently, it was performed a TG test of 12 sorption/ desorption cycles using the 15 (Na, Li, K)-MgO sorbent (Figure 4-44). Figure 4-45 plots the carrying capacity and the MgO conversion of the cyclic $CO_2$ sorption/ desorption test of the 15 (Na, Li, K)-MgO sorbent.

Dal Pozzo et al. reported a MgO sorbent doped with 10 % of (Na, Li, K)$NO_3$ that registered carrying capacities of 480 and 410 mg $CO_2$/ g sorbent for the 1st and 5th cycles, respectively [25]. Another article describes carrying capacities of 440 and 352 mg $CO_2$/ g sorbent for the 1st and 5th cycles, respectively, of an MgO sorbent impregnated with 15% of the same ternary mixture [33]. Since the synthesized 15 (Na, Li, K)-MgO sorbent varied its carrying capacity between 460 and 330 mg $CO_2$/ g sorbent between the 1st and the 5th cycle, it is possible to affirm that the results are in accordance with literature.

The deactivation of MgO-based sorbents along cycles can be justified by both the sintering of the sorbents and the segregation of the nitrates. These processes occur with both AMS types of promotors, being much more pronounced for the $NaNO_3$, though. Dal Pozzo stated that the sorbents promoted by AMS loose surface area and pore volume mainly during the first sorption/ desorption cycle, which is correlated with the occurrence of accentuated sintering [25]. The authors stand out that the sintering appears to be more pronounced for the sorbents that present higher $CO_2$ carrying capacities during the 1st cycle. Its explanation is based on the low melting temperature of $MgCO_3$ (Tammann temperature ~ 180 °C), i.e., if $MgCO_3$ is in a higher concentration in the sample, the presence of a melting phase will be more intense, so the quantity of sintered compounds will increase. As show in Figure 4-19, the $NaNO_3$ and (Na, Li, K)$NO_3$ decompositions only start for values above 600 °C, so they remain stable under the temperatures used for the above sorption/ desorption tests, meaning that does not justify the sorbents' loss of reactivity. However, the segregation of AMS can occur, like was demonstrated by SEM images for $NaNO_3$ [25], and in this work where the segregation of K particles was showed in Figure 4-17. Due to the AMS segregation, the dispersion of MgO in the melted phase of nitrates will be reduced, and the $CO_2$ carrying capacity decreases. Apparently, under the used conditions, this process is more accentuated for $NaNO_3$ salt.

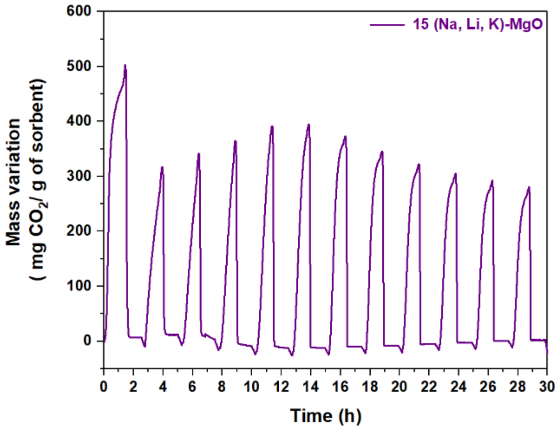

**Figure 4-44 – Profile of sorption (300 °C, 60 min) and desorption (445 °C, 60 min) tests carried out along 12 cycles in a TG (80 ml/ min of $CO_2$) for 15 (Na, Li, K)-MgO sorbent.**

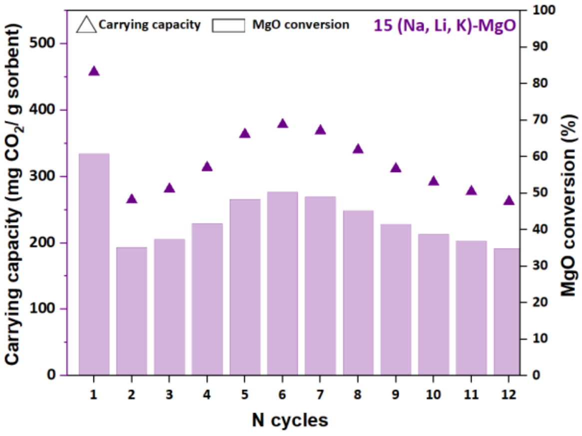

**Figure 4-45 – Carrying capacity (mg $CO_2$/ g sorbent) and MgO conversion (%) of 15 (Na, Li, K)-MgO sorbent achieved along 12 sorption-desorption cycles in a TG apparatus.**

The 15 (Na, Li, K)-MgO sorbent exhibited a sorption/ desorption profile of intense and stable peaks over the 12 cycles in general. Its MgO conversion fell from 58 % to 34 % right at the 2nd cycle, but it gradually increased until the 6th cycle up to 48 %, from where it progressively decreased until the last cycle, reaching a final MgO conversion of 33 %.

Harada et al. reported carrying capacities of 440 and 310 mg $CO_2$/ g sorbent between the 1st and the 12th cycle for a MgO sorbent doped with 15 % of (Na, Li, K)$NO_3$ [33]. In line with literature, the synthesized 15 (Na, Li, K)-MgO registered a carrying capacity of 460 mg $CO_2$/ g sorbent at the 1st cycle and of 262 mg $CO_2$/ g sorbent at the last cycle.

The promising performance of the 15 (Na, Li, K)-MgO sorbent over multiple sorption/ desorption cycles led to the impregnation of supported MgO-Ca-SG and MgO-Ce-SG sorbents with 15 % of (Na, Li, K)$NO_3$, so their performance over cyclic sorption/ desorption TGA tests could be evaluated. Only 5 cycles were performed (Figure 4-46), due to practical reasons, concerning to the 30 hours that the 12 cycles test would take. Figure 4-47 plots the carrying capacity and the MgO conversion of the 5 cyclic $CO_2$ sorption/ desorption tests of both the 15 (Na, Li, K)-MgO-Ca and 15 (Na, Li, K)-MgO-Ce sorbents.

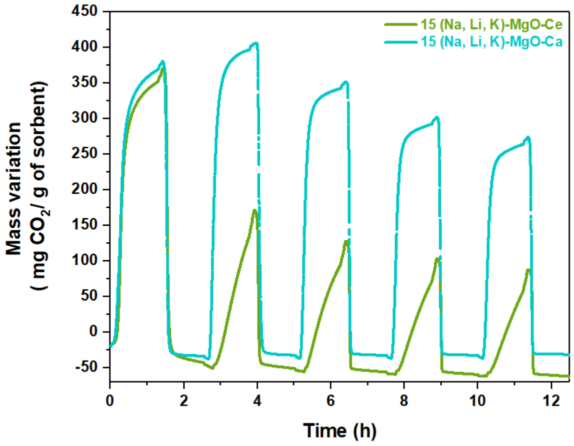

**Figure 4-46 – Profile of sorption (300 °C, 60 min) and desorption (445 °C, 60 min) tests carried out along 5 cycles in a TG (80 ml/ min of $CO_2$) for 15 (Na, Li, K)-MgO-Ca and 15 (Na, Li, K)-MgO-Ce sorbents**

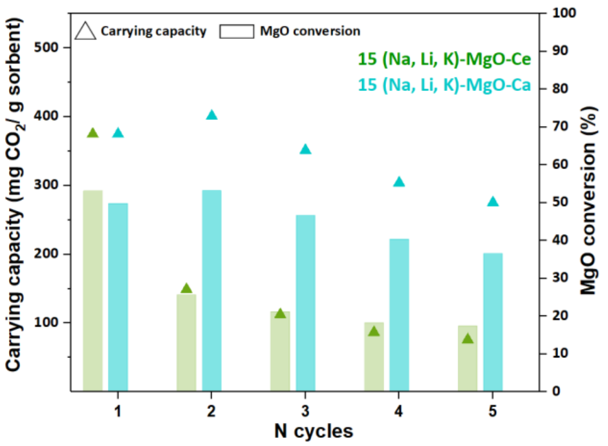

**Figure 4-47 – Carrying capacity (mg $CO_2$/ g sorbent) and MgO conversion (%) of 15 (Na, Li, K)-MgO-Ca and 15 (Na, Li, K)-MgO-Ce sorbents achieved along 5 sorption-desorption cycles in a TG apparatus.**

The 15 (Na, Li, K)-MgO-Ca sorbent exhibited a more promising sorption/ desorption profile along the 5 sorption/ desorption cycles than the 15 (Na, Li, K)-MgO-Ce sorbent, since a higher $CO_2$ carrying capacity was achieved over cycles. Although the 15 (Na, Li, K)-MgO-Ce sorbent registered a reduction of around 50 % of its MgO conversion from cycle 1 to cycle 2, while 15 (Na, Li, K)-MgO-Ca even increases its own, both supported sorbents present quite stable peaks until the end of the test. In fact, that profile is expected from a supported sorbent, since the support inhibits the sintering process and, thus, the sorbent manages to remain stable its multicycle carrying capacity with small loss of $CO_2$ uptake [10].

Quantitively, the MgO-SG-Ca impregnated with 15 % of (Na, Li, K)$NO_3$ obtained a carrying capacity of 375 mg $CO_2$/ g sorbent at the 1st cycle and of 275 mg $CO_2$/ g sorbent at the 5th cycle. Literature reports a Ca-based supported MgO promoted with 20 % of ternary mixture (Na, Li, K)$NO_3$ that varied its carrying capacity from 396 to 330 mg $CO_2$/ g sorbent between the same number of cycles which is in line with the obtained results [35].

Literature reports a Ce-based supported MgO sorbent promoted with 12 % of ternary mixture of (Na, Li, K)$NO_3$ that registered carrying capacities of 340 and 180 mg $CO_2$/ g sorbent between cycles number 1 and 5 [36]. Same sorbent but with an impregnation molar percentage of 17 % managed to achieve 420 mg $CO_2$/ g sorbent at the 1st cycle and 330 mg $CO_2$/ g sorbent at the 5th cycle. The 15 (Na, Li, K)-MgO-Ce sorbent presents an impregnation molar percentage of 15 %, that is, in between those mentioned, and it registers a carrying capacity of 375 mg $CO_2$/ g sorbent, that is, in that interval. Yet, it verified lower carrying capacity at the 5th cycle (76 mg $CO_2$/ g sorbent).

Figure 4-48 shows the variation of the MgO crystallite size of the 15 (Na, Li, K)-MgO-Ca-SG and 15 (Na, Li, K)-MgO-Ce-SG before (fresh) and after (spent) undergoing 5 sorption/ desorption cycles in a TGA.

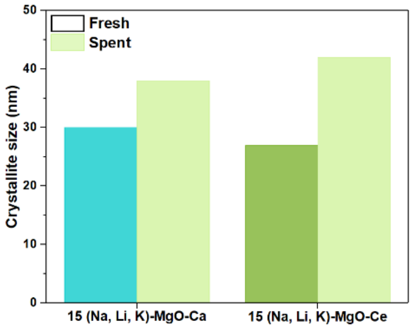

**Figure 4-48 – Crystallite size of 15 (Na, Li, K)-MgO-Ca and 15 (Na, Li, K)-MgO-Ce sorbents before (fresh) and after (spent) 5 sorption/ desorption cycles in a TGA.**

Both 15 (Na, Li K)-MgO-Ca and 15 (Na, Li K)-MgO-Ce sorbents increased its MgO crystallites' size with cycles in 21 % and 36 %, which is expected and mainly attributed to the sintering of the samples. The higher increase of 15 (Na, Li K)-MgO-Ce sorbent is in line with its higher deactivation along the cycles (Figure 4-47). Furthermore, the lower increase of MgO crystallites of 15 (Na, Li K)-MgO-Ca sorbent can possibly be justified by the already mentioned formation of the double salt $CaMg(CO_3)_2$ during $CO_2$ sorption. It is stated in literature that this salt is not significantly affected over multiple cycles, contributing to the stability of the sorbent [35].

### 4.3.2 FIXED-BED REACTOR STUDIES

The performance of the unsupported 15 (Na, Li, K)-MgO and of the supported 15 (Na, Li, K)-MgO-Ca and 15 (Na, Li, K)-MgO-Ce sorbents was evaluated in a fixed-bed reactor over 10 sorption/ desorption cycles with sorption and desorption temperatures fixed at 280 °C (under a flow with 25 % or 100 % of $CO_2$) and at 400 °C (under a flow with 100 % of air), respectively. The experimental conditions were different from those used in the TGA apparatus, because preliminary studies performed with 15 (Na, Li, K)$NO_3$-MgO sorbent demonstrated that the $CO_2$ sorption was improved at temperatures near 280 °C, which, in turn, can be related with the higher heating ramp used in the fixed-bed unit (25 °C/min). Also, due to the low kinetic sorption of MgO-based sorbents and $CO_2$ detector apparatus sensibility, it was not possible to quantify the $CO_2$ uptake during sorption step. Therefore, the desorption step was carried out under air flow and the $CO_2$ uptake calculus was performed as described in section 3.5.2.3. Based on the thermodynamic of $MgCO_3$ equilibrium curve vs $CO_2$ partial pressure (Figure 2.2), the desorption was carried out at 400 °C. The results are plotted in Figure 4-49 and in Figure 4-50 if either a gas stream consisting of 100 % of $CO_2$ or containing 25 % of $CO_2$ + 75 % of air, respectively, was used during sorption reaction.

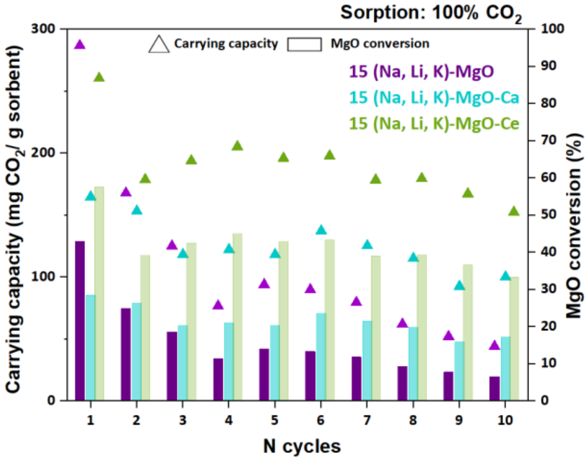

**Figure 4-49 – Carrying capacity (mg $CO_2$/ g sorbent) and MgO conversion (%) achieved along 10 sorption/ desorption cycles in a fixed-bed unit carried out with 15 (Na, Li, K)-MgO, 15 (Na, Li, K)-MgO-Ca and 15 (Na, Li, K)-MgO-Ce sorbents using the following conditions: sorption with 100 % $CO_2$ at 280 °C and desorption with 100 % air at 400 °C.**

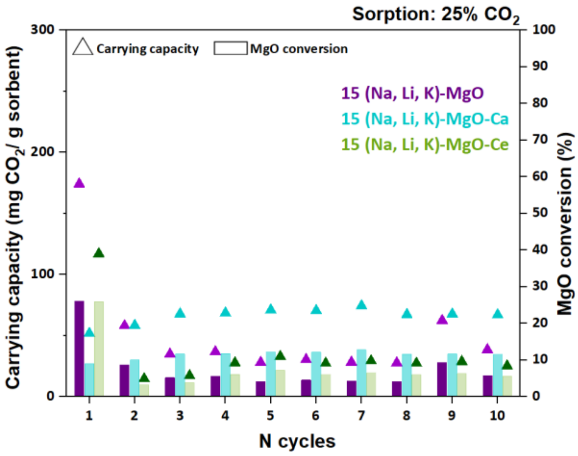

**Figure 4-50 – Carrying capacity (mg $CO_2$/ g sorbent) and MgO conversion (%) achieved along 10 sorption/ desorption cycles in a fixed-bed unit carried out with 15 (Na, Li, K)-MgO, 15 (Na, Li, K)-MgO-Ca and 15 (Na, Li, K)-MgO-Ce sorbents using the following conditions: sorption with 25 % $CO_2$ at 280 °C and desorption with 100 % air at 400 °C.**

A general comparison of Figure 4-49 and Figure 4-50 shows that the analyzed set of sorbents obtained both higher values of carrying capacity and percentages of MgO conversion under sorption atmosphere of 100 % $CO_2$, as expected. $CO_2$ concentration functions as a driving force for the diffusion and sorption of $CO_2$ molecules at the sorption step, so higher $CO_2$ concentrations means higher contact between the sorbent and $CO_2$ [10].

Focusing on Figure 4-49, unsupported MgO sorbent performed worse than any of the supported MgO sorbents, concerning to $CO_2$ uptake, thus, it presents the lowest MgO conversion values of the set as the number of cycles increases, although it registered a higher MgO conversion at the 1st cycle than the 15 (Na, Li, K)-MgO-Ca sorbent. This behavior was expected, and it is the result of the non-addition of support. It started with an abrupt decreasing tendency from the 1st to the 4th cycle, with a small regain at the 5th cycle that is followed by a gradual decreasing of the MgO conversion until the 10th cycle. The Ca supported exhibits regains at the 4th, 6th and 10th cycles, showing higher values of MgO conversion than those of the unsupported sorbent. It was the Ce-based supported sorbent that demonstrated to have the highest values of MgO conversion under 100 % of $CO_2$ sorption atmosphere, which is in disagreement with the result obtained in the TG test. However, the use of a different desorption atmosphere and temperature can justify the lower deactivation of sorbent when tested in the fixed-bed, since it can affect both processes of sintering and nitrates segregation, as mentioned above. About stability, both supported sorbents presented similar values of deactivation, i.e., 40 % and 42 % for 15 (Na, Li, K)-MgO-Ca and 15 (Na, Li, K)-MgO-Ce, respectively, while the unsupported sorbent deactivation was 85 %.

The 15 (Na, Li, K)-MgO sorbent registered a carrying capacity of 287 mg $CO_2$/ g sorbent at the 1st cycle and of 44 mg $CO_2$/ g sorbent at the 5th cycle, considering the sorption atmosphere of 100 % $CO_2$. Literature reports an MgO sorbent impregnated with (Li, K)$NO_3$ + ($Na_2$,$K_2$)$CO_3$ that registered higher values of carrying capacity of 410 and 325 mg $CO_2$/ g sorbent between 1st and 8th, yet it must take into account that test was conducted under different sorption and desorption conditions and in a packed bed reactor [34]. Moreover, it is described in literature that packed bed reactors may be able to overcome limitations associated to fixed-bed configuration, namely, elevated pressure drops, gradients of temperature and both mass and heat transfers' limitation problems. In fact, conventional fixed-bed reactors are believed not to deliver the full potential associated to $CO_2$ uptake technologies. Conversely, packed configuration can be able to reduce the pressure drop by keeping an elevated contacting area between the gas and the solid [77].

In addition, it is interesting to note that each sorbent registered lower carrying capacities for the tests carried in the fixed-bed reactor than those in the TGA. It can be due to the already mentioned limitations associated with fixed-bed configuration.

Under an atmosphere consisting of 25 % of $CO_2$ + 75 % of air (Figure 4-50), it was the Ca-based supported sorbent that presented the highest MgO conversion values. Moreover, it was the only sorbent that managed to increase its $CO_2$ uptake during the test, which can be due to the formation of the double salt $CaMg(CO_3)_2$, through the dissolution of carbonates, contributing for the $CO_2$ uptake [10,29]. Therefore, between the 1st and 10th cycle the MgO conversion of 15 (Na, Li, K)-MgO-Ca increased 28 %, while the 15 (Na, Li K)-MgO and 15 (Na, Li K)-MgO-Ce sorbents deactivation was 78 % and 79 %, respectively. Hence, the 15 (Na, Li K)-MgO-Ca was considered the sorbent best performing under a sorption atmosphere of 25 % of $CO_2$, which make it the most promising sorbent under realistic industrial applications, where concentrations of $CO_2$ lower than 25 % in flue gases are often.

Figure 4-51 plots the variation of the MgO crystallite size of the 15 (Na, Li, K)-MgO, 15 (Na, Li, K)-MgO-Ca-SG and 15 (Na, Li, K)-MgO-Ce-SG before (fresh sorbent) and after undergoing 10 sorption/ desorption cycles in a fixed-bed reactor under two different sorption atmospheres, namely, 25 % of $CO_2$ and 100 % of $CO_2$.

Considering as reference the crystallite size of fresh sorbents, the MgO crystallite size of the unpromoted 15 (Na, Li, K)-MgO sorbent was the less stable along the cycles since their size increased 77 % and 73 % under a sorption atmosphere of 25 % and 100 % of $CO_2$, respectively. The lower stability of the unpromoted sorbent's crystallites is in line with its higher deactivation along cycles. The 15 (Na, Li, K)-MgO-Ca sorbent registered an increase of the MgO crystallite size of 47 % and 33 % under a sorption atmosphere of 25 % of $CO_2$ and of 100 % of $CO_2$, respectively. In the other hand, the 15 (Na, Li, K)-MgO-Ce sorbent is the presenting more stable crystallites since an increase of 22 % was achieved under an atmosphere of 25 % of $CO_2$, and it remained stable under a sorption of 100 % of $CO_2$.

Figure 4-51 also stands out that the MgO crystallites maintain its sized a little more stable under a sorption atmosphere of 100% of $CO_2$, which can be related with the obtained higher conversions. A possible explanation for this can be the lower thermal conductivity of $CO_2$ comparatively with air, i.e., 37.8 [78] vs 43.2 [79] mW/ mK at 280 °C, which can contribute for the lower sintering of crystallites.

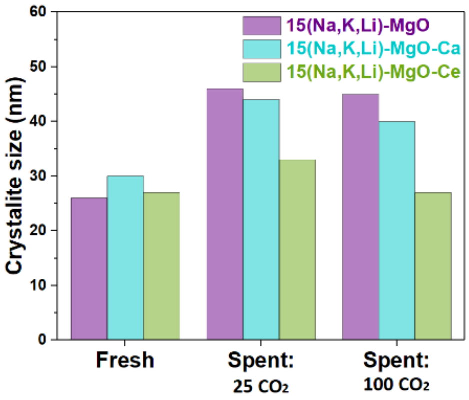

**Figure 4-51 – Crystallite size of 15 (Na, Li, K)-MgO, 15 (Na, Li, K)-MgO-Ca and 15 (Na, Li, K)-MgO-Ce sorbents before (fresh) and after (spent) 10 sorption/ desorption cycles in a fixed-bed unit, under a sorption atmosphere of 25 % of $CO_2$ or 100 % of $CO_2$.**

The $N_2$ sorption technique was used to assess the textural properties of the unsupported 15 (Na, Li, K)-MgO-SG as well as of both the supported 15 (Na, Li, K)-MgO-Ca and 15 (Na, Li, K)-MgO-Ce sorbents after undergoing 10 sorption/ desorption cycles in the fixed-bed unit. Figure 4-52 (a), (b) and (c) shows the $N_2$ sorption isotherms; (d), (e) and (f) the specific surface area ($S_{BET}$) and total pore volume ($V_p$); and (g), (h) and (i) the pore size distribution (PSD) estimated by the BJH desorption of the 15 (Na, Li, K)-MgO, 15 (Na, Li, K)-MgO-Ca and 15 (Na, Li, K)-MgO-Ce, respectively, as fresh and spent sorbents.

$N_2$ sorption/ desorption isotherms of the fresh sorbents were prior classified as type II with a discreet hysteresis, that was subsequently proved by the presence of a small share of mesoporous by the corresponding PSD. However, the hysteresis became narrower for the 15 (Na, Li, K)-MgO and 15 (Na, Li, K)-MgO-Ca sorbents under a sorption atmosphere of 25 % of $CO_2$ and disappeared under a sorption atmosphere of 100 % of $CO_2$. The 15 (Na, Li, K)-MgO-Ce sorbent remained its hysteresis quite stable.

The analyzed sorbents registered a decrease in the $S_{BET}$ from fresh to spent on both atmospheres. Generally, the total pore volume follows the same tendency. Thus, promoted MgO sorbents loose surface area and pore volume during cycling. In addition, the unsupported 15 (Na, Li, K)-MgO shows the highest reduction of $S_{BET}$, suggesting that the addition of support helps the sorbent to keep its surface area closer to that as fresh sorbent. The $S_{BET}$ reduction was always higher for sorbents whose sorption was performed under 100 % of $CO_2$ than with 25 % of $CO_2$, namely, 76 % and 80 % for 15 (Na, Li, K)-MgO, 30% and 43% for 15 (Na, Li, K)-MgO-Ca, 10 % and 38 % for15 (Na, Li, K)-MgO-Ce.

The PSD of the 15 (Na, Li, K)-MgO and of the 15 (Na, Li, K)-MgO-Ca are very similar and are in accordance with the evidence given by the corresponding $N_2$ isotherms. Both have a PSD highly concentrated in the macropores zone with a decreasing pore volume from fresh to spent under 25 % of $CO_2$ and, finally, to spent under 100 % of $CO_2$. The 15 (Na, Li, K)-MgO-Ce sorbent presents a PSD with higher share of mesoporous, in line with the presence of hysteresis.

Looking for the sorption atmosphere effect on the sorbent's crystallite size and $S_{BET}$, it can be stated that a higher $CO_2$ concentration during the sorption step contributes for a lower increase of the crystallite size, i.e., lower sintering of MgO crystallite. Yet, lower $S_{BET}$ values were achieved for these sorbents. This result confirms that sintering is not the only responsible for the reduction of the surface area and deactivation along cycles, and factors like the nitrates' segregation can also contribute for the $S_{BET}$ reduction. Further studies need to be conducted for a better understanding of the sorption atmosphere's effect on the sorbents.

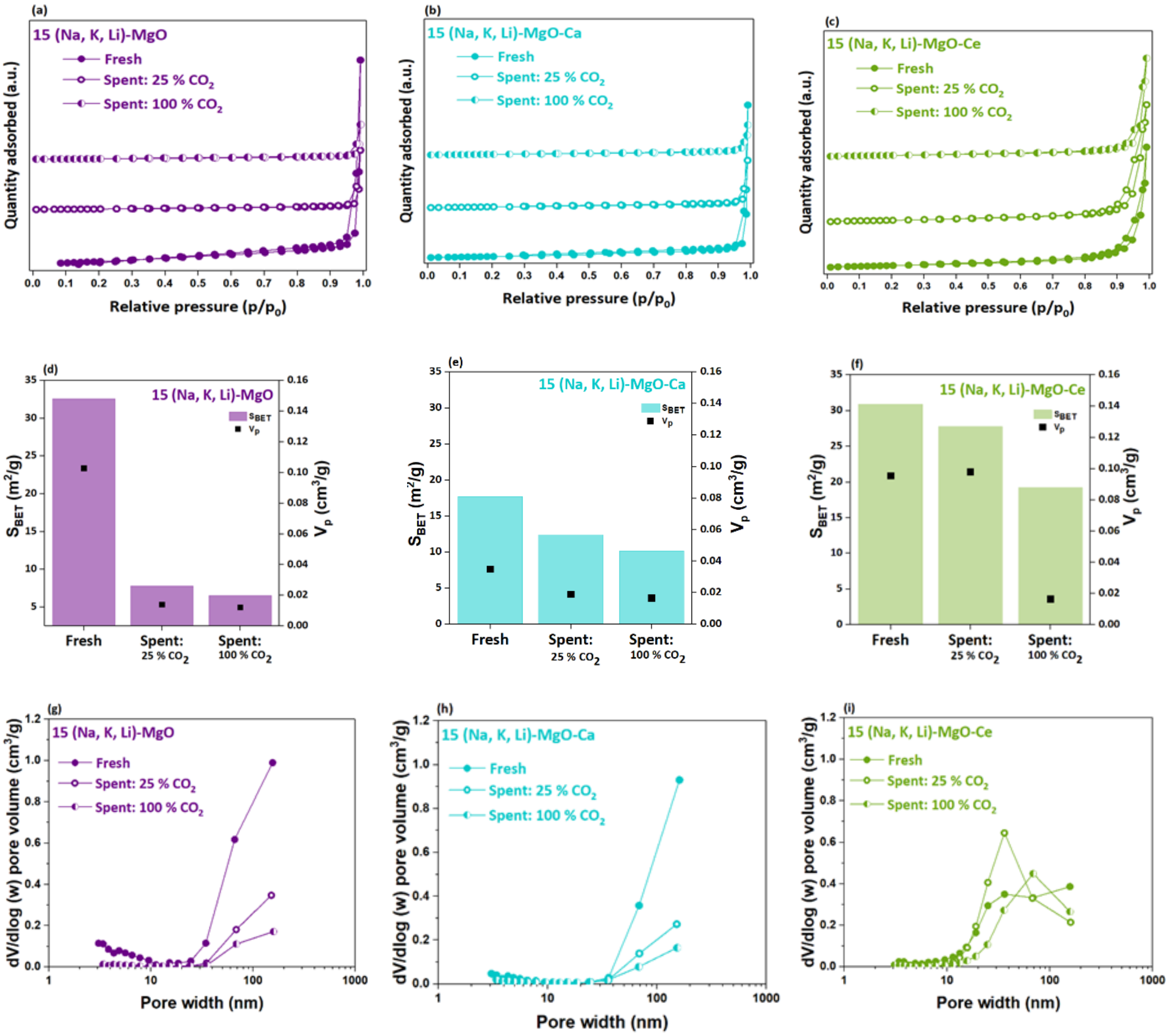

**Figure 4-52 – Textural properties of fresh and spent sorbents, 15 (Na, Li, K)-MgO, 15 (Na, Li, K)-MgO-Ca and 15 (Na, Li, K)-MgO-Ce, tested along 10 cycles in a fixed-bed unit, under a sorption atmosphere of 25 % of $CO_2$ or 100 % of $CO_2$: (a, b, c) $N_2$ sorption isotherms, (d, e, f) specific surface area ($S_{BET}$) and total pore volume ($V_p$), (g, h, i) pore size distribution (PSD) estimated by the BJH desorption.**

To evaluate the sorbents 3D morphology's evolution after undergoing 10 sorption/ desorption cycles in the fixed-bed unit (sorption atmosphere: 100 % of $CO_2$), as well as the distribution of the support (Ca and Ce-based) and of the AMS along the particles, it was carried the SEM analysis. Figure 4-53 shows the SEM images of 15 (Na, Li, K)-MgO, 15 (Na, Li, K)-MgO-Ca and 15 (Na, Li, K)-MgO-Ce of sorbents and Figure 4-54 shows the identification of the main elements present in specific zones of these samples.

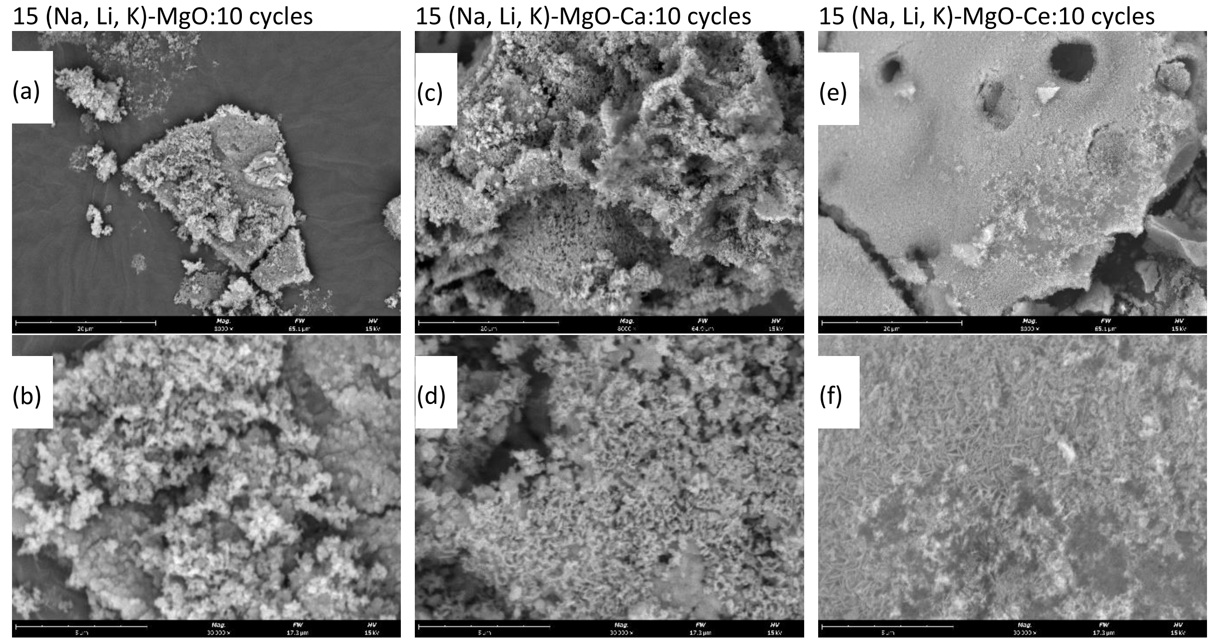

**Figure 4-53 – SEM images of (a and b) 15 (Na, K, Li)-MgO, (c and d) 15-(Na, K, Li) MgO-Ca and (e and f) 15 (Na, K, Li)-MgO-Ce sorbents after 10 sorption/ desorption cycles under a sorption atmosphere 100 % of $CO_2$ in a fixed-bed unit. (a, c, e: scale: 20_µm and magnification: x 8 000; b, d, f: scale: 5_µm and magnification: x 30 000).**

SEM images (a) and (b) of Figure 4-53 looks similar to the fresh 15 (Na, Li, K)-MgO sorbent (Figure 4-16 (a) and (b)). SEM images (c) and especially (d) of Figure 4-53 exhibit clear effects of sintering, such as aggravated grain agglomeration in the external surface of the 15 (Na, Li, K)-MgO-Ca sorbent, after undergoing 10 sorption/ desorption cycles under a sorption atmosphere of 100 % $CO_2$. SEM images (e) and (f) of Figure 4-53 show a more intense presence of crystals as well as a slightly grain agglomeration in the outer surface of the 15 (Na, Li, K)-MgO-Ce sorbent, after undergoing 10 sorption/ desorption cycles. Figure 4-54 shows the mapping of the previous sorbents after 10 sorption/desorption cycles, that allows to assess the elements' distributions in the sorbent.

As explained above (section 4.1.2), the evaluation of the elements mapping should be focused only over the particles surface. Calcium and cerium appear to be well-distributed along the MgO particles since no segregation was observed. In supported particles, the potassium distribution along the surface looks to be homogeneous. However, for the unsupported sorbent, an intense signal is observed over the particle (black circles), that can be justified by the occurrence of some sintering associated to the $KNO_3$, as already mentioned. The sodium looks to be more concentrated in some zones of the unsupported sorbent than in supported sorbents. In fact, as observed for the fresh sorbents, the Na was not detectable in the 15 (Na, Li, K)-MgO-Ca sample, and its signal is very smooth for the 15 (Na, Li, K)-MgO-Ce sorbent, which can be related to the higher dispersion of Na in supported samples, that, in turn, reduces the emitted intensity.

Summarizing, the 15 (Na, Li, K)-MgO sorbent is associated with the highest degree of alkali metal salts aggregation/sintering, which can justify its lower performance in the fixed-bed unit. In the other hand, the Ca and Ce addition contributes for a higher dispersion of AMS on the sorbent, improving their carrying capacity, and additionally, the 15 (Na, K, Li)-MgO-Ce sorbent benefits also from its lower particles size.

(a)15 (Na, Li, K)-MgO: 10 cycles (e)15 (Na, Li, K)-MgO-Ca: 10 cycles (i) 15 (Na, Li, K)-MgO-Ce:10 cycles

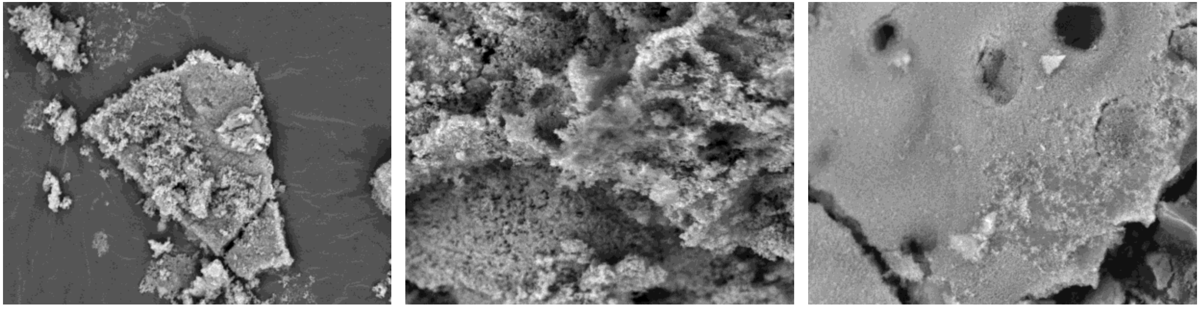

(b) Magnesium (f) Magnesium (j) Magnesium

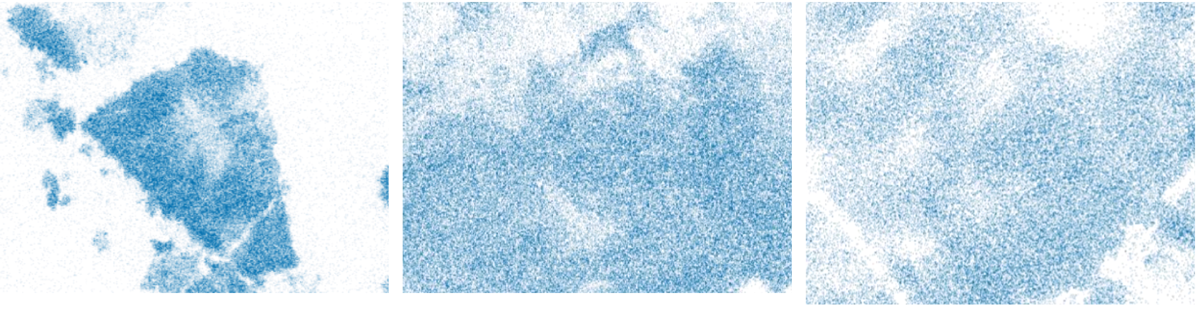

(g) Calcium (l) Cerium

Unsupported sorbent

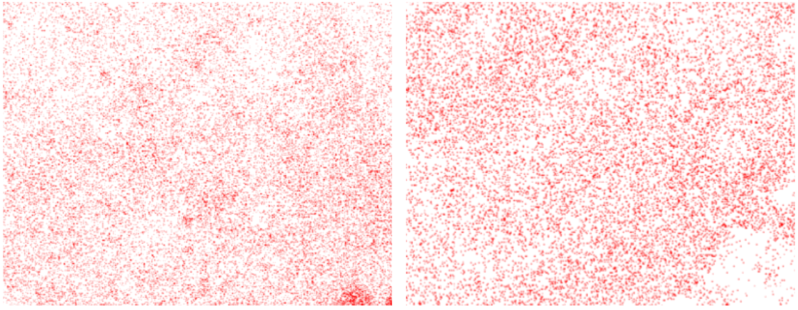

(c) Potassium (h) Potassium (m) Potassium

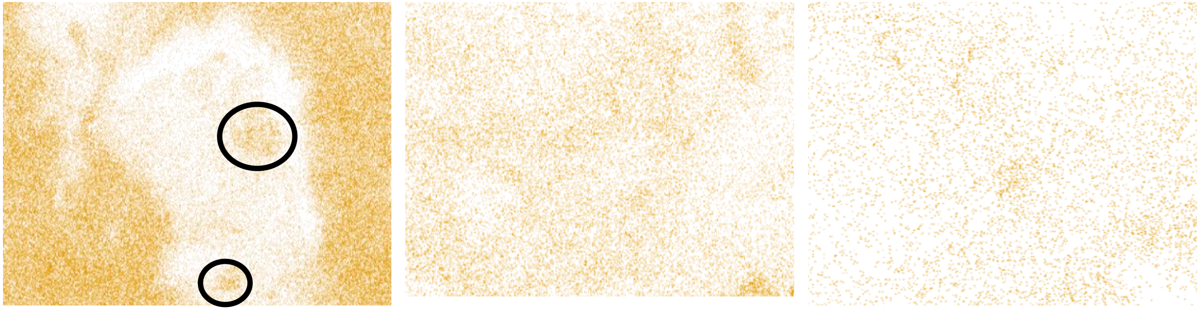

(d) Sodium

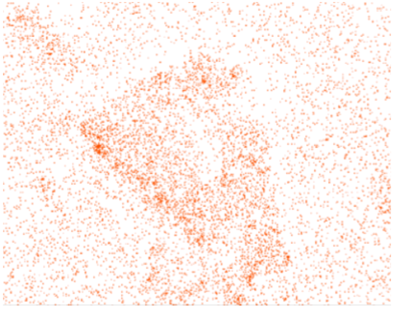

Not detected

(n) Sodium

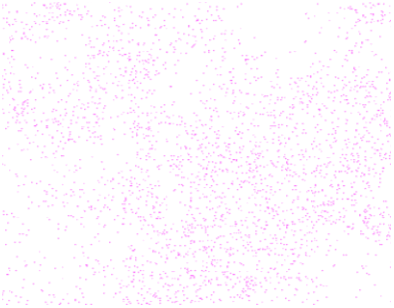

**Figure 4-54 – Mapping of SEM images: (a, b, c, d) 15(Na, Li, K)-MgO; (e, f, g , h) 15 (Na, Li, K) MgO-Ca, and (i, j, l, m, n) 15 (Na, Li, K)-MgO-Ce (scale: 20_µm and magnification: x 8 000).**

# 5 CONCLUSIONS

CCS technologies are considered one of the most viable solutions to mitigate global $CO_2$ emissions. MgO-based sorbents are considered promising materials, due to their high theoretical $CO_2$ capture capacity, small regeneration energy, wide availability and low price. Yet, they also exhibit experimental poor $CO_2$ capture capacity coupled with both low kinetics and thermal stability. This thesis evaluated the efficiency of the sol-gel method in the synthesis of mesoporous MgO sorbents; and the potential of both the addition of supports (Ca and Ce-based) and the AMS doping on the enhancement of the $CO_2$ uptake of MgO-based sorbents.

The synthesis of pure MgO-based sorbents was confirmed by the presence of the MgO's characteristic peaks in the corresponding diffractograms. Moreover, using the sol-gel method it was possible to decrease the crystallite size of MgO particles. The $N_2$ sorption's results agreed with the XRD characterization, with smaller MgO crystallites corresponding to higher sorbents' surface areas. In addition, $N_2$ sorption isotherms and PSD distribution showed that all the synthesized MgO-based sorbents were constituted of both meso and macroporous. Furthermore, SEM images showed that the addition of the Ce-based support changed the sorbent's internal structure with the formation of numerous spherical empty holes of different diameters. Also, the element mapping of both supported sorbents proved their distribution's homogeneity. Summarizing, the sol-gel method was proved to be efficient, as homogeneous and nanosized MgO-based sorbents were produced.

The successful synthesis of AMS doped MgO-based sorbents using the wet-impregnation method was confirmed by the presence of the AMS salts' characteristic peaks in the corresponding diffractograms. All the AMS impregnated samples suffered an increase of the MgO crystallites' size. Moreover, the ternary alkali AMS accentuated that size increase, regardless the AMS impregnation's molar percentage. In addition, diffractograms at different stages of the 30 Na-MgO sorbent showed that increase of the crystalite size was also potenciated by the sorption/ desorption cycles. Also, the use of Ca and Ce-based supports inhibited the increase of the crystallite size. The $N_2$ sorption's results agreed with the XRD characterization. The 15 (Na, Li, K)-MgO, 15 (Na, Li, K)-MgO-Ca and 15 (Na, Li, K)-MgO-Ce sorbents registered smaller $S_{BET}$ in comparison with those of the respective undoped sorbents. The $N_2$ isotherms and PSD distributions revealed an increase of the macroporous share in their constitution. SEM images of the unsupported 15 (Na, Li, K)-MgO sorbent showed the presence of structures resulting from the $KNO_3$ melting, while those of the supported sorbents don't. The element mapping of the unsupported sorbent showed worse homogeneity distribution, with sintered zones of potassium nitrate and more concentrated in sodium nitrate zones too. Conversely, both supported sorbents were well-distributed. Hence, the addition of Ca and Ce-based supports was concluded to prevent the agglomeration and sintering to occur.

The thermal decomposition of mono and ternary alkali nitrate salts demonstrated that the type of atmosphere affects both the extent of the decomposition and the loss of mass, being higher under 100 % of air than under 100 % of $CO_2$. The ternary mixture of (Na, Li, K)$NO_3$ offered wider working temperature ranges to operate in, regardless the atmosphere used.

The $CO_2$ uptake of the 30 Na-MgO sorbent remained stable under 300 °C, 325 °C and 350 °C for 60 or 90 minutes. The desorption efficiency increased with the increasing temperatures of 420 °C, 430 °C, 435 °C, 440 °C and 445 °C. Thus, the selected conditions were sorption temperature of 300 °C for the time interval of 60 minutes and desorption temperature of 445 °C for 60 minutes.

Using the defined sorption/ desorption operation conditions, the preliminary $CO_2$ uptake of MgO-based sorbents was assessed in a TGA over a temperature window from 20 °C to 500 °C under an atmosphere of 100 % of $CO_2$. Unpromoted MgO-based sorbents registered significant small $CO_2$ uptakes than promoted ones (36 mg $CO_2$/ g sorbent against 239 mg $CO_2$/ g sorbent). Thus, it was proved that the AMS impregnation enhances the $CO_2$ sorption capacity of MgO-based sorbents. In addition, it was verified that the AMS doping increased the MgO crystallites' size after undergoing the TGA test, with the increase being higher when the impregnation uses the single salt than the ternary mixture. Regarding to the supported sorbents, the same evidence was found. Moreover, undoped supported MgO-based sorbents managed to achieve higher $CO_2$ uptakes than the undoped unsupported ones.

The carrying capacity along the sorption/desorption cycles was assessed in a TGA under 100 % of $CO_2$. The mono alkali impregnated sorbents exhibited significantly worse performances than the ternary alkali impregnated sorbents, with the formers demonstrating to have higher $CO_2$ uptake's losses over the 5 sorption/ desorption cycles. Overall, the 15 (Na, Li, K)-MgO sorbent was considered to have the best performance, varying its carrying capacity from 460 to 330 mg $CO_2$/ g sorbent between the 1st and the 5th cycle. Moreover, the supported 15 (Na, Li, K)-MgO-Ca and 15 (Na, Li, K)-MgO-Ce sorbents both registered a carrying capacity of 375 mg $CO_2$/ g sorbent at the 1st and of 275 and 76 mg $CO_2$/ at the 5th cycle, respectively. In accordance, the increase of the MgO crystallite's size of the 15 (Na, Li, K)-MgO-Ce was higher than that of the 15 (Na, Li, K)-MgO-Ca.

Finally, the 15 (Na, Li, K)-MgO, 15 (Na, Li, K)-MgO-Ca and the 15 (Na, Li, K)-MgO-Ce sorbents achieved higher values of carrying capacity over 10 sorption/ desorption cycles carried out under sorption atmosphere of 100 % of $CO_2$ than under 25 % of $CO_2$ in the fixed-bed reactor. The 15 (Na, Li, K)-MgO-Ce sorbent had the best performance under sorption atmosphere of 100 % of $CO_2$, varying its carrying capacity from 260 to 152 mg $CO_2$/ g sorbent between the 1st and the 10th cycle. The 15 (Na, Li, K)-MgO-Ca sorbent had the best performance under sorption atmosphere of 25 % of $CO_2$, varying its carrying capacity from 52 to 67 mg $CO_2$/ g sorbent between the 1st and the 10th cycle. The improved $CO_2$ carrying capacity of supported sorbents can be explained by the reduction of nitrates' sintering and segregation, since their dispersion on the sorbent looks to be enhanced, and by the improvement of sorbents' properties, like surface area.

Summarizing, the modified MgO-based sorbents are promising materials for $CO_2$ capture, whose performance can be enhanced by the AMS doping and by the addition of Ca or Ce-based supports.

# 6 FUTURE WORK

Future work in the scope of this thesis should considerate:

- To explore nano-MgO preparation techniques, such as spray-drying;
- To explore different ratios of porous supports and different supports (ex. $TiO_2$);
- To optimize both sorption and desorption temperatures and time intervals using different types and fractions of AMS and supports;
- To assess the effect of the addition of steam in the $CO_2$ carrying capacity of MgO-based sorbents;
- To perform multicyclic sorption/ desorption experiments under more realistic conditions from an industrial point of view, such as, sorption atmosphere ranging from 15 to 25 % of $CO_2$.

In addition, it was verified there is big a lack of technical and economical assessment studies in literature with relation to CCS technologies using MgO-based sorbents that doesn't align with the urgency of mitigating $CO_2$ emissions. Although the performance of MgO-based sorbents has already been quite investigated in TGAs, there are still few studies using reactors. So, considering a broader scope for MgO-based sorbents' applications, here stands out important aspects that need to be considered in a near future:

- Concerning to the technical aspect, experimental tests in laboratory and pre-pilot scale projects should focus on perform sorption/ desorption cyclic tests in reactors. Multistage fluidized bed and structured reactors are appointed as promising configurations. Moreover, these tests have to occur under realistic conditions that assess the MgO-based sorbents' performance according to the target application, like SEWGS. Finally, sorption/ desorption tests need to be run for higher numbers of cycles (hundreds or thousands).
- Regarding to the economical aspect, the integration of a MgO-based looping system in a CCS technology will only be implemented in industry if it is cost-effective. The development of a life cycle assessment (LCA) should be taken into account when estimating both resources consumption and environmental impact.

# 7 REFERENCES

[1] International Energy Agency, “World Energy Outlook 2020,” 2021. https://www.iea.org/reports/world-energy-outlook-2020?mode=overview#executive-summary (accessed May 13, 2021).

[2] M. T. Masson-Delmotte, V., P. Zhai, H.-O. Pörtner, D. Roberts, J. Skea, P.R. Shukla, A. Pirani, W. Moufouma-Okia, C. Péan, R. Pidcock, S. Connors, J.B.R. Matthews, Y. Chen, X. Zhou, M.I. Gomis, E. Lonnoy, T. Maycock, “Global Warming of 1.5°C. An IPCC Special Report on the impacts of global warming of 1.5°C above pre-industrial levels and related global greenhouse gas emission pathways, in the context of strengthening the global response to the threat of climate change,” 2018. doi: 10.1038/291285a0.

[3] A. F. P. Stéphanie Bouckaert and U. R. and B. W. Christophe McGlade, “Net Zero by 2050 A Roadmap for the Global Energy Sector,” 2021.

[4] BP, “Statistical Review of World Energy,” *Stat. Rev. World Energy*, vol. 67, pp. 1–56, 2020, [Online]. Available: bp.com/statisticalreview.

[5] M. Schulz and D. Kourkoulas, “Regulation (EU) No 517/2014 of the European Parliament and of the Council of 16 April 2014 on fluorinated greenhouse gases and repealing Regulation (EC) No 842/2006,” 2014. [Online]. Available: http://eur-lex.europa.eu/eli/reg/2014/517/oj.

[6] “Global Warming Potentials (IPCC Second Assessment Report).” https://unfccc.int/process/transparency-and-reporting/greenhouse-gas-data/greenhouse-gas-data-unfccc/global-warming-potentials (accessed May 15, 2021).

[7] IPCC, “Assessment Report 6 Climate Change 2021: The Physical Science Basis,” 2021, [Online]. Available: https://www.ipcc.ch/report/ar6/wg1/.

[8] International Energy Agency, “Global Energy Review 2021,” *Glob. Energy Rev. 2020*, pp. 1–36, 2021, [Online]. Available: https://iea.blob.core.windows.net/assets/d0031107-401d-4a2f-a48b-9eed19457335/GlobalEnergyReview2021.pdf.

[9] “Paris Agreement on climate change - Consilium.” https://www.consilium.europa.eu/en/policies/climate-change/paris-agreement/ (accessed May 13, 2021).

[10] Y. Hu, Y. Guo, J. Sun, H. Li, and W. Liu, “Progress in MgO sorbents for cyclic CO2 capture: A comprehensive review,” *J. Mater. Chem. A*, vol. 7, no. 35, pp. 20103–20120, 2019, doi: 10.1039/c9ta06930e.

[11] A. Page, Brad; Turan, Guloren; Zapantis, “Global Status of CCS,” 2020.

[12] W. Wang, Qiang; Gao, “MgO-based Intermediate-temperature CO2 Adsorbents,” in *Pre-combustion Carbon Dioxide Capture Materials*, 1st ed., Q. Wang, Ed. Beijing: Royal Society of Chemistry, 2018.

[13] P. Breeze, “Coal-fired Generation- CHAPTER 7 Carbon Capture and Storage,” 2015, doi: 10.1016/B978-0-12-804006-5.00013-7.

[14] K. Zhang, “Development of Molten Salt Promoted Metal Oxide based Absorbents for CO2 Separation,” 2014.

[15] B. J. P. Buhre, L. K. Elliott, C. D. Sheng, R. P. Gupta, and T. F. Wall, “Oxy-fuel combustion technology for coal-fired power generation,” *Prog. Energy Combust. Sci.*, vol. 31, no. 4, pp. 283–307, 2005, doi: 10.1016/j.pecs.2005.07.001.

[16] UNECE, “Carbon Capture, Use And Storage (CCUS),” 2021, [Online]. Available: https://shop.un.org.

[17] I. Ghiat and T. Al-Ansari, “A review of carbon capture and utilisation as a CO2abatement opportunity within the EWF nexus,” *J. CO2 Util.*, vol. 45, no. December 2020, p. 101432, 2021, doi: 10.1016/j.jcou.2020.101432.

[18] K. Wang, Y. Zhao, P. T. Clough, P. Zhao, and E. J. Anthony, “Structural and kinetic analysis of CO2 sorption

on NaNO2-promoted MgO at moderate temperatures," *Chem. Eng. J.*, vol. 372, no. April, pp. 886–895, 2019, doi: 10.1016/j.cej.2019.04.080.

[19] H. Zhao and M. Zhang, "Research progress of CaO-based absorbents prepared from different calcium sources," *IOP Conf. Ser. Earth Environ. Sci.*, vol. 474, no. 5, 2020, doi: 10.1088/1755-1315/474/5/052058.

[20] Z. Skoufa, A. Antzara, E. Heracleous, and A. A. Lemonidou, "Evaluating the activity and stability of CaO-based sorbents for post-combustion CO2 capture in fixed-bed reactor experiments," *Energy Procedia*, vol. 86, pp. 171–180, 2016, doi: 10.1016/j.egypro.2016.01.018.

[21] J. Fagerlund, J. Highfield, and R. Zevenhoven, "Kinetics studies on wet and dry gas-solid carbonation of MgO and Mg(OH) 2 for CO 2 sequestration," *RSC Adv.*, vol. 2, no. 27, pp. 10380–10393, 2012, doi: 10.1039/c2ra21428h.

[22] G. Song, X. Zhu, R. Chen, Q. Liao, Y. D. Ding, and L. Chen, "An investigation of CO2 adsorption kinetics on porous magnesium oxide," *Chem. Eng. J.*, vol. 283, pp. 175–183, 2016, doi: 10.1016/j.cej.2015.07.055.

[23] Y. Guo *et al.*, "Nanostructured MgO Sorbents Derived from Organometallic Magnesium Precursors for Post-combustion CO2 Capture," *Energy and Fuels*, vol. 32, no. 6, pp. 6910–6917, 2018, doi: 10.1021/acs.energyfuels.8b00866.

[24] A. Hanif, S. Dasgupta, and A. Nanoti, "Facile Synthesis of High-Surface-Area Mesoporous MgO with Excellent High-Temperature CO2 Adsorption Potential," *Ind. Eng. Chem. Res.*, vol. 55, no. 29, pp. 8070–8078, 2016, doi: 10.1021/acs.iecr.6b00647.

[25] A. Dal Pozzo, A. Armutlulu, M. Rekhtina, P. M. Abdala, and C. R. Müller, "CO2 Uptake and Cyclic Stability of MgO-Based CO2 Sorbents Promoted with Alkali Metal Nitrates and Their Eutectic Mixtures," *ACS Appl. Energy Mater.*, vol. 2, no. 2, pp. 1295–1307, 2019, doi: 10.1021/acsaem.8b01852.

[26] X. Yang, L. Zhao, Y. Liu, Z. Sun, and Y. Xiao, "Carbonation performance of NaNO3 modified MgO sorbents," *Ind. Eng. Chem. Res.*, vol. 56, no. 1, pp. 342–350, 2017, doi: 10.1021/acs.iecr.6b03909.

[27] K. Zhang *et al.*, "Phase Transfer-Catalyzed Fast CO2 Absorption by MgO-Based Absorbents with High Cycling Capacity," *Adv. Mater. Interfaces*, vol. 1, no. 3, pp. 1–6, 2014, doi: 10.1002/admi.201400030.

[28] C. H. Lee, S. Mun, and K. B. Lee, "Characteristics of Na-Mg double salt for high-temperature CO2 sorption," *Chem. Eng. J.*, vol. 258, pp. 367–373, 2014, doi: 10.1016/j.cej.2014.07.082.

[29] K. Zhang, X. S. Li, H. Chen, P. Singh, and D. L. King, "Molten Salt Promoting Effect in Double Salt CO2 Absorbents," *J. Phys. Chem. C*, vol. 120, no. 2, pp. 1089–1096, 2016, doi: 10.1021/acs.jpcc.5b10729.

[30] X. Zhao, G. Ji, W. Liu, X. He, E. J. Anthony, and M. Zhao, "Mesoporous MgO promoted with NaNO3/NaNO2 for rapid and high-capacity CO2 capture at moderate temperatures," *Chem. Eng. J.*, vol. 332, pp. 216–226, 2018, doi: 10.1016/j.cej.2017.09.068.

[31] S. J. Park, Y. Kim, and C. W. Jones, "NaNO3-Promoted Mesoporous MgO for High-Capacity CO2 Capture from Simulated Flue Gas with Isothermal Regeneration," *ChemSusChem*, vol. 13, no. 11, pp. 2988–2995, 2020, doi: 10.1002/cssc.202000259.

[32] W. Gao, T. Zhou, Y. Gao, Q. Wang, and W. Lin, "Study on MNO 3 /NO 2 (M = Li, Na, and K)/MgO Composites for Intermediate-Temperature CO 2 Capture," *Energy and Fuels*, vol. 33, no. 3, pp. 1704–1712, 2019, doi: 10.1021/acs.energyfuels.8b02749.

[33] T. Harada and T. A. Hatton, "Colloidal Nanoclusters of MgO Coated with Alkali Metal Nitrates/Nitrites for Rapid, High Capacity CO2 Capture at Moderate Temperature," *Chem. Mater.*, vol. 27, no. 23, pp. 8153–8161, 2015, doi: 10.1021/acs.chemmater.5b03904.

[34] J. Chen, L. Duan, F. Donat, and C. R. Müller, "Assessment of the Effect of Process Conditions and Material Characteristics of Alkali Metal Salt Promoted MgO-Based Sorbents on Their CO2Capture Performance," *ACS Sustain. Chem. Eng.*, vol. 9, no. 19, pp. 6659–6672, 2021, doi: 10.1021/acssuschemeng.1c00262.

[35] T. Papalas, A. N. Antzaras, and A. A. Lemonidou, “Magnesite-derived MgO promoted with molten salts and limestone as highly-efficient CO2 sorbent,” *J. CO2 Util.*, vol. 53, no. June, p. 101725, 2021, doi: 10.1016/j.jcou.2021.101725.

[36] S. Jin, K. J. Ko, and C. H. Lee, “Direct formation of hierarchically porous MgO-based sorbent bead for enhanced CO2 capture at intermediate temperatures,” *Chem. Eng. J.*, vol. 371, no. April, pp. 64–77, 2019, doi: 10.1016/j.cej.2019.04.020.

[37] B. W. Hwang *et al.*, “CO2 capture and regeneration properties of MgO-based sorbents promoted with alkali metal nitrates at high pressure for the sorption enhanced water gas shift process,” *Process Saf. Environ. Prot.*, vol. 116, pp. 219–227, 2018, doi: 10.1016/j.psep.2018.02.008.

[38] S. Zarghami, A. Hassanzadeh, H. Arastoopour, and J. Abbasian, “Effect of Steam on the Reactivity of MgO-Based Sorbents in Precombustion CO2 Capture Processes,” *Ind. Eng. Chem. Res.*, vol. 54, no. 36, pp. 8860–8866, 2015, doi: 10.1021/acs.iecr.5b01175.

[39] Y. Y. Li, X. Y. M. Dong, X. D. Sun, Y. Wang, and J. H. Zhu, “New Solid-Base Cu-MgO for CO2 Capture at 473 K and Removal of Nitrosamine,” *ACS Appl. Mater. Interfaces*, vol. 8, no. 44, pp. 30193–30204, 2016, doi: 10.1021/acsami.6b09927.

[40] W. Gao, T. Zhou, Y. Gao, and Q. Wang, “Enhanced water gas shift processes for carbon dioxide capture and hydrogen production,” *Appl. Energy*, vol. 254, no. April, p. 113700, 2019, doi: 10.1016/j.apenergy.2019.113700.

[41] C. H. Lee and K. B. Lee, “Sorption-enhanced water gas shift reaction for high-purity hydrogen production: Application of a Na-Mg double salt-based sorbent and the divided section packing concept,” *Appl. Energy*, vol. 205, no. July, pp. 316–322, 2017, doi: 10.1016/j.apenergy.2017.07.119.

[42] Y. Hu, H. Cui, Z. Cheng, and Z. Zhou, “Sorption-enhanced water gas shift reaction by in situ CO2 capture on an alkali metal salt-promoted MgO-CaCO3 sorbent,” *Chem. Eng. J.*, vol. 377, no. August 2018, p. 119823, 2019, doi: 10.1016/j.cej.2018.08.209.

[43] Y. Hu, Z. Cheng, and Z. Zhou, “High-purity H2production by sorption-enhanced water gas shift on a K2CO3-promoted Cu/MgO-Al2O3difunctional material,” *Sustain. Energy Fuels*, vol. 5, no. 13, pp. 3340–3350, 2021, doi: 10.1039/d1se00400j.

[44] Z. Fei *et al.*, “Probing thermal decomposition mechanism of molten nitrite/nitrates salt by time of flight mass spectrometry,” *Sol. Energy*, vol. 183, no. May, pp. 823–828, 2019, doi: 10.1016/j.solener.2019.03.067.

[45] C. Villada, A. Bonk, T. Bauer, and F. Bolívar, “High-temperature stability of nitrate/nitrite molten salt mixtures under different atmospheres,” *Appl. Energy*, vol. 226, no. May, pp. 107–115, 2018, doi: 10.1016/j.apenergy.2018.05.101.

[46] P. Gimenez and S. Fereres, “Effect of Heating Rates and Composition on the Thermal Decomposition of Nitrate Based Molten Salts,” *Energy Procedia*, vol. 69, pp. 654–662, 2015, doi: 10.1016/j.egypro.2015.03.075.

[47] R. W. Bradshaw, J. G. Cordaro, and N. P. Siegel, “Molten nitrate salt development for thermal energy storage in parabolic through solar power systems,” pp. 1–10, 2009.

[48] K. H. Stern, “High Temperature Properties and Decomposition of Inorganic Salts Part 3, Nitrates and Nitrites,” *J. Phys. Chem. Ref. Data*, vol. 1, no. 3, pp. 747–772, 1972, doi: 10.1063/1.3253104.

[49] R. I. Olivares, “The thermal stability of molten nitrite/nitrates salt for solar thermal energy storage in different atmospheres,” *Sol. Energy*, vol. 86, no. 9, pp. 2576–2583, 2012, doi: 10.1016/j.solener.2012.05.025.

[50] R. . Bradshaw and D. . Meeker, “High-temperature stability of ternary nitrate molten salts for solar thermal energy systems,” vol. 21, pp. 51–60, 1990.

[51] R. Bottom, “Thermogravimetric Analysis,” *Princ. Appl. Therm. Anal.*, pp. 87–118, 2008, doi: 10.1002/9780470697702.ch3.

[52] R. B. Prime, H. E. Bair, S. Vyazovkin, P. K. Gallagher, and A. Riga, “Thermogravimetric Analysis (TGA),” *Therm. Anal. Polym. Fundam. Appl.*, pp. 241–317, 2008, doi: 10.1002/9780470423837.ch3.

[53] E. M. U. Barbara L Dutrow, Louisiana State University , Christine M. Clark, “X-ray Powder Diffraction (XRD).” https://serc.carleton.edu/research_education/geochemsheets/techniques/XRD.html (accessed Jun. 18, 2021).

[54] A. K. Singh, *Experimental Methodologies for the Characterization of Nanoparticles*. 2016.

[55] L. S. U. Darrell Henry, U. of M.-L. Nelson Eby, U. of M.-D. John Goodge, and M. S. U. David Mogk, “X-ray reflection in accordance with Bragg’s Law.” https://serc.carleton.edu/research_education/geochemsheets/BraggsLaw.html (accessed Jun. 18, 2021).

[56] E. A. Rosauer, “Proceedings of the Iowa Academy of Science Crystallite-Size Determination of MgO by X-Ray Diffraction Line Broadening Crystallite-Size Determination of MgO by,” vol. 68, pp. 357–371, 1961.

[57] M. Thommes *et al.*, “Physisorption of gases, with special reference to the evaluation of surface area and pore size distribution (IUPAC Technical Report),” *Pure Appl. Chem.*, vol. 87, no. 9–10, pp. 1051–1069, 2015, doi: 10.1515/pac-2014-1117.

[58] U. of W. Susan Swapp, “Scanning Electron Microscopy (SEM).” https://serc.carleton.edu/research_education/geochemsheets/techniques/SEM.html (accessed Jun. 19, 2021).

[59] C. I. C. Pinheiro, A. Fernandes, C. Freitas, E. T. Santos, and M. F. Ribeiro, “Waste Marble Powders as Promising Inexpensive Natural CaO-Based Sorbents for Post-Combustion CO2 Capture,” *Ind. Eng. Chem. Res.*, vol. 55, no. 29, pp. 7860–7872, 2016, doi: 10.1021/acs.iecr.5b04574.

[60] N.-M.-T. I.A. Kazarinox, L.A.; Isaycheva, Makhmmod A. Adiba, “Protection of Metals and Physical Chemistry of Surfaces,” in *vol 55*, 2nd ed., 2019.

[61] T. H. Y. Duong *et al.*, “Synthesis of Magnesium Oxide Nanoplates and Their Application in Nitrogen Dioxide and Sulfur Dioxide Adsorption,” *J. Chem.*, vol. 2019, no. 2, 2019, doi: 10.1155/2019/4376429.

[62] K. D. Salman, H. H. Abbas, and H. A. Aljawad, “Synthesis and characterization of MgO nanoparticle via microwave and sol-gel methods,” *J. Phys. Conf. Ser.*, vol. 1973, no. 1, 2021, doi: 10.1088/1742-6596/1973/1/012104.

[63] A. T. Vu, Y. Park, P. R. Jeon, and C. H. Lee, “Mesoporous MgO sorbent promoted with KNO3 for CO2 capture at intermediate temperatures,” *Chem. Eng. J.*, vol. 258, pp. 254–264, 2014, doi: 10.1016/j.cej.2014.07.088.

[64] S. Jin, K. Ho, and C. H. Lee, “Facile synthesis of hierarchically porous MgO sorbent doped with CaCO3 for fast CO2 capture in rapid intermediate temperature swing sorption,” *Chem. Eng. J.*, vol. 334, no. September 2017, pp. 1605–1613, 2018, doi: 10.1016/j.cej.2017.11.095.

[65] X. Song, Y. Wu, F. Cai, D. Pan, and G. Xiao, “High-efficiency and low-cost Li/ZnO catalysts for synthesis of glycerol carbonate from glycerol transesterification: The role of Li and ZnO interaction,” *Appl. Catal. A Gen.*, vol. 532, pp. 77–85, 2017, doi: 10.1016/j.apcata.2016.12.019.

[66] T. Wang, D. Mantha, and R. G. Reddy, “Thermal stability of the eutectic composition in LiNO 3NaNO 3KNO 3 ternary system used for thermal energy storage,” *Sol. Energy Mater. Sol. Cells*, vol. 100, pp. 162–168, 2012, doi: 10.1016/j.solmat.2012.01.009.

[67] P. Hovington *et al.*, “Can we detect Li K X-ray in lithium compounds using energy dispersive spectroscopy?,” *Scanning*, vol. 38, no. 6, pp. 571–578, 2016, doi: 10.1002/sca.21302.

[68] D. E. Newbury, "Mistakes encountered during automatic peak identification in low beam energy X-ray microanalysis," *Scanning*, vol. 29, no. 4, pp. 137–151, 2007, doi: 10.1002/sca.20009.

[69] Y. J. Min, S. M. Hong, S. H. Kim, K. B. Lee, and S. G. Jeon, "High-temperature CO2 sorption on Na2CO3-impregnated layered double hydroxides," *Korean J. Chem. Eng.*, vol. 31, no. 9, pp. 1668–1673, 2014, doi: 10.1007/s11814-014-0116-1.

[70] R. L. Lehman, J. S. Gentry, and N. G. Glumac, "Thermal stability of potassium carbonate near its melting point 10.1016/S0040-6031(98)00289-5 : Thermochimica Acta | ScienceDirect.com," vol. 316, pp. 1–9, 1998, [Online]. Available: http://www.sciencedirect.com/science/article/pii/S0040603198002895.

[71] L. Shi, T. Qu, D. Liu, Y. Deng, B. Yang, and Y. Dai, *Process of Thermal Decomposition of Lithium Carbonate*. 2020.

[72] F. Pedrosa, T. Marcelo, C. A. Nogueira, A. Gomes, and T. Diamantino, "Molten nitrate salts containing lithium as thermal energy storage media: A short review," *ECOS 2018 - Proc. 31st Int. Conf. Effic. Cost, Optim. Simul. Environ. Impact Energy Syst.*, 2018.

[73] M. Bauer, Thomas; Breindenbach, N; Pfleger, N; Laing, D; Eck, "ASES Conference Solar," 2012.

[74] K. Zhang, X. S. Li, Y. Duan, D. L. King, P. Singh, and L. Li, "Roles of double salt formation and NaNO3 in Na2CO3-promoted MgO absorbent for intermediate temperature CO2 removal," *Int. J. Greenh. Gas Control*, vol. 12, pp. 351–358, 2013, doi: 10.1016/j.ijggc.2012.11.013.

[75] Y. Yang, M. Asta, and B. B. Laird, "Solid-liquid interfacial premelting," *Phys. Rev. Lett.*, vol. 110, no. 9, pp. 1–5, 2013, doi: 10.1103/PhysRevLett.110.096102.

[76] H. Yu, X. Wang, Z. Shu, M. Fujii, and C. Song, "Al 2 O 3 and CeO 2 -promoted MgO sorbents for CO 2 capture at moderate temperatures," vol. 12, no. 1, pp. 83–93, 2018.

[77] C. Dhoke, A. Zaabout, S. Cloete, and S. Amini, "Review on reactor configurations for adsorption-based CO2 capture," *Ind. Eng. Chem. Res.*, vol. 60, no. 10, pp. 3779–3798, 2021, doi: 10.1021/acs.iecr.0c04547.

[78] "The Engineering ToolBox." https://www.engineeringtoolbox.com/carbon-dioxide-thermal-conductivity-temperature-pressure-d_2019.html?vA=280&degree=C# (accessed Oct. 20, 2021).

[79] "The Engineering ToolBox." https://www.engineeringtoolbox.com/air-properties-viscosity-conductivity-heat-capacity-d_1509.html (accessed Oct. 20, 2021).

# 8 APPENDIX

## 8.1 EXPERIMENTAL APPARATUS

Figure 8-1 – TG-DSC sestsys Evo 16 – SETARAM analyzer.

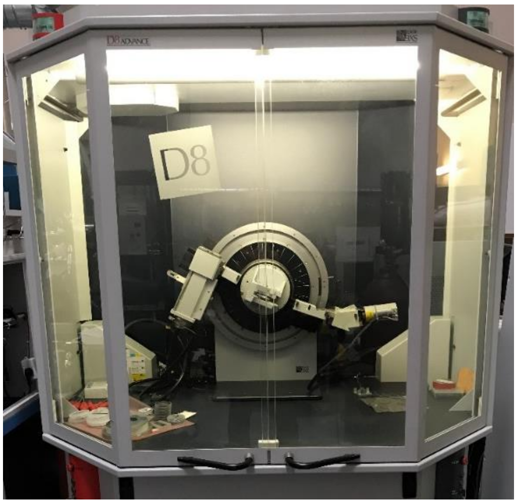

Figure 8-2 – Bruker D8 Advance Powder X-Ray Diffractometer.

Figure 8-3 – Autosorb IQ of Quantachrome Instruments.

Figure 8-4 – Phenom Pro G6 from Thermo Scientific.

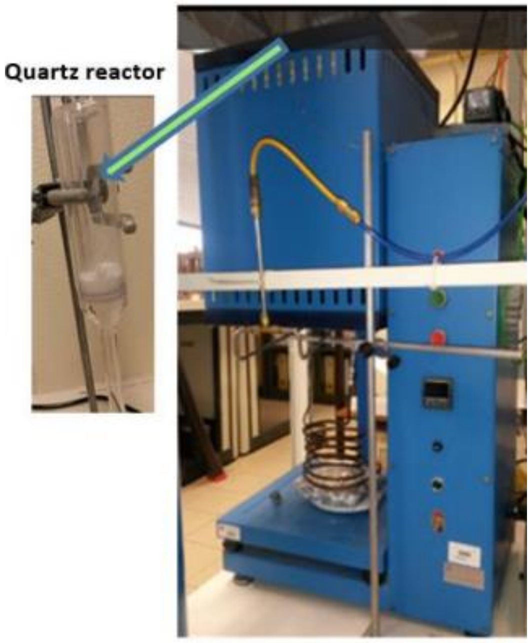

Figure 8-5 – Lab-scale fixed-bed unit and quartz reactor.

## 8.2 DETERMINATION PROCESS OF INFLECTION AND MAXIMUM $CO_2$ UPTAKE RATE TEMPERATURES

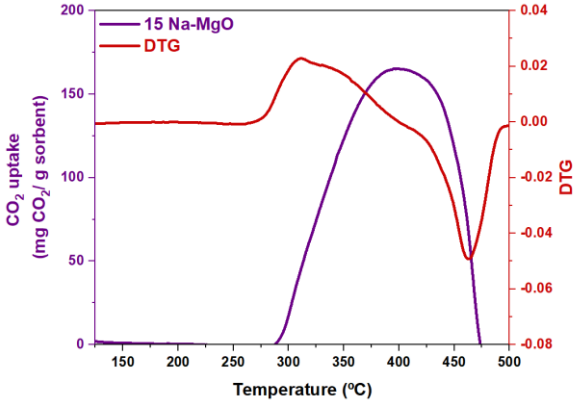

Figure 8-6 – $CO_2$ uptake profile of MgO-SG 4 sorbent doped with 15 % of $NaNO_3$ and respective first derivative.

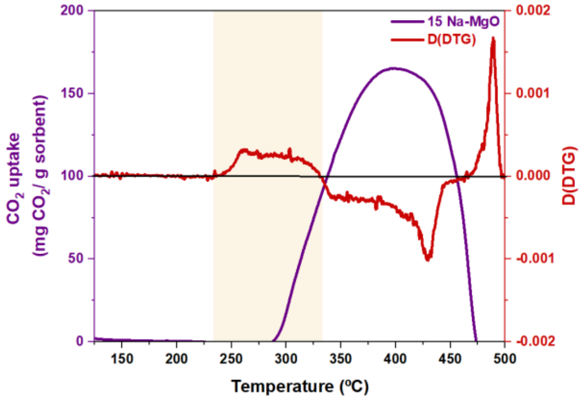

Figure 8-7 – $CO_2$ uptake profile of MgO-SG 4 sorbent doped with 15 % of $NaNO_3$ and respective second derivative (acelerating sorption is highlight in yellow).

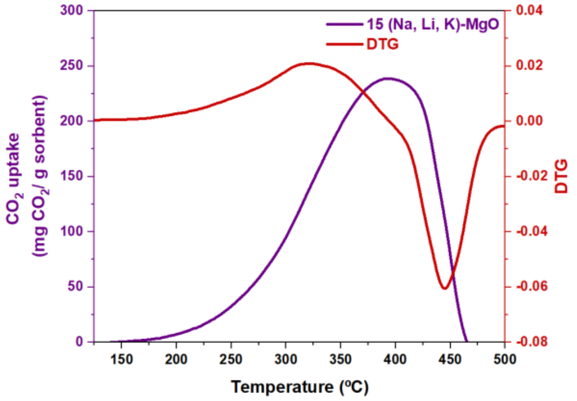

Figure 8-8 – $CO_2$ uptake profile of MgO-SG 4 sorbent doped with 15 % of (Na, Li, K)$NO_3$ and respective first derivative.

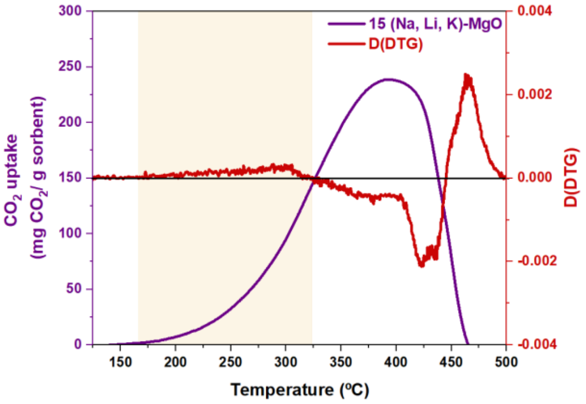

Figure 8-9 – $CO_2$ uptake profile of MgO-SG 4 sorbent doped with 15 % of (Na, Li, K)$NO_3$ and respective second derivative (acelerating sorption is highlight in yellow).

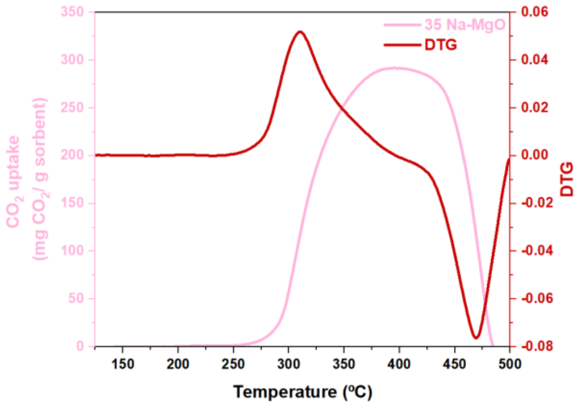

Figure 8-10 – CO$_2$ uptake profile of MgO-SG 4 sorbent doped with 35 % of NaNO$_3$ and respective first derivative.

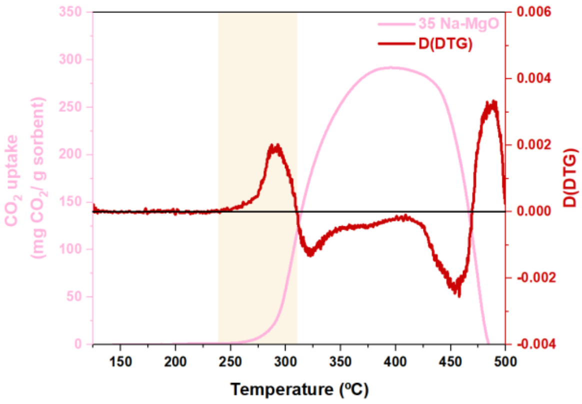

Figure 8-11 – CO$_2$ uptake profile of MgO-SG 4 sorbent doped with 35 % of NaNO$_3$ and respective second derivative (acelerating sorption is highlight in yellow).

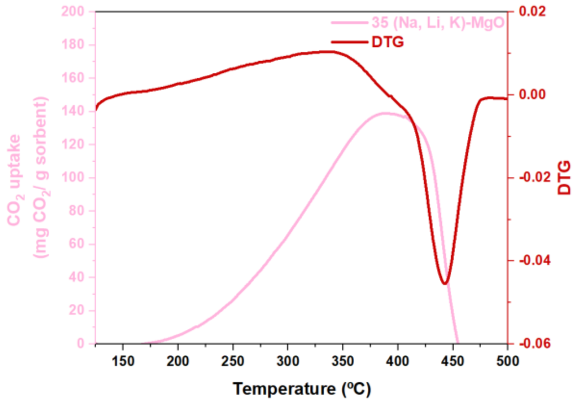

Figure 8-12 – CO$_2$ uptake profile of MgO-SG 4 sorbent doped with 35 % of (Na, Li, K)NO$_3$ and respective first derivative.

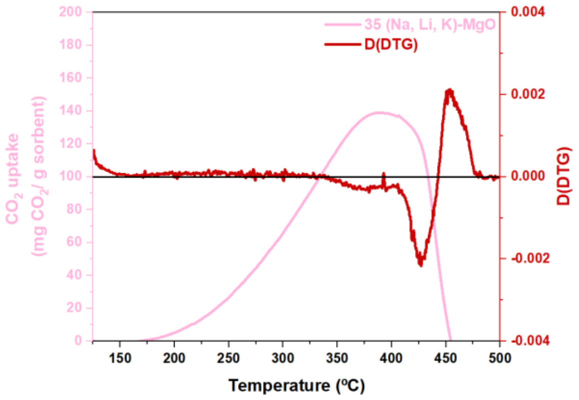

Figure 8-13 – CO$_2$ uptake profile of MgO-SG 4 sorbent doped with 35 % of (Na, Li, K)NO$_3$ and respective second derivative (acelerating sorption is highlight in yellow).

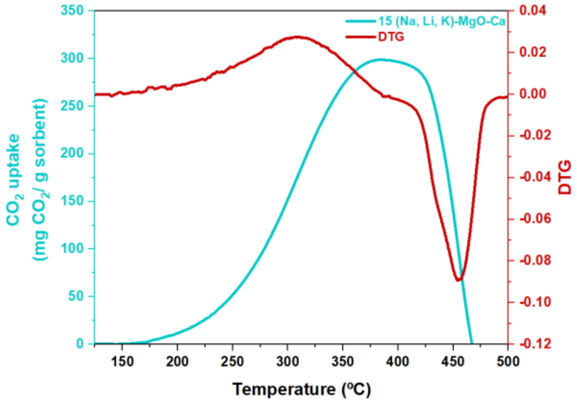

**Figure 8-14 – $CO_2$ uptake profile of MgO-SG-Ca sorbent doped with 15 % of (Na, Li, K)$NO_3$ and respective first derivative.**

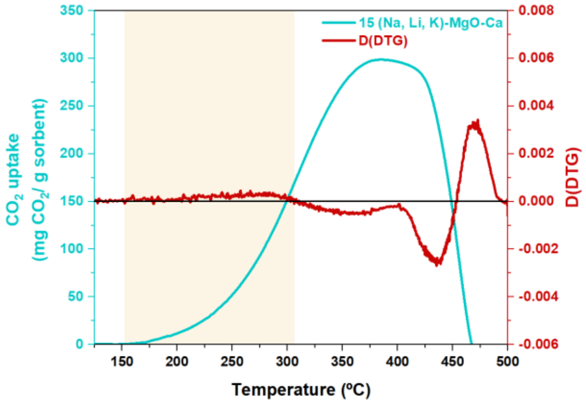

**Figure 8-15 – $CO_2$ uptake profile of MgO-SG-Ca sorbent doped with 15 % of (Na, Li, K)$NO_3$ and respective second derivative (acelerating sorption is highlight in yellow).**

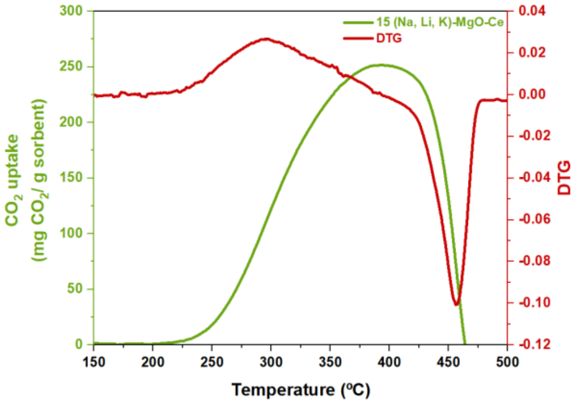

**Figure 8-16 – $CO_2$ uptake profile of MgO-SG-Ce sorbent doped with 15 % of (Na, Li, K)$NO_3$ and respective first derivative.**

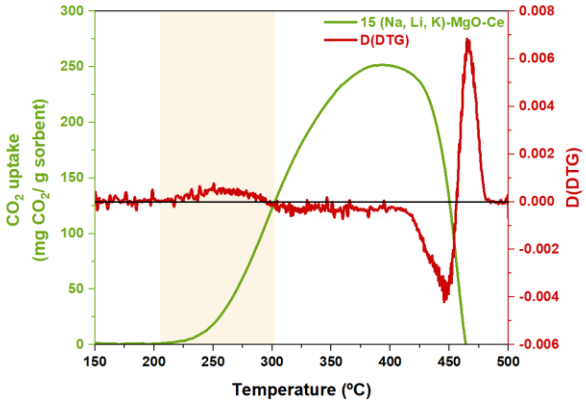

**Figure 8-17 – $CO_2$ uptake profile of MgO-SG-Ca sorbent doped with 15 % of (Na, Li, K)$NO_3$ and respective second derivative (acelerating sorption is highlight in yellow).**

## 8.3 XRD PATTERNS

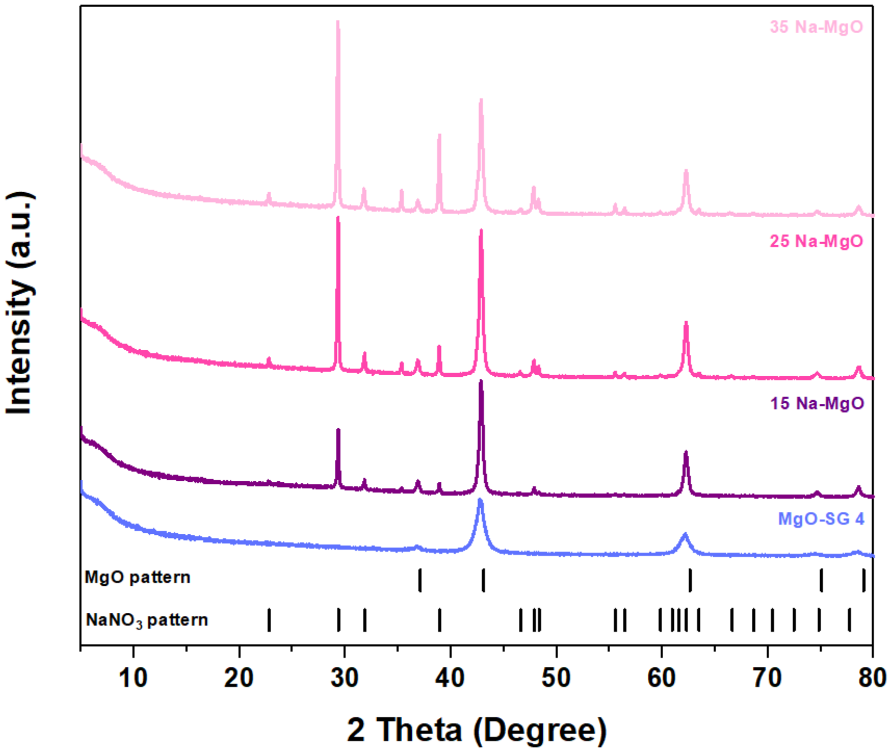

Figure 8-18 – XRD patterns of the fresh sorbent MgO-SG 4 and of the samples 15 Na-MgO, 25 Na-MgO and 35 Na-MgO after TGA tests.

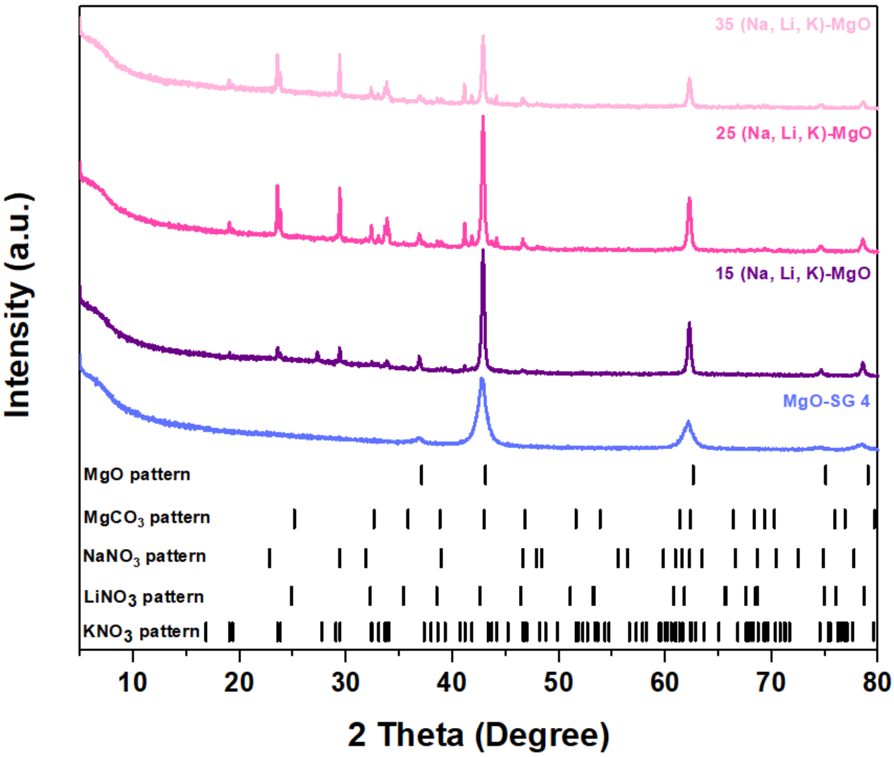

Figure 8-19 – XRD patterns of the fresh sorbent MgO-SG 4 and of the samples 15 (Na, Li, K)-MgO, 25 (Na, Li, K)-MgO and 35 (Na, Li, K)-MgO after TGA tests.